2013

Chemical composition and structure study of surfaces and ultrathin films of complex compounds

Yi Li
Louisiana State University and Agricultural and Mechanical College, yli48@lsu.edu

CHEMICAL COMPOSITION AND STRUCTURE STUDY OF SURFACES AND ULTRATHIN FILMS OF COMPLEX COMPOUNDS

A Dissertation

Submitted to Graduate Faculty of the
Louisiana State University and
Agriculture and Mechanical College
In partial fulfillment of the
requirements for the degree of
Doctor of Philosophy

in

The Department of Physics and Astronomy

by
Yi Li
B.S., Nanjing University of Post and Telecommunication, 2003
May 2013

ACKNOWLEDGMENTS

There are many people I would like to thank, who have contributed in some way towards this thesis. First I wish to express my gratitude to my supervisor, Professor Jiandi Zhang. His extraordinary passion for research, great knowledge and resourcefulness has been such an inspiration to me. He has provided insight and clear guidance throughout my study, and his support has been invaluable in every aspects. I also would like to thank my committee members for their encouragement, support and suggestions. The discussion with Dr. Ward Plummer, Dr. Rongying Jin and Dr. Mark Jarrell gave me both theoretical and experimental suggestions.

I would like to give my special thanks to Economic Development Assistantship (EDA) provided by the Graduate School in LSU. It greatly supported me in finishing my study and research. I am deeply grateful to my colleagues that have provided the environment for sharing their experiences about the problem issues involved as well as participated in stimulating discussions. The assistance and discussions offered by my collaborators have been very helpful, and therefore I wish to thank Zhaoliang Liao, Fangyang Liu, Gaoming Wang, Jing Teng and Guorong Li.

Finally I would like to thank my family. The love, encouragement and support from my parents and brother have made everything so enjoyable.

TABLE OF CONTENTS

LIST OF TABLES

LIST OF FIGURES

ABSTRACT

Complex Materials, such as transition-metal oxides (TMOs) with exotic properties provide immense opportunities in condensed matter and materials science. The signature and challenge of these materials is the multitude of competing ground states that can be tuned by doping, structural modification, or the application of external stimulus. The fundamental issues for the understanding of these emergent phenomena include the structure and chemical composition in the proximity of surface/interface.

In the thesis, I have developed a method using angle resolved X-ray photoelectron spectroscopy (ARXPS) to characterize the surface structure and chemical composition. In particular, I have considered the photoelectron diffraction effects on the relative intensities of different core electron levels which are essential to reveal the variation of chemical composition. I developed the basic methodology for the data analysis of the ARXPS spectra and used the well-known crystal surface of Sr_2RuO_4 (100) to verify our methodology.

Then I have used the developed ARXPS method to investigate the surface structure and chemical composition of a widely used crystal surface: $SrTiO_3$(100). I found that, although maintaining in-plane unreconstructed: primary $p(1\times1)$, the surface exhibits out-of-the-plane bulking relaxation. More importantly, the systematic analysis of ARXPS spectra show that the surface is TiO_2-layer terminated and has significant oxygen vacancies. These results confirm the conjecture from *LEED-I(V)* refinement on structure. The existence of surface oxygen-vacancies may explain the observed surface metallicity of $SrTiO_3$.

Finally, I have studied the chemical composition of the ultrathin crystalline films of $La_{2/3}Sr_{1/3}MnO_3$ on $SrTiO_3$ (100), especially the Sr surface segregation. I found that Sr concentration at the surface is appreciably higher than the corresponding bulk value. Such

an off-stoichiometric behavior should link to the different physical properties such as nonmetallic/nonmagnetic “dead layer” behavior in the ultrathin films compared with the bulk crystal.

To conclude, by considering the photoelectron diffraction effects, I have developed a method of ARXPES to characterize the surface chemical composition, which is essential for the understanding of emergent phenomena at surface, interface and thin film of complex materials.

CHAPTER 1. INTRODUCTION

1.1 Exciting physics in transition metal oxides (TMOs)

The past several years have seen extensive experimental and theoretical activities in correlated electron systems. Transition metal oxides (TMOs) among the correlated systems play a pivotal role in the search for understanding because of the exotic properties they exhibit. The numerous functionalities present tremendous opportunities and formidable challenges in condensed matter physics and materials science and the interest of these materials stems from the richness of their novel properties, the complexity of underlying physics. For example, there are metallic oxides ReO_3 and insulating $BaTiO_3$, which sit at the two ends of the range of TMOs. Vanadium oxides exhibit very different properties at various conditions. Doping of Sr into $La_{1-x}Sr_xVO_3$, increase of pressure on V_2O_3 and temperature of VO_2 leads to metal-insulator transition (MIT). Interesting electronic properties also arise from charge density waves (e.g., $K_{0.3}MoO_3$) and charge ordering (e.g., Fe_3O_4). Diverse magnetic properties, such as ferromagnetic, ferromagnetic and antiferromagetic are also found in, for instance, CrO_2, Fe_3O_4 and NiO respectively. Other exciting discoveries in physics, which caused worldwide study, are high temperature superconductivity in copper oxides (cuprates as a typical example), colossal magnetoresistance (CMR) effect and quantum phase transition. Strongly correlated electron systems have proven to be very difficult to understand. For example, so far no one has been able to put forward a theory of high-temperature superconductivity. Indeed, many phenomena associated with strong electron correlations are hard to explain, due to the fact that there are often several competing degrees of freedom in many of the technologically important classes of materials. The competition between different interactions can lead to quite complex phase diagrams.

To discuss some basic features of TMOs, let us first show a representative crystal structure of TMOs, that is, the perovskite structure with formula ABO_3, where A is pre-transition site and B is a transition metal. The surrounding six oxygen ions produce a crystal field acting on B with cubic symmetry [Figure. 1.1a]. Consequently, the originally five-fold degenerate 3*d* orbitals are split into three-fold degenerate t_{2g} orbitals (*xy, yz, zx* orbitals), and two-fold degenerate higher energy level e_g orbitals (x^2-y^2, $3z^2-r^2$ orbitals) (Figure 1.1b). The e_g electrons are more itinerant and the t_{2g} electrons are more localized generally. These orbitals have a different sign for the wave function depending on the radial direction, which results in the cancellation of the overlap integrals with the *p* orbitals of the O ions between two neighboring B ions. Therefore, the degenerate d-orbital further affects the spin coupling and creates a complex system being more than the sum of its single parts [1]. Through varying ionic size of the A site or doping of B site, etc., we can introduce tilting and rotating of oxygen octahedral to releases the strain; change the band width; tune the occupation of the d-orbital etc.

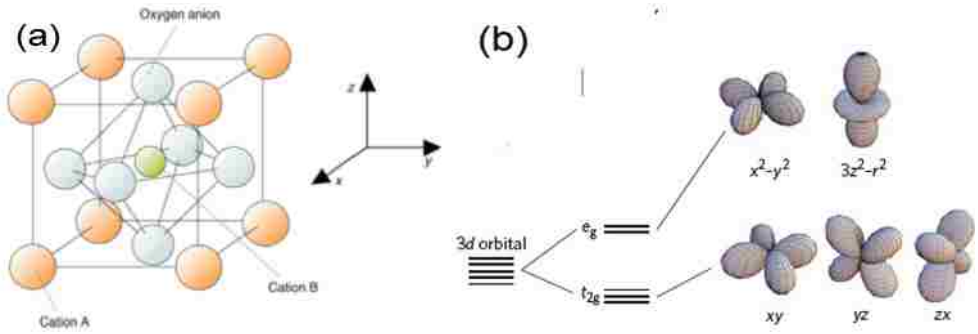

Figure 1.1. (a) Ideal ABO_3 perovskite structure. (b) Transition metal (3d) orbital energy levels under the crystal field effects due to simple cubic perovskite lattice structure.

The high-temperature cuprate superconductors offer examples of complexity and doping effect. In 1986 Bednorz and Müller [2] made one of the most important discoveries in modern condensed matter physics when they found that La_2CuO_4 becomes

superconducting when a certain amount of Ba^{2+} was doped at La site. This breakthrough quickly led to the discovery of other 'high-T_C' cuprate superconductors such as $YBa_2Cu_3O_{6+x}$ [3]. The superconductivity in these cuprate compounds was inconsistent with the well-established BCS theory, which correctly explained the conventional superconductors known [4]. Figure 1.2 shows a generic phase diagram for a hole-doped cuprate superconductor [5].

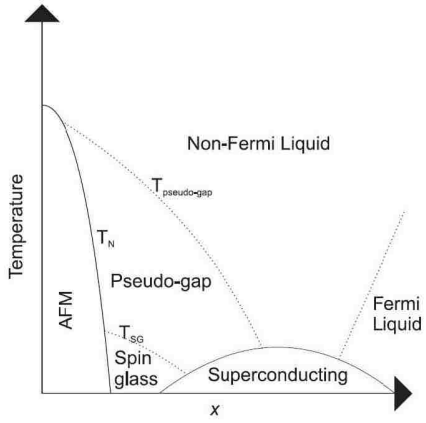

Figure 1.2. A generic phase diagram of a cuprate superconductor, showing the critical temperature T_c vs hole doping x.

The parent compound or the material at very low doping level is a Mott insulator and the spins order antiferromagnetically [6]. As x is increased the Néel temperature decreases, eventually reaching zero. If x is increased beyond this critical point the material enters either what is known as possible spin glass phase as the ground state or pseudogap phase at high temperature. It seems that electrons are not totally forbidden from crossing the gap, however, and the symmetry of the gap has been shown to be that of d-wave electrons. Superconducting phase appears with further hole doping. The critical temperature gradually increases with increasing $\boldsymbol{x}$, until a maximum is reached whereupon T_C gradually reduces.

All cuprate compounds share the following two elements: the CuO_2 planes that form single-layer or multilayer conducting blocks per unit cell, and the "charge reservoirs" in between the CuO_2 planes that are responsible for contributing either electrons or holes to the CuO_2 planes. It is understood that the electronic states of the CuO_2 planes mainly control the physics of high T_c superconductivity. By doping with substitution elements or by changing the oxygen content in the charge reservoirs, the carrier density in the CuO_2 planes can be controlled. However, the role of the oxygen dopants is not well understood, nor is it clear how the charge carriers are distributed on the planes. Doping component strongly disrupts the surrounding bonding environment and especially the electronic correlations between electrons on neighboring Cu atoms, thus the effects of this disruption on High Temperature Superconductivity (HTS) can, in principle, be used to help identify the microscopic mechanism. For this reason, numerous theoretical studies have analyzed the local effects of an impurity atom on the superconducting order parameter, and on the spatial dependence of the quasi-particle *LDOS*, in a d-wave superconductor. S.H. Pan et al. conducted Scanning Tunneling Microscopy study on $Bi_2Sr_2CaCu_2O_{8+x}$ [7]. The image in Figure.1.3 (a) reveals the crystal structure of the BiO plane with atomic resolution. After Fourier filtering, they observed the electronic inhomogeneity as shown in Figure 1.3(b).

Spatial variation of the energy gap and its correlation with the *LDOS* can be seen in greater detail in Figure 1.4. The existence of such microscopic inhomogeneities has many important consequences on the quasi-particle properties that are accessible by macroscopic measurements. They suggested that this inhomogeneity is actually indicative of the local nature of the superconducting state. When doping occurs, one may think

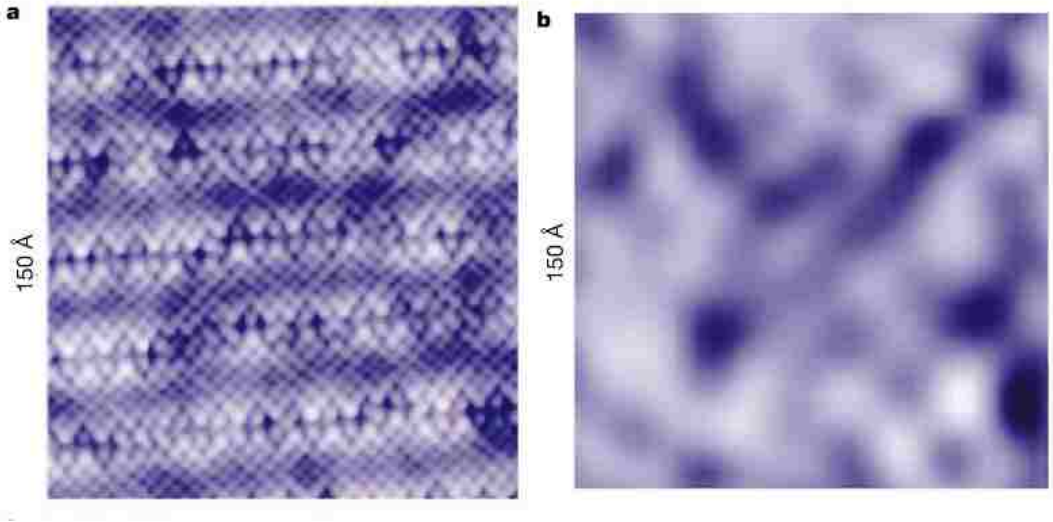

Figure 1.3. Topographic image and associated integrated LDOS map of an optimally oxygen-doped, nominally pure single crystal of $Bi_2Sr_2CaCu_2O_{8+x}$. a) Constant-current-mode, topographic image of the surface BiO plane exposed after cleavage of the single crystal. b) Fourier filtering is used to remove the contrast due to the two well-ordered topological structures mentioned above. The variation of the integrated LDOS, which is seen as an inhomogeneous background in a, is displayed. A brighter color represents a larger magnitude of the integrated LDOS. (Reference 7)

intuitively that apical oxygen in the CuO_6 octahedrons tend to approach toward central Cu^{2+} ions in order to gain the attractive electrostatic energy. Therefore the elongated CuO_6 octahedrons by the Jahn-Teller (JT) interactions shrink by doping holes. This high interaction between Jahn-Teller effect and doping with superconducting states is so important to study. Cuprate 2D layered structure and short interplanar coherence length make this type of materials suitable for surface probes, such STM and AR photoemission.

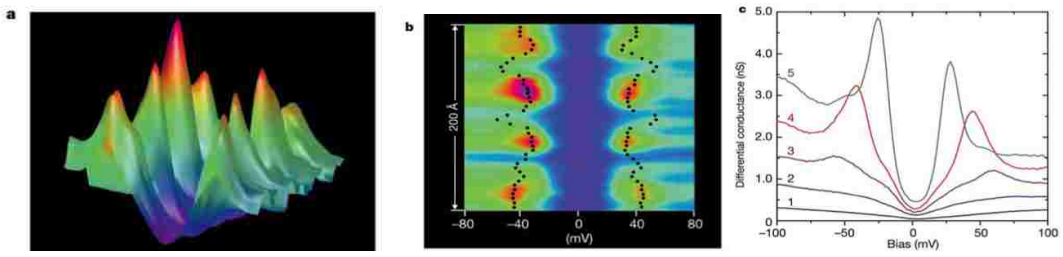

Figure 1.4. 2D and 3D plots of the spatial dependence of the differential conductance showing the microscopic inhomogeneity in the magnitude of the superconducting gap in $Bi_2Sr_2CaCu_2O_{8+x}$. The dots in the panel b trace out the superconducting band edges.

Ruthernate is another well-known TMO perovskite systems exhibiting multiple phases. The single-layered $Ca_{2-x}Sr_xRuO_4$, is quasi two-dimensional system, showing a rich array of interesting ground states [8,9]. As shown in Figure. 1.5 [10], isovalent cation substitution of the smaller Ca^{2+} by the bigger Sr^{2+} ions induces both structural distortion and an unusual variation of electronic and magnetic properties. As is common in perovskites when the **A**-site cations with different ionic radii are substituted, Ca replacement for Sr gradually modulates the rotational and tilt distortion of the RuO_6 octahedra, starting with a tetragonal I4/mmm structure for Sr_2RuO_4, to an I41/acd structure for $Ca_{1.5}Sr_{0.5}RuO_4$, and ending with an orthorhombic S-Pbca structure for Sr_2RuO_4 [11]. This in turn leads to an evolution of the ground state, from an unconventional 'p-wave' superconducting state in Sr_2RuO_4 with possible spin-triplet pairing [12], to a quantum critical point at $x = x_c \sim 0.5$ and to an antiferromagnetic Mott insulating phase when $x < 0.2$.

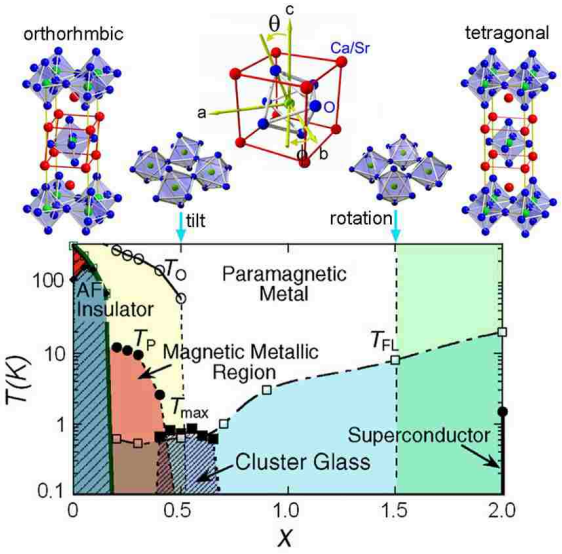

Figure 1.5. Phase diagram with structural evolution of $Ca_{2-x}Sr_xRuO_4$. T_O, T_P, and T_{max} are the orthorhombic structural transition temperature and the peak temperature of $\chi(T)$, and peak temperature of M(T) curve with zero-field cooling, respectively. Both rotational (φ) and tilt (θ) distortion of RuO_6 octahedron are shown.

The family of manganese based perovskites, which have the general form of $R_{1-x}D_xMnO_3$ (R is trivalent rare-earth element and D is divalent element), display unusual properties as well with coupled structural, electronic and magnetic phase transition. Both end members of $La_{1-x}Ca_xMnO_3$ are antiferromagnetic insulators [13], but become ferromagnetic metal (FM) upon doping or antiferromagnetic (AFM) and charge/orbital ordered insulator. The phase diagram of $La_{1-x}Ca_xMnO_3$ as a function of T and x is given in Figure. 1.6 [14]

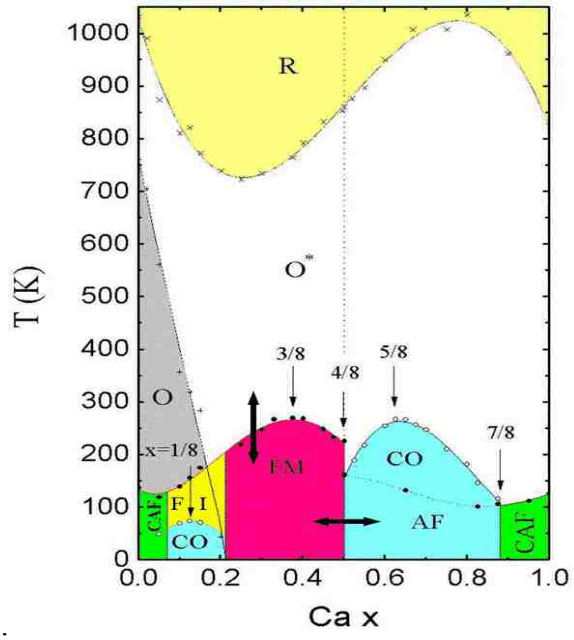

Figure 1.6. Electronic phase diagram of $La_{1-x}Ca_xMnO_3$. The horizontal axis shows the value of Ca content in the formula. Phases include charge-ordered (CO), antiferromagnetic (AF), canted antiferromagnet (CAF), ferromagnetic metal (FM), and ferromagnetic insulator (FI).

The curved line is drawn approximately on the boundary between the spin-disordered paramagnetic state and the spin-ordered states, and the hatched lines indicate the approximate boundaries between different ground states. This material is a paramagnetic insulator above the magnetic ordering temperature. At lower temperature, the magnetic ordering depends on the amount of doping. With doping of small amounts of Ca, the

materials become ferromagnetic insulator and charge-ordered states developed inside this phase at even lower temperature. With increasing doping, the material becomes ferromagnetic metal with strongest ferromagnetic coupling at $x \sim 0.35$ as Curie temperature reaches the maximum. In the high-doping region which extends to $x = 1$ (x>0.5), the compound is antiferromagnetic insulator, and then undergoes a transition to an insulating Charge Ordering (CO) state with decreasing temperature.

Many experimental and theoretical studies have indicated that the inhomogeneous nature arising from competition between the ferromagnetic (FM) metallic and antiferromagnetic (AFM) insulating states leads to a large change in the resistivity as a function of temperature, magnetic field, chemical pressure and so on. After the early studies of manganites described above, Tokura et al. [15,16,17] proposed that the Charge-ordering (CO) states observed by Jirák et al. [18] were very important for the explanation of the CMR effect. They presented results indicating an abrupt collapse of the CO state into a ferromagnetic (FM) state under the influence of a magnetic field. The competition between CO and FM is indeed a key component of the current theories of manganites aiming to explain the CMR phenomenon. It is clear from the experiments and the theory that the CO-FM transition should be first-order unless disordering effects smear it into a rapid but continuous transition. The huge CMR effect in some compounds at very low temperatures appears to be caused by the CO-FM first-order transition induced by magnetic fields.

1.2 New properties due to reduced dimensionality

The dimensionality effect also plays a key role of controlling the properties of complex materials. To illustrate the range of dimensionality in the TMOs, we are

describing the well-known layered Ruddlesden-Popper series also have remarkable complex electronic and magnetic properties. Take $Sr_{n+1}Ru_nO_{3n+1}$ (Figure 1.7) as an example, n is the number of layers of corner-sharing RuO_6 octahedra per formula unit. The properties of $Sr_{n+1}Ru_nO_{3n+1}$ exhibit strong dependence on the number of RuO_6 octahedral layers in crystal structure, reflecting the effect of dimensionality in the system. Single-layered Sr_2RuO_4, as the most two-dimensional-like compound in the perovskite series, is an unconventional superconductor with possible spin-triplet pairing [19,20,21]. The bilayered $Sr_3Ru_2O_7$ shows behavior consistent with proximity to a metamagnetic quantum critical point [22]. The magnetic ground state of the triple-layer $Sr_4Ru_3O_{10}$ is poised between an itinerant metamagnetic and itinerant ferromagnetic state [23,24,25], regarded as a three dimensional compound, is an itinerant ferromagnet with unusual transport characteristic [26,27].

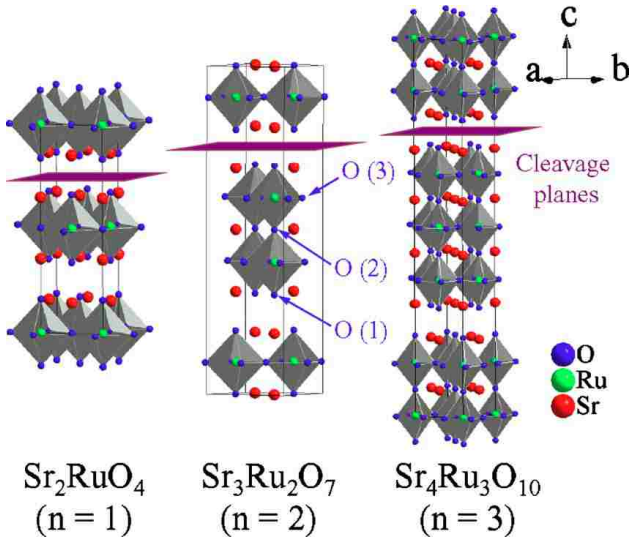

Figure 1.7. Schematic structure of the n=1, n=2 and n=∞ members of the Ruddlesden-Popper series $Sr_{n+1}Ru_nO_{3n+1}$. The structure properties of n=1 and n=2 phases are clearly low dimensional and are expected to lead to highly anisotropic physical properties, while n=∞ structure is 3D indeed.

Figure 1.8 is an artist's view of the high-*Tc* material $HgBa_2Ca_2Cu_3O_{8+x}$. This material has one of the highest superconducting temperatures recorded, when optimally doped with oxygen (x~0.14) [28]. The parent compound (x=0) is not a superconductor but when excess O is incorporated into the Hg-O lattice it pulls charge out of the CuO_2 plane and drive the material into the superconducting state. Conventional wisdom says that the superconductivity occurs in the central CuO_2 plane, so this is really a reduced dimensionality system.

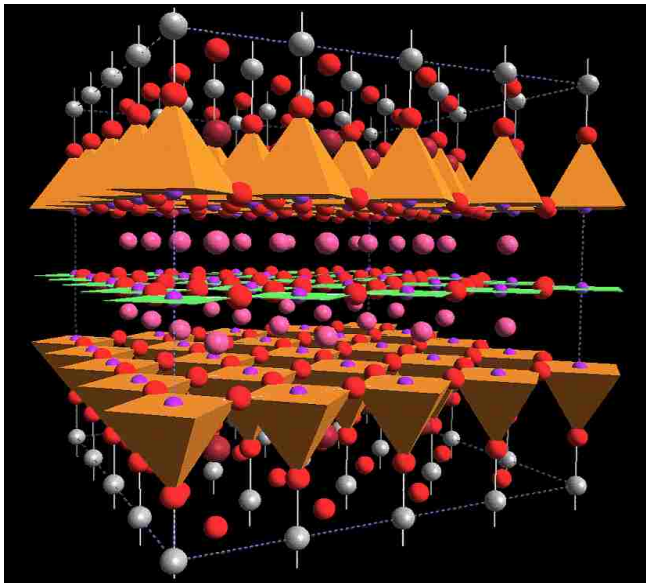

Figure 1.8. Artistic view of the crystal structure of the high-temperature superconductor $HgBa_2Ca_2Cu_3O_{8+x}$, showing highly 2D (layered) character. The orange pyramids present the appropriate portion of CuO_6 octahedra.

Besides the global effect of dimensionality variation from 3D-2D, there is also nano scale reduction, as small as a single atom, which induces the emergent phenomena. These are greatly and comprehensively demonstrated in lots of materials ranging from a single substance such as gold nanodots to compound such as manganites thin films. Nanoparticle, nanowire, ultrathin film, *etc.*, are several typical examples of nanomaterials and result from reduced dimensionality and broken symmetry. The smaller size of a

material, the wider band gap will be. Showing in Figure 1.9 from 3D to 0D, the Density of States (DOS) changes from continuous function (3D) to Step function (2D), saw tooth (2D) and δ function (0D). These will dramatically modify the mechanical, thermal, electronic, optic and magnetic properties. For examples, the dimensionality can control the electronic phase transition in $LaNiO_3/LaAlO_3$ superlattice [29] and quantum well state emerges in ultrathin $SrVO_3$ film [30].

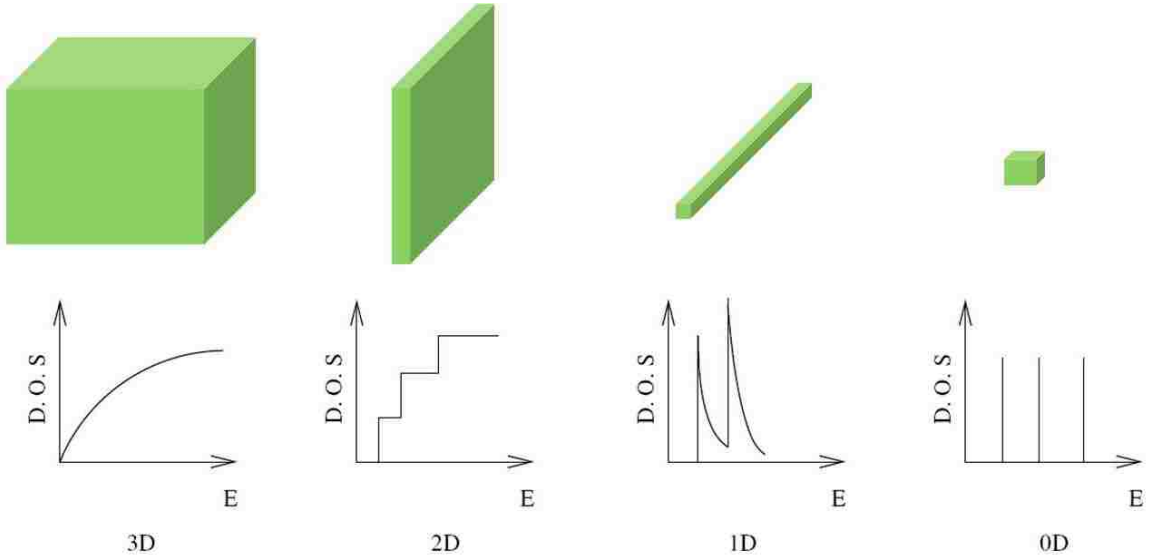

Figure 1.9. Reduced dimensionality induced change of density of States (DOS).

Many materials have inherent length scale of interaction, or inhomogeneities (for example, phase separation). These length scales could vary from 1 nm to 1 micrometer. For example, the superconductive coherence length, which is the characteristic size of cooper pair, is about 2 nm in $YBa_2Cu_3O_7$ in a-b plane. The Bohr radius of 1s exciton in bulk ZnO is reported to be 2.34nm [31]. The phase separation domain size in $La_{0.55}Ca_{0.45}MnO_3$ is about 5 nm as revealed by transmission electron microscopy [32]. The largest domain with size of micrometer is reported in $La_{(1-x)}Pr_xCa_{3/8}MnO_3$ (LPCMO) which is directly confirmed by AFM image (see Figure 1-4)[33]. To conclude, reduced

dimensionality will strongly affect the co-existent and competing coupling among the spin, lattice, charge and orbital, thus it is another key control parameter to tune the properties. Again, the complexity of this class of materials deserves careful characterization in both structure and composition.

1.3 Emergent phenomena at interface/surface of $SrTiO_3$

The signature of these TMO materials is the multitude of competing ground states that can be turned or manipulated by chemical doping, structural manipulations, strain induction, or the application of external stimulus, such as pressure, electric or magnetic fields, etc. Understanding of the various types of exotic behaviors exhibited by correlated electron systems has dramatically challenged our perspective of solids. One of the most important tuning parameters "doping" requires us to study the spatial dependence of chemical composition in depth, which is not precisely determined due to not too many techniques. We have learned that complex materials are so sensitive to the local environment and we could image the surface differs from the bulk dramatically. In the past few years, it is becoming increasingly clear that interfaces, thin films, and heterostructures of TMOs display a rich diversity of fascinating properties that are related to, but not identical to, the bulk phenomena. Correlated electron devices will involve the fabrication of thin films, superstructures and junctions. Virtually all electronic devices began with an understanding of interface barrier formation, electronic/magnetic structure, and control — "**the interface is the device**" [34]. Knowledge of the surface/interface properties as well as the effects derived from broken symmetry and spatial confinement is essential if these devices are to be made to work at optimized functionality.

$SrTiO_3$ (100), a band insulator, is a frequently used material as the foundation of the emerging field of oxide electronics [35,36]. Also it serves the most important substrate for expitaxial thin film growth, which will be discussed in depth later. $SrTiO_3$ is the preferred template for the creation of exotic, two-dimensional (2D) phases of electron matter at oxide interfaces [37,38,39]. The APRES data also reveals the existence of universal free electron gas at surface which can be controlled by ultraviolet illumination [40, 41]. First principle pseudopotential method indicates that reduced surface becomes metallic as well [42]. However, the physical nature of the electronic structure underlying these 2D electron gases (2DEGs), which is crucial to understanding their remarkable properties [43,44], remains elusive. Figure 1.10 demonstrates the observation of a surface 2DEG on SrTiO3 after exposure of the cleaved (100) surface to synchrotron (ultraviolet) light. People also have shown some perovskites interface also shows a number of appealing properties that have metal–insulator transitions [45,46], superconductivity [47,48] or large negative magnetoresistance [49].

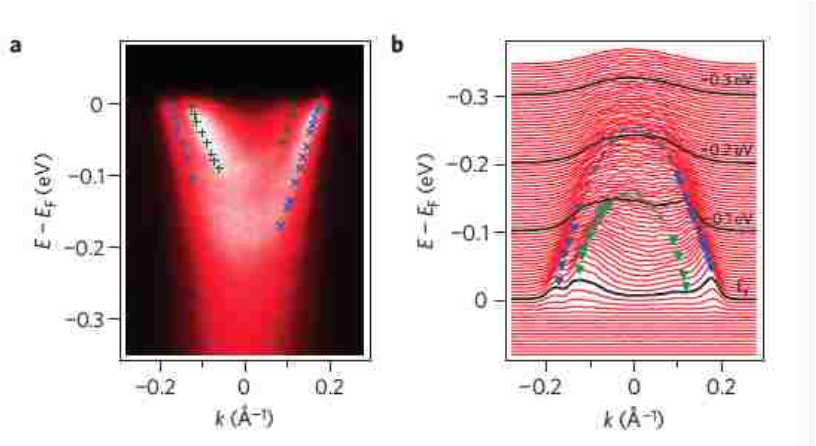

Figure 1.10. ARPES data of $La_xSr_{1-x}TiO_3$ (x=0.001) at T = 20 K (a) with corresponding momentum distribution curves (b) The sample has been irradiated with 480 J.cm-2 ultraviolet light of 55 eV with an intensity of ~0.34Wcm^{-2}. The ARPES data are taken in the second Brillouin zone using the same photon energy.

Let us look at the $LaAlO_3$-$SrTiO_3$ (LAO-STO) interface. LAO and STO are both insulators, with a band gap respectively of 5.4 and 3.2 eV. The main difference between LAO and STO resides in the layer charge polarity [50]: STO (100) is a non-polar solid, while LAO is a polar solid. These materials both belong to the perovskite group, which share the same chemical formula (ABO_3) and a similar cubic crystal structure. The interface can be p-type when the bulk STO is terminated with a SrO plane (hole doping) and n-type with a TiO_2 plane (electron doping). Figure 1.11 illustrates the schematic of the resulting LaO/TiO_2 and AlO_2/SrO interfaces, showing the composition of each layer and the ionic charge state of each layer. Only in the latter case, the interface has conducting property and 2D free electron gas forms. The Ti related electronic states are thus expected to carry the metallic states. Having the full understanding of substrate surface is crucial to analyze the interface properties as the small change on the substrate will lead to completely new phenomena.

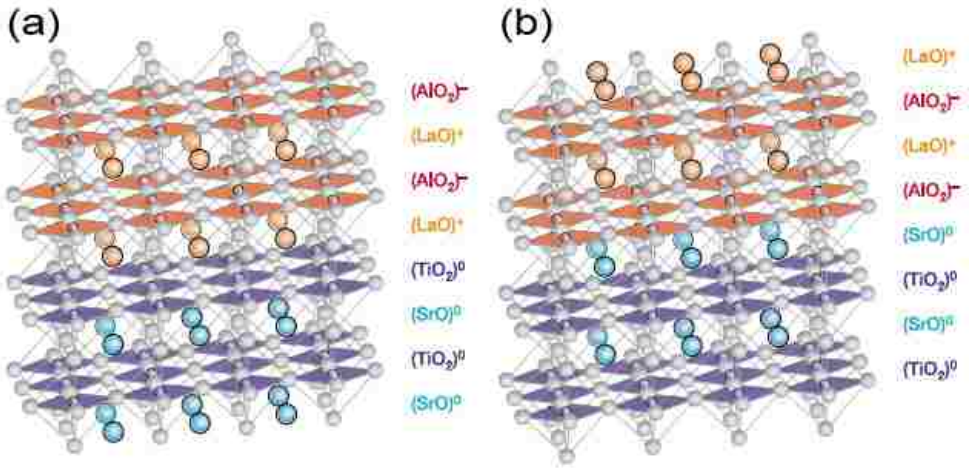

Figure 1.11. Schematic view of the LaO/TiO_2 and AlO_2/SrO interface.

Figure 1.12 shows the 15 unit cells (UC) coverage of LAO film on STO single crystal. The Scanning Transmission Electron Microscopy (STEM) image displayed in panel A indicates the coherent interface. The occurrence of the zero-resistance state and the characteristic R (T, H) dependencies provide clear evidence for superconductivity. In addition to that, magnetic fields up to $\mu_0 H = 8$ T were applied to the 8-uc-thick sample, revealing a positive magnetoresistance (Figure 1.9b). Moreover, there's a thickness dependence of the metal transition. 2DEG is observed only when the capping is at least 4-unit cell thick [51].

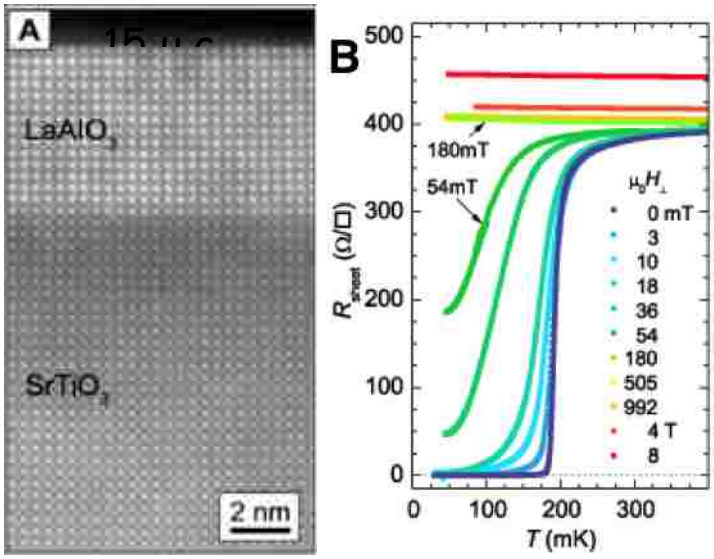

Figure 1.12. (a) High-angle annular dark field image of a 15-uc-thick $LaAlO_3$ film grown on $SrTiO_3$. (b) Sheet resistance of the 8-uc sample plotted as a function of temperature for magnetic fileds applied perpendicular to the interface.

Intrinsic electronic reconstruction has been proposed [52] and observed by photoelectron spectroscopy studies [53,54,55]. On the other hand, oxygen-annealing experiments [56,57] indicated that the formation of oxygen vacancies introduced by pulsed laser deposition process is the source of the large carrier densities at the interface.

Surface X-ray diffraction [58] and medium-energy ion spectroscopy [59] suggested that cationic (A-site) mixing occurs thus resulting in dilatory lattice distortions and the formation of metallic $La_{1-x}Sr_xTiO_3$ at the interface. Recent theoretical calculations predicated a thickness-dependent polar distortion [60] and an exponential decay of lattice relaxation effects [61] in LAO film. A metal-to-insulator transition (MIT) has been reported around four unit cell thickness of LAO on STO [62]. Surface X-ray diffraction [58] has provided the evolution of lattice constant in normal direction to the surface but the detailed Jahn-Teller (JT)-type lattice distortion is yet to be determined. Therefore, the mechanisms for the metallic behavior at the interface are still debated intensively. Many issues still remain to be resolved: What is the difference of JT distortion at the interface compared to the bulk materials? How to quantitatively describe the effect of vacancies and defects on the metallic properties at interface? What is the main driving force for the observed MIT?

Although the reasons of these behaviors are not well defined, people suspect that polarity as the cause of the interface properties, which can be produced during the sample preparation or intrinsic after breaking the symmetry. The key issues are surface or film stoichiometry, and dependence of the chemical and electronic structures of the epitaxial interface on surface treatments. Comprehensive characterization of the interface with atomic scale precision is essential.

1.4 Motivation of this thesis project

The carrier density and sheet conductivity of the surface/interface 2DEG react sensitively to gate fields. It was successfully patterned on the nano-scale, which is central

to the development of oxide electronics [63]. However, the understanding of the origin of this 2DEG is unclear. And the chemical complexity of most oxides would make devices much inferior to those based on conventional semiconductors.

So far we know the change of chemical composition in proximity of surface and interface will dramatically change the properties. As transition metal cations can exist in multiple valences, a variation in local bonding configuration is possible. Due to this, even small change in composition, such as oxygen deficiency in LAO/STO interface, surface segregation of $La_{1-x}Sr_xMnO_3$, can form complete different materials, as the TMOs materials properties are so sensitive to the local composition and structure.

Spectroscopic investigations of surface TMOs are essential to elucidate the fundamental electronic structure and underlying role of many-body interactions in oxide 2DEGs, and so will play a major role in the development of all-oxide electronics. The core level XPS and valence ARPES are extremely important in determining the chemical composition, impurity, chemical valence and bonding environment, and electronic band structure of thin films. XPS provides the signature of a chemical component. The shift and relative intensity of core-levels give us the information on chemical composition and chemical valence. The satellite spectra in XPS offer the information on electron-electron correlation. ARPES near Fermi surface can allow us to determine the valence band structure, Fermi surface and superconducting gap related to the thin films. This study will require such techniques, including Angle resolved X-ray photoelectron Spectroscopy (XPS) and Ion Scattering Spectroscopy (ISS). My objective of thesis project: How to use ARXPS to determine composition, especially considering the diffraction effect. The thesis work is developing a method of using ARXPS to determine the composition in the

proximity of surface of a crystal or a thin film of oxide materials. By probing the individual atomic sites, it is possible to determine with a very high spatial resolution the atomic and electronic structure in many oxide materials. This is an important advantage for the investigations to tune the electronic properties in oxide structures by controlling the atomic arrangement at the interfaces. Novel heteroepitaxial devices based on this atomically controlled growth, like ferroelectric devices, Mott transition devices, superconducting devices and magnetic random-access memory devices, have great potential for future applications.

A prerequisite to ensure a high-quality interface and thin films is that the starting surface of a substrate has to be atomically smooth. A key feature in this project is that we will use the surface sensitive and atomic resolved characterization techniques to examine the surface of the single crystal and thin film. The surface preparation of a substrate will include three techniques, depending on which substrate we want to use and what termination we need: 1) in-situ cleaving of a layered single crystal; 2) ex-situ chemical etching and in-situ post annealing; 3) ion-sputtering and annealing. After the films are grown or the single crystal is cleaved, the characterization abilities are the key to the understanding of the strain induced novel properties and close coupling of different degree of freedoms.

We propose to use Angle resolved X-ray Photoelectron Spectroscopy (ARXPS) and Ion Scattering Spectroscopy (ISS) to study the surface of TMOs materials. The basic concept of ARXPS is changing surface sensitivity by detecting photoelectrons travelling a distance d in the solid at different emission angles. The main advantages of ARXPS for surface studies are, beside the non-destructiveness, their direct information of electronic

states, straightforward to compare with theory, surface sensitive probe, and being sensitive to “many body” effects. Even small surface flat samples can apply this technique under Ultra high vacuum conditions. Meanwhile if the surface is disordered, ARXPS cannot extract the reasonably good information from it. ARXPS cannot be used for non-conducting samples, which constrain the applications from using on the insulator surfaces. ISS is also a useful tool as a newcomer in surface analysis with excellent detection sensitivity. The extremely low ion intensities during analysis reduce charging problems with isolating samples to a minimum, which can be easily overcome by using a simple charge neutralization system. Even organic samples can be analyzed at low ion doses without serious degradation problems as they are observed under the bombardment of energetic electron beams. The ISS method suffers only negligible matrix effects. Therefore quantitative comparison of different samples analyzed under identical conditions and quantitative depth profiling are easily performed. Because of the scattering process, which will be discussed later, the ISS method cannot detect elements lighter than He. At present the main disadvantages of the ISS method are the limited mass resolution and the lateral resolution of 100 pm. Nevertheless, for a variety of applications the ISS method exhibits important advantages and surface analytical laboratories are therefore more and more accepting it. Detail description of equipment setup will be described in the next chapter.

1.5 Scope of the thesis

The present thesis is organized as follows:

- Experimental techniques, including thin film preparation through Pulsed Laser Deposition (PLD), real time film growth monitoring through Reflection High

Energy Electron Diffraction (RHEED), Scanning Tunneling Microscopy (STM) and Lowe Energy Electron Diffraction (LEED) as the surface characterization techniques, Angle Resolved X ray photoelectron spectroscopy (ARXPS).

- The methodology of studying the surface composition through ARXPS is developed. Sr_2RuO_4 single crystal was used to further test the effectiveness of this methodology.
- Our ARXPS experimental results on the single crystal Nb doped $SrTiO_3$ (100) surface is described and discussed.
- We also carry the ARXPS study of LSMO 6 Unit Cell thin film to discuss the chemical composition.
- Core level study of Iron Based Superconductor of "122" family.

CHAPTER 2. EXPERIMENTAL TECHNIQUES

2.1 Laser molecular beam epitaxy (MBE)

To achieve the goal of in-situ growth and characterization with atomic precision, we constructed a UHV oxide growth system based on the pulsed laser deposition (PLD) method [64,65,66] and Molecular Beam Epitaxy (MBE) concept. MBE was developed to enable atomic control and characterization of thin film growth processes of semiconductors, while PLD was verified to be extremely useful for transforming sintered targets of multi-component TMO materials into thin films. Pulsed-laser deposition (PLD) is one of the most promising techniques of the formation of complex-oxide heterostructures, superlattices, and well-controlled interfaces. The advantages of PLD include deposition under relatively high oxygen pressures and preservation of target composition in the film. It is natural to combine the advantages of both PLD and MBE to achieve atomically controlled growth of oxides and other complex materials [4]. Combined with LEED and STM/AFM/XPS, we are able to 1) grow materials in layer-by-layer with atomic level; 2) control the surface termination; 3) directly image the morphology and structure on atomic scale so that we know exactly what we have grown and what the surface/interface looks like. The main advantage of the system is allowing the optimization of the growth condition in real-time fashion.

The technique of PLD is conceptually simple, as illustrated schematically in Figure. 2.1(a). A pulsed-laser beam bombards the target to remove the surface materials from a solid then forms a plasma plume, which will deposit onto a substrate. The plume always contains a combination of ions, electrons and neutral particles. Usually, the excimer lasers with a wavelength in ultraviolet range have been used in PLD deposition, such as KrF (248 nm), XeCl (308 nm), and ArF (193 nm), the width of the wavelength is about

10-40 nm. The laser-solid interaction is very rapid. The penetration depth is about hundreds of nm, and the temperature is as high as $10^3 - 10^4$ °C. In our setup, the laser source we used is KrF excimer with the 6 targets in chamber with capabilities of rotation. The KrF excimer laser we use was provided by Lambda Physik Co., which has a wavelength of 248 nm and pulse duration of 30 ns. The laser energy of each pulse can reach up to ~1.0 Joule.

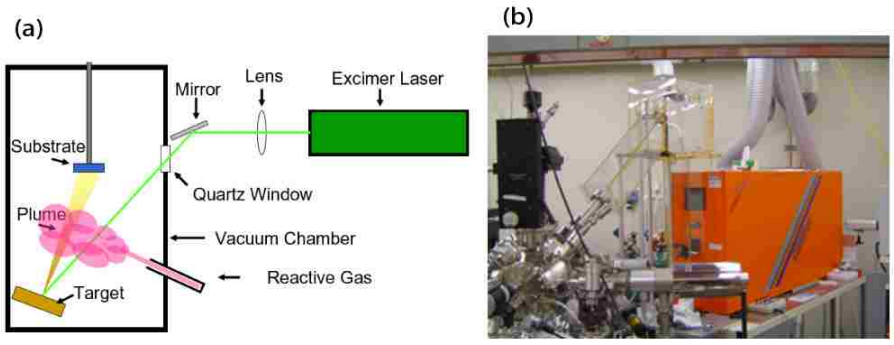

Figure 2.1. a) The schematic view of laser MBE setup. b) Our integrated Laser-MBE and *in-situ* characterization system made up of XPS, STM/AFM, LEED.

The fabrication of thin film materials through layer-by-layer epitaxial growth with full control over the composition and structure at the atomic level has become one of the most exciting areas of research in condensed matter physics and materials sciences. Laser molecular beam epitaxial (LMBE) uses the merits of both pulsed laser deposition and conventional MBE for depositing films, especially for high melting point ceramics and multicomponent solids, controlled in the atomic scale.

Reflection High Energy Electron Diffraction (RHEED) is a surface sensitive technique to probe surface topography and to monitor dynamic growth process. The RHEED setup is schematically shown in Figure 2.2. It is an electron gun shooting high-energy electron beam approaches a sample surface at a very small grazing angle θ (<5°).

The diffracted electrons reach a phosphor screen and form a RHEED pattern, which depends not only on the surface symmetry but also surface topography. Practically the display screen is usually a phosphor coating on the inner side of glass vacuum window and the diffraction pattern is recorded by a camera at the outside of the window. Because of the grazing angle, the electron will not impede the growth process and the surface sensitivity maintains as the inelastic mean free path is reduced by $1/\cos\theta$. The penetration is only about 2 or 3 monolayers in most cases.

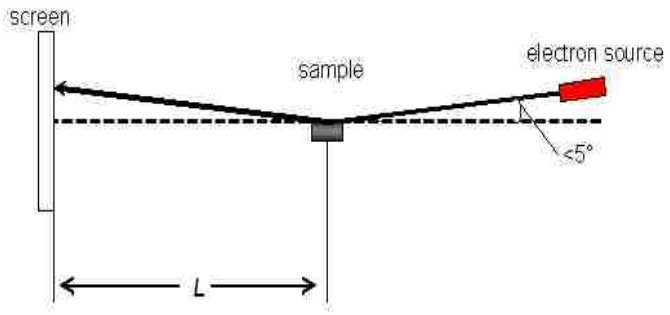

Figure 2.2. Schematic diagrams of RHEED apparatus

The diffraction beams can be deduced from reciprocal lattice space, which consists of lattice rods in the direction normal to the surface. The diffracted beam with the wave vector has the same magnitude of incoming wave vector, but different direction. We know that the diffraction maximum occur only when the Laue equation or equivalent, Bragg condition are satisfied. This condition occurs whenever a reciprocal lattice point lies exactly on the Ewald Sphere. The surface irregularities that result in the expanded width of the rods and the X ray source energy range both make the RHEED spot a line shape. In case of spot diffraction pattern in RHEED, which is actually means the surface is rough because the incident beam penetrate into the islands and other rough features.

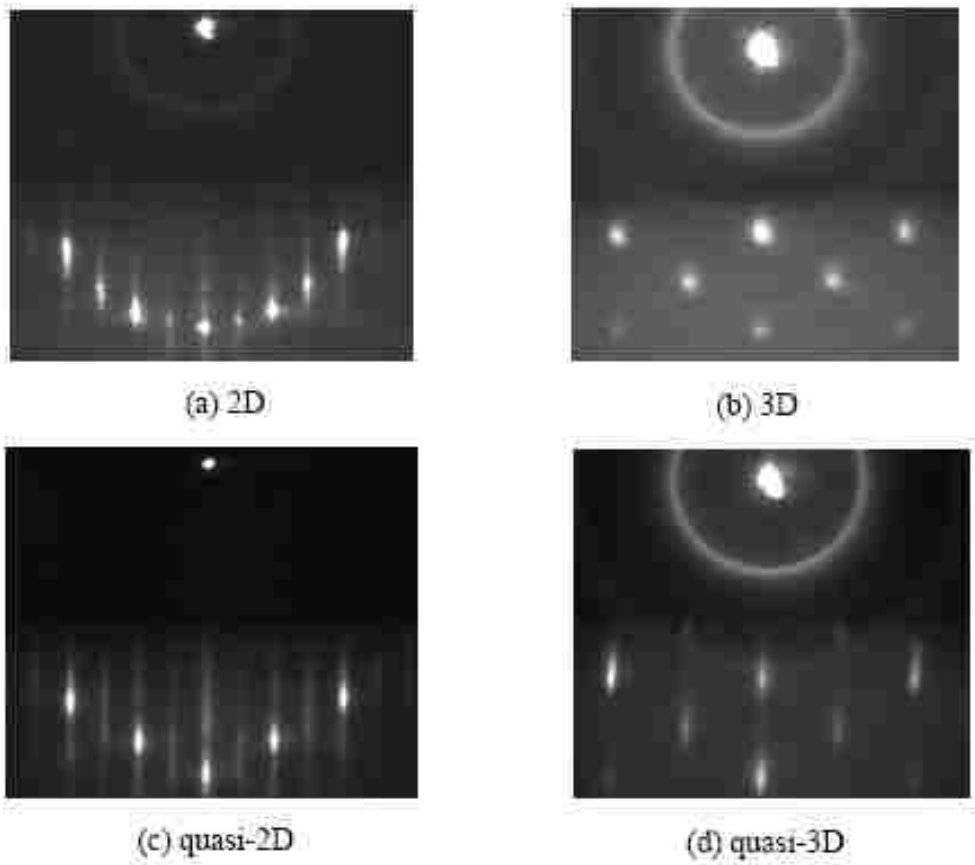

Figure 2.3. Examples of RHEED patterns for various surface morphologies, e.g. atomically smooth 2-dimensional (2D) surface and atomically rough 3D surface.

The way to monitor the growth speed counts on the intensity evolution with deposition time. This is so called intensity oscillation. If the growth mode is two dimensional, the intensity of a specific diffraction spot will have a regular oscillation pattern vs. time. In Figure 2.4, the reflectivity reaches a minimum when the coverage of surface atoms is half a monolayer, which corresponds to the roughest surface. This drop down intensity is due to the diffuse scattering. When the growth of a new monolayer is completed, the surface is significantly smoother than the half deposited surface; therefore the intensity reaches maximum again as less diffuse scattering occurs. By counting the intensity regulation

periods, we will be able to accurately figure out the layers of the unit cells deposited, thus the film thickness. The intensity of the oscillation will decreases progressively as more and more layers are deposited as the surface overall roughness is increased.

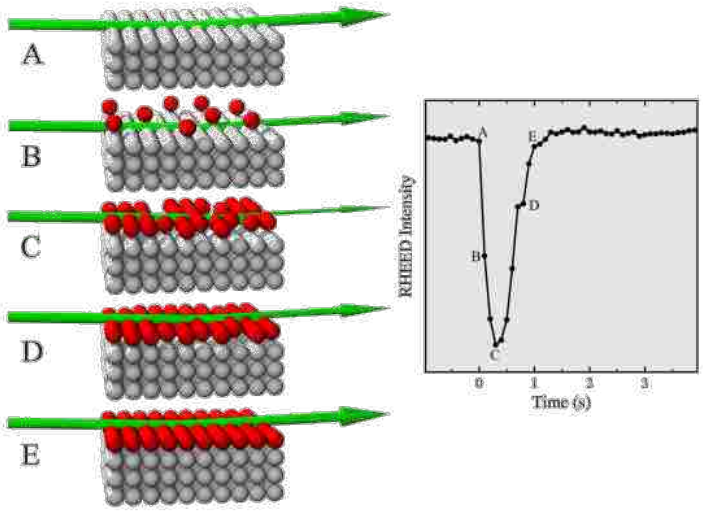

Figure 2.4. Surface models illustrating the growth of a single monolayer of film on a flat surface in layer-by-layer mode. The graph shows real measured RHEED intensity during homoepitaxial growth of a single unit cell layer of $SrTiO_3$.

2.2 Scanning tunneling microscopy (STM)

A scanning tunneling microscope (STM) is an instrument for imaging surfaces at atomic resolution. Scanning Tunneling Microscopy (STM) is one of the few inventions that took just 5 years after its invention to the Nobel Prize. It was developed by Binig and Rohrer at IBM in 1981 and proved to be a powerful tool for surface science [67]. In the setup, a sharp scanning metallic tip and a conducting sample are necessary conditions. By applying a bias voltage, the tunneling current is generated. The process can be depicted by the diagram of Figure 2.5 with (a) and (b) are macroscopic and atomic scale respectively. Another principle is the piezoelectric effect. It is this effect that allows us to precisely scan the tip with angstrom-level control.

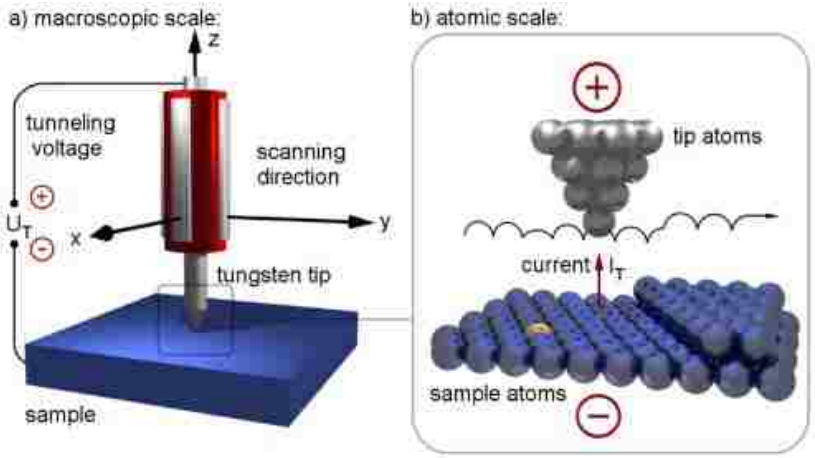

Figure 2.5. Principal of Scanning Tunneling Microscopy: Applying a negative sample voltage yields electron tunneling from occupied states at the surface into unoccupied states of the tip. Keeping the tunneling current constant while scanning the tip over the surface, the tip height follows a contour of constant local density of states.

The basic principal is quantum tunneling. The electrons in the sample tunneling through the vacuum barrier create a tunneling current I from the tip to the sample:

$$I \propto Ve^{-2kd} \tag{2.1}$$

where d is the distance between the tip end and the sample, and k is the constant related to work function in the form of

$$k = (2m\phi / \hbar^2)^{1/2} \tag{2.2}$$

where m is the electron mass, $\hbar$ is the Planck constant divided by 2π. The typical value for k is $2A^{-1}$. If the distance d is small enough, the tunneling current is measurable.

The STM setup is shown in Figure 2.6. The main part is the tip-sample configuration, which requires the atomic movement of the tip or sample. A piezoelectric scanning drive is used here and combines with the feedback loop to tracing the sample position. By plotting the distance to maintain the tunneling current, the computer is able to display a surface topology.

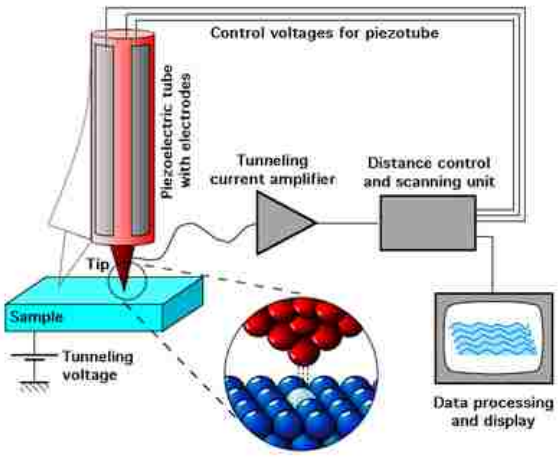

Figure 2.6. STM system set up overview

STM is not only able to "see" the atoms, but also probe the surface electron density of state (DOS). The tunneling current strongly depends on DOS of a specific sample and tip as well as very sensitively on the *d* as revealed by the following equation:

$$I \approx \frac{4\pi e}{\hbar} e^{-d\sqrt{\frac{8m\varphi}{\hbar^2}}} \rho_t(0) \int_{-eV}^{0} \rho_s(\varepsilon) d\varepsilon \tag{2.3}$$

The differential of tunneling current over bias gives rise to information of DOS：

$$\frac{dI}{dV} \propto DOS(eV) \tag{2.4}$$

The tunneling current will choose the most near atom to sample surface. A very sharp tip is critical for STM imaging. The tip can be platinum, tungsten or gold. The tip is made of tungsten in our lab since it is much more easy to obtained through electrochemical etching. We used NaOH solution to etch the wire so the portion of the tip submerged in the solution drop, leaving a sharp tip in the air. We then immediately transfer the freshly made tip to the vacuum chamber to protect the tip from contamination. See example of FeTe single crystal STM image in Figure 2.7. The sample was in-situ clearly and the

surface is (1x1) non-reconstructed tested by LEED. By measuring the distance between two bright spots, we can get the lattice constants of FeTe single crystal. Comparing with the experimental bulk measurement, we can see if the STM image reflects the electron structure or real surface morphology

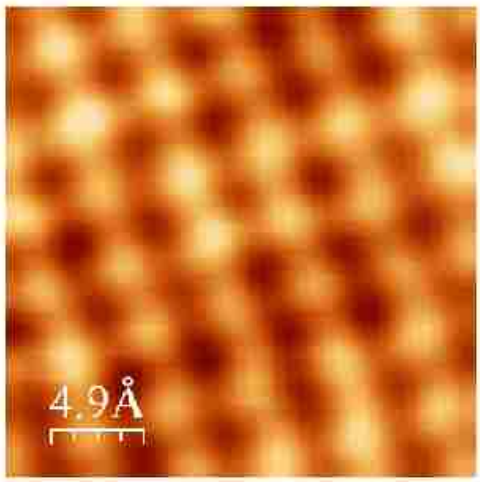

Figure 2.7. STM image of surface of single crystal FeTe (001) taken at bias voltage 1.5V at room temperature.

2.3 Low energy electron diffraction (LEED)

A beam of low energy electrons is used to form a diffraction pattern from the ordered surface atoms in the crystal or thin films make the electron see it as a grating. By analyzing the diffraction pattern, position, shape, and other features, we will be able to check the surface structure. The LEED collects the backscattered diffraction beams. As long as the electron beam energy is greater than a certain value, such as 50eV, a diffraction pattern can always be observed. As the electrons have a coherence length typically at 5-10 nm, the intensity of diffraction spots will be hard to detect due to the large background caused by incoherent scattering. Therefore a clear LEED diffraction

pattern indicates a well-ordered surface structure. The inelastic mean free path is relatively smaller for low energy electrons; the electrons beams can only penetrate into the top few layers under surface, so the LEED is very surface sensitive. Figure 2.8 is a representative LEED image for any (001) non-reconstructed surface.

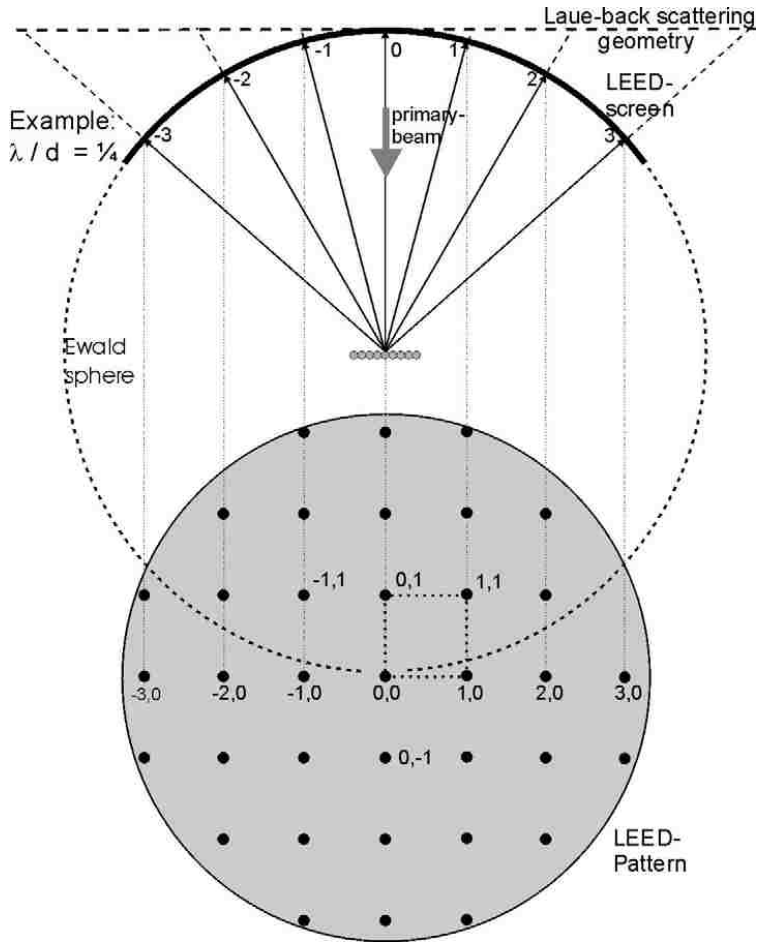

Figure 2.8. Expected LEED diffraction pattern for (001) non-reconstructed surface.

A monochromatic electron beam generated by an electron gun provides a beam of electrons with energy ranging from 20 eV-300 eV. It is normally incident on a surface; the backscattered electrons then will form specific pattern on a phosphor screen. To get enough intensity on the phosphor screen, a screen high voltage is biased on the screen to

accelerate the electrons so that high-energy electron can lighten the screen. A suppressor voltage (0-3V) is used to filter unexpected low energy electrons to reduce noise. The sample must be conductive and grounded in case of charging. LEED pattern is usually recorded with a phosphor screen and processed in a computer. In principle is reciprocal space of a sample surface. Spots are formed due to Bragg law $d\sin\theta = n\lambda$, where λ is the incident electron wavelength. According to the De Broglie relation, the wavelength of an electron is given by $\lambda = h/p = h/(2mE)^{1/2} = (150.4eV/E)^{1/2}$ where e is the electron charge and m is the mass of electron. In the case of beam energy less than 300eV, the wavelength is smaller than most of the lattice constants.

Figure 2.9 illustrates a schematic view of LEED setup. The instrument mainly includes the electron gun, florescent screen and ultra high vacuum chamber.

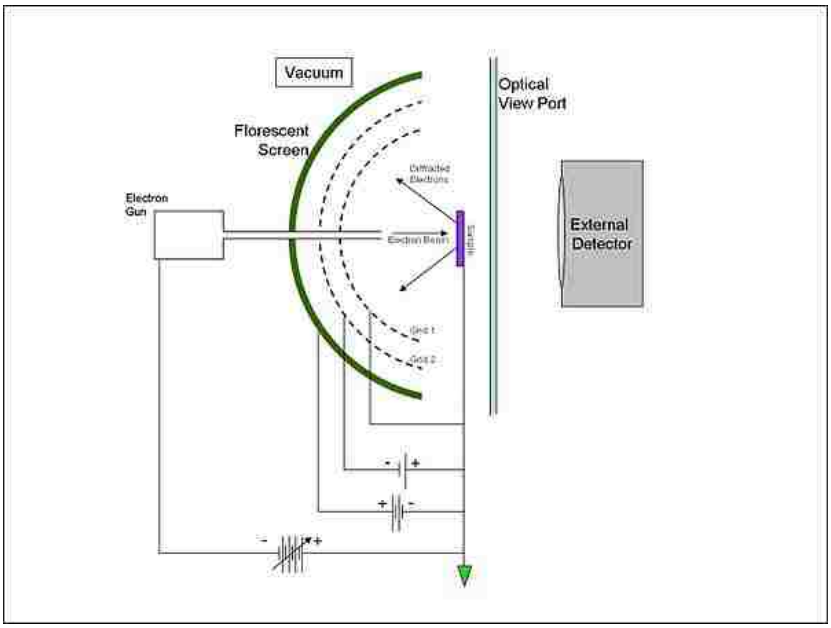

Figure 2.9. A simple sketch of the LEED apparatus.

The heart of the LEED instrument provided of company Omicron GmbH is two electrostatic octopole deflection units, which can scan the diffracted electron beam over a

single electron detector with a small entrance aperture. As a result, signal to noise ratio and resolution are dramatically improved compared to conventional, screen and camera based LEED systems, as well as allowing operation at reduced sample currents. The resulting lateral resolution is given by the transfer width of the instrument of better than 1000 Angstroms. The usable dynamic range is between 1 and 8*106 counts per second.

2.4 (Angle Resolved) X-ray photoelectron spectroscopy (ARXPS)

2.4.1 X-ray photoelectron spectroscopy (XPS)

2.4.1.1 XPS principle.

As XPS technique which has attracted a lot of interests in various research areas ranging from solid-state physics to chemistry and become a commonly used technique for studying the properties of surfaces is the major tool for my thesis project, we will describe the basic principles, the characteristics and the potential of the technique and instrumentation much deeper than previous experimental tools.

When X-ray impinges upon a solid material, the orbital electron might acquire energy from the photon energy, leading the electron excited from the surface, which is so called photoemission. The amount of electrons having escaped from the sample without energy loss is typically measured in the range of 20 to 2000 eV. This type of measurements is necessarily performed under high vacuum conditions, and only samples restricted in size can be analyzed. From this point of view, XPS cannot be considered as non-destructive techniques. The X-rays are usually produced by electron bombardments of Al and Mg anodes which can initiate the emission of $K\alpha_{1,2}(\hbar\omega = 1253.6eV)$ and $K\alpha_{1,2}(\hbar\omega = 1486.7eV)$ respectively. Both energies are sufficient to excite the core electrons of all of the elements in the periodic table. The ejected photoelectrons are

energy analyzed in a high-resolution spectrometer (Figure 2.1). One of the most important features of the photoelectrons is the energy level, which can be calculated as the peak position of drawing of the number of electrons recorded versus kinetic energy (kinetic energy E_K). A simple relation Einstein photoelectric equation connects the peak positions to specific binding energies (E_B), which is representative of the atomic species. Thus XPS provides a chemical "fingerprint" of the surface.

$$E_K = \hbar\omega - E_B - \phi \tag{2.5}$$

Where ϕ is the work function, whose precise value depends on both the sample and the spectrometer [68]. It is clear that only binding energies lower than the exciting radiation is probed. In the case of a conducting sample in electrical contact with the spectrometer, the work function ϕ is equal to the spectrometer work function $\phi_{sp}(\sim 5eV)$. In a first approximation, the work function is the difference between the energy of the Fermi level E_F and the energy of the vacuum level E_v, which is the zero point of the electron energy scale: $\phi = E_F - E_V$ (2.6)

For convenience, most commercial equipment has already calibrated the kinetic energy of the photoelectron relative to the Fermi level, which is set to the same value for both the spectrometer and the sample under the equilibrium. Therefore the binding energy value can be easily obtained through detecting the kinetic energy of ejected electrons, though the accurate position will have to be calibrated through standard sample, such as Au 4f peak whose binding energy is accurately and well known 84.0 eV. Sometimes the calibration can also be done using the mid point of Fermi Level intensity if the sample is metallic.

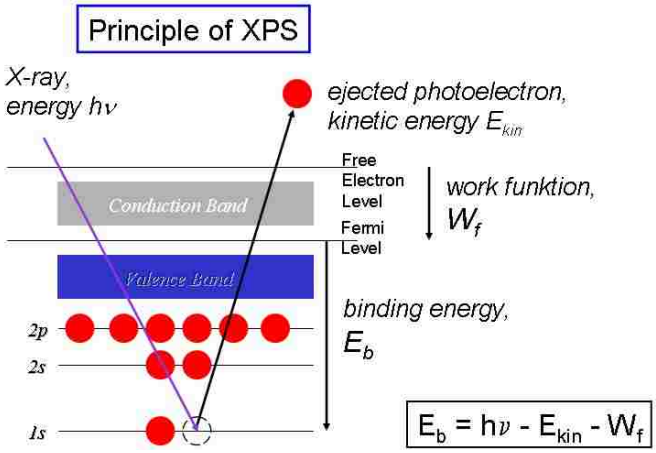

Figure 2.10. The principle of XPS experiment. The measured spectrum is quantified in peak intensities and peak positions.

2.4.1.2 X-ray photoelectron spectrum.

The primary structure of an X-ray photoelectron spectrum consist of a few basic types of peaks; (1) peaks due to photoemission from core levels, (2) those due to photoemission from valence levels, (3) peaks due to X-ray-excited Auger decay (Auger series), and (4) other peaks, such as multiplet splitting, satellite peaks, ghost peaks, electron energy plasma [69]. For example, a typical XPS spectrum of Nickel metal is shown in Figure 2.11. It is a wide scan of the electronic structure of the Gold atom [70]. The spectrum exhibits the typical appearance of sharp peaks and extended tails. The peaks correspond to the energies of the photoelectrons, which escape from the solid without undergoing energy loss. The higher energy tails correspond to energy loss of the photoelectrons, which have undergone inelastic scattering on their outward path, thus emerging with lower kinetic energy (higher binding energy).

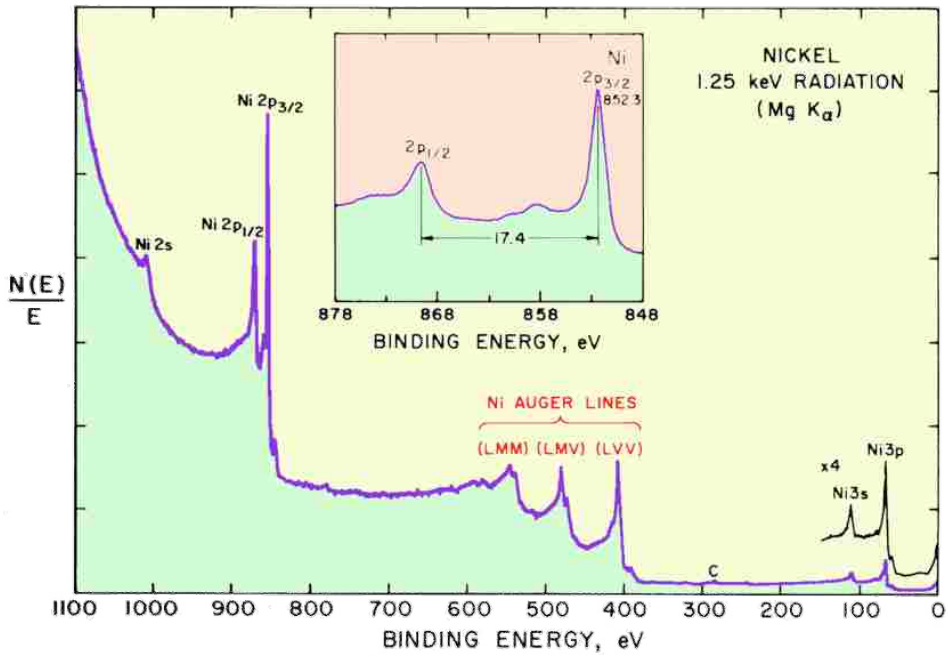

Figure 2.11. XPS spectra of metal Ni Irradiated with Mg $K\alpha_{1,2}(\hbar\omega = 1253.6eV)$.

The nomenclature employed to describe a XPS feature is based on the momenta associated with the orbiting paths of electrons around atomic nuclei, indicated by the quantum numbers *n, l, j*. XPS uses the spectroscopic notation: first the principal quantum number (n = 1, 2, 3, …), then *l* = 0, 1, 2, … indicated as s, p, d, …respectively, and finally the j value given as a suffix (1/2, 3/2, 5/2, …). It is immediately clear from the figure that the core levels have variable intensities and widths and that non-s- levels are doublets such as the $4d_{1/2}$ and $4d_{3/2}$ lines shown in the inset of Figure 2.11. The doublets arise through spin orbit (*j-j*) coupling (the spin-spin and orbit-orbit couplings are much smaller). Two possible states, characterized by the quantum *j* (*j=l+s=l±1/2*) arise when *l* *>0*. . The separation ΔE_j can be a few electron volts and it is expected to increase as Z increases for a given sub shell (constant *n, l*) or to increase as l decreases for constant n.

If the energy resolution of the spectrometer is high enough, these energy difference (spin orbit coupling) can be identified clearly. The relative intensities of the doublet peaks are roughly given by the ratio of the respective degeneracies $(2j_- + 1)/(2j_+ + 1)$ [60].

After the emission of a core electron such as 2s or 2p one from the L shell, a hole is left in the core shell. The hole can be filled by an electron from the M shell or valence band with another M or V electron carrying away the energy (auger process). We can clearly see the LMN, LMV, and LVV auger lines in the Figure 2.11. The line width, which is defined as the full width at half-maximum intensity (FWHM) of Auger peak, is larger than XPS peak due to the electron transition process is shorter in photoemission process. Typically, people use Auger lines in element identification because the energy of Auger lines is independent of the incident photon energy.

Satellite peaks mainly refers to shake up/off satellites peaks. Another well known satellite peak introduced by multiple X ray photon energy is not going to be discussed because our monochromatic source exhibits a primary characteristic X-ray source by getting riding of $K\alpha'$, $K\alpha_3$ etc. When the core hole is created by photoemission, other electrons relax in energy to lower energy states to screen this hole partially and therefore make more energy to the emitted photoelectrons. Once photoelectron is excited from an atom at an excited state, the kinetic energy is smaller than that of corresponding atom at the grounding state. Such a peak near the main core level peak is called shake up satellite. The binding energy difference between the satellite peak and main peak can vary from one tenth of eV to visible order of 10 eV. So the satellite peak is an important signature of electron correlation which is widely discussed topic in the oxides materials. We will have a few examples to be laid out in later chapters.

2.4.1.3 Quantitative analysis

Background subtraction. Prior to quantitative evaluation, proper determination of intensity for the photoelectron line is essential. In XPS, the peak intensity represents the total intensity of the photoelectrons emitted from a core level, which is measured by the total area of the peak. The generated photoelectrons of a characteristic peak will undergo different inelastic interactions with the electrons in the solid sample producing a continuous background at higher binding energy side of a photoelectron line. The accurate intensity of a specific peak can only be achieved by subtracting the background carefully. Some of the background subtractions are easy but not with others shake-up, shake-off and multiple splitting which leads to extending features over a wide energy range. There are several methods to do the subtraction, 1) linear background [71], 2) Tougarrd background and [72] 3) Shirley background [73]. Looking at Figure 2.11, the lower binding energy part of the whole scan can use linear background subtraction, while different background is displayed for higher binding energy part. How to interpret this rapid change of background resulting from the energy loss process?

The most common method used to model the background is so called Shirley background [5]. The essential feature of the Shirley algorithm is the iterative determination of a background using the areas marked A1 and A2 in Figure 2.12 to compute the background intensity *S(E)* at energy E: The Shirley background is described as equation:

$$S(E) = I_2 + \kappa \frac{A2(E)}{(A1(E) + A2(E))} \tag{2.7}$$

Where E_1 and E_2 are two distinct energies and I_1 and I_2 are two intensity values usually chosen to cause the background to merge with the spectral bins at E_1 and E_2. κ defines the

step in the background and is typically equal to ($I_1 - I_2$). $S(E)$ is unknown initially and calculated by a iterative process. This theoretical calculation might cause some problem when the algorithm produces a background curve that cuts through the data. In this case the Shirley background in clearly wrong because it does not make any physical sense. Therefore a modified Shirley background or other background methods are necessary.

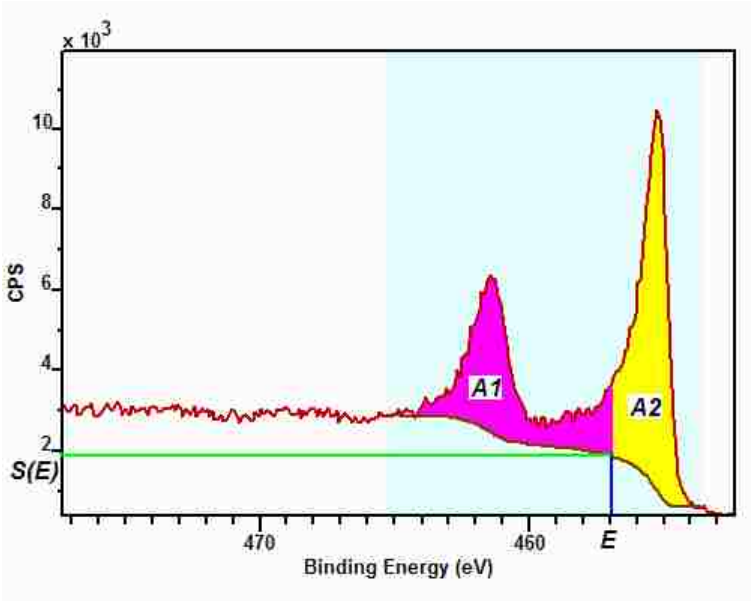

Figure 2.12. A Shirley background computed from a Ti 2p spectrum.

Tougaard background subtraction has been developed to model the background. It explains the elastic and inelastic loss of the secondary electrons also in an iterative way as Shirley method. The essence of Tougaard method is energy loss cross-section function, which is the probability of electron at an offset energy, contributes to the background. However, the Tougaard method is not very correct comparing with Shirley or corrected Shirley one because the cross section can only be used generally in concept or qualitatively analyzed. Nevertheless, the Tougaard is used when it is appropriate to describe. Typically the choice of background subtraction is to be made by the software. Our experience is that Shirley background is used most frequently.

Curve fitting. Before we discussed the curve fitting of a peak, we need to notice that some spectra have multiple peaks overlap due to small binding energy difference. The better energy resolution is, the easier to identify the single peaks. The overlap can come from the multiple core levels with close energy positions. In some cases, one atom existing in the solid has different chemical environments, leading to existence of multiple peaks. Most of the peaks displayed a wide bump at higher binding side that is understood as the surface components. After the background subtraction, the first thing that needs to be done is the peak fitting procedure to resolve the peak parameter. In reality, the quality of experiments results depends on how we smooth the curve especially in the case of high noise level. First of all, there are few basic rules to fit the curves. For the line width, the intrinsic X-ray source contribution is lorentzian line shape; the peak width due to the core hole lifetime is calculated by Heisenberg's uncertainty relationship $2\pi\hbar/\tau$; the analyzer resolution, which broadens the line width, is Gaussian type. We shall keep in mind that the intrinsic line width is bigger for deeper core levels as the core lifetime is shorter. As the overall line shape of a peak is mixture of Gaussian and Lorentzian shapes requiring a careful analysis. The asymmetric tail caused by the process when the photoelectron transfer its kinetic energy to excite the valence electrons can be fit with Doniach-Sunjic function. Our software setup provides a good tool to analyze the curve using Doniach-Sunjic behavior easily. After applying these basic rules, we have to guess a few initial parameters of line width, intensity, positions etc. and input them to the XPS software. A few trial and correction process have to be enacted to finally achieve a relatively good fit. The final fit must be consistent with all other available information so it is best to start with initial parameters carefully and cautiously.

Chemical shift. Another concept to discuss here is chemical shift. We frequently observe binding energy shifts in the core level peaks. The shift magnitude is from one tenth of eV or a few eVs for different systems. Understanding these shifts is important to study the composition, structure and chemical environment. There are several factors that can contribute to the binding energy shift for a specific core level. For example, a change in the chemical environment will affect the valence state of the atoms and thus change the core levels. Pure Silicon Si 2p peak will have lower binding energy than the oxidized Si. This is so called chemical shift. As the basic information about the chemical environment and element concentration in the sample can be extracted from the primary structure, the small chemical shifts in binding energy are difficult to determine in advance. XPS measures the energy difference between the total energies of an initial state with N electrons $E_i(N)$ and a final state with N-1 electrons $E_f(N-1)$. Thus the binding energy is simply defined as the difference between two states energy:

$$E_B = E_f(N-1) - E_i(N) \tag{2.8}$$

The initial state is the state of atom prior to the photoemission process. If the energy of the atom's initial state is changed by the formation of chemical bonds with other atoms, the E_B of the electron in that atom will also change. This definition of Binding Energy has the disadvantage that total energies are not easy to calculate from first principles, and one has to rely on approximations to obtain them or use the experimental results for standard materials. Koopman's approximation [74] states that the binding energy equals to the negative energy of the orbital from which the photoelectron is emitted. However in reality, Koopman's energy is never observed. The main reason for this is the relaxation shift. When the core hole is created by photoemission, other electrons relax in energy to

lower energy states to screen this hole partially and so make more energy available to the outgoing photoelectrons. In the case of a free atom, the final state maybe one in which an electron is in an excited bound state, or in which another electron is ejected into the continuum. Such process leaves less energy for the emitted photoelectron and this gives rise to lower kinetic energy satellites; these are usually referred to as shake-up satellites (when excitation is to a bound state) and shake-off (when excitation to the continuum). In a solid this relaxation energy consists of two basic contributions. One results from the relaxation of the orbitals on the same atom (intra-atomic relaxation) discussed above. The other one is due to charge flow from the crystal onto the ion that caries the hole (inter-atomic relaxation), which can lead to plasmon losses. Thus XPS always measures final-state energies which can be related to initial-state energies only after some careful considerations.

The chemical shifts are typically a few to 10 eV or more. To extract chemical information, it is imperative to determine peak positions as accurately as possible. The interest is preferentially evoked by means of a monochromatic X-ray source, and recorded with the highest possible energy resolution. When dealing with small chemical shifts, overlapping peaks may occur in the spectra. Peak deconvolution and peak fitting tools are available in the commercial data handling systems. An illustration is seen in Figure 2.13, where the C 1s peak is deconvoluted in its components. Three different carbon chemical bonding can be clearly identified. The energy differences can be as big as an order of eV. The line width also varies depending on the lifetime of the photoelectrons coming from the specific core levels.

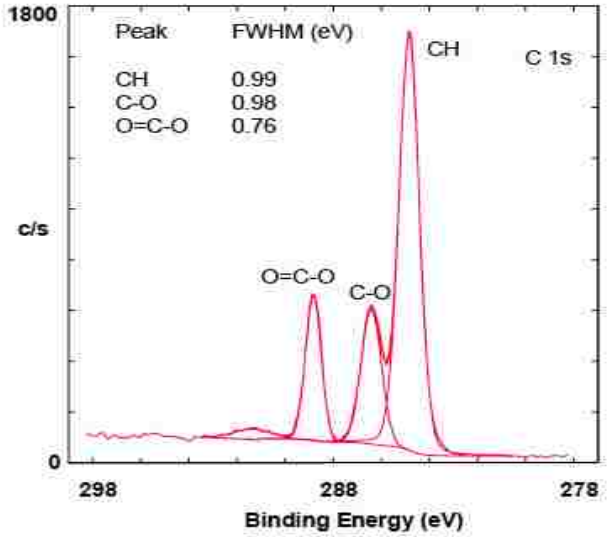

Figure 2.13: Chemical shift of the C 1s peak as a function of its bonding with O.

2.4.1.4 Experimental details

The electron spectrometer and sample room must be operating under ultra high vacuum (UHV), typically in the range of 10^{-8} to 10^{-10} torr. The reason for this is two fold. The low energy electrons are elastically and non-elastically scattered by residual gas molecules leading to a loss of intensity and of energy so that not only the intensity of the peaks is affected but also the noise in the spectrum increases. The second reason is that lowering the vacuum level to e.g. 10^{-6} torr would immediately lead to the formation of a monolayer of residual gas absorbed on the sample surface in less than a second. A vacuum of 10^{-10} torr allows measurements to be carried out for about an hour before a mono film is formed. The fact that AES and XPS are methods achieving a depth resolution of a few nanometers with a detection limit lower than 1% of a monolayer, clearly establishes the high requirements on the vacuum. Even in the case of a vacuum of 10^{-10} torr, typically carbon peaks are found as a result of surface contamination.

A typical XPS setup is shown in Figure 2.14. The main components of the setup include the X ray source, Monochromator, X ray Hemispherical Sector Analyzer and Detector. The X ray source is generated from Electron bombardment on various anodes, such as Aluminum. The purpose of Monochromator is to focus the X ray beam to achieve better resolution of spectra. The X-ray line width can be reduced to 0.15 eV by using a monochromator. It is based on Bragg reflection of the X-rays on single crystal, e.g. natural quartz, as shown in Figure 2.14. The quartz crystal is placed on the surface of a Rowland or focusing sphere, together with the anode and the sample. The X-rays are dispersed by diffraction on the crystal and re focused on the sample surface. Other benefits are the removal of contributions to the XPS spectrum of satellite peaks and of the Bremsstrahlung continuum coming from the X-ray spectrum of the anode. The drawback of the use of a monochromator is a severe loss in intensity of the primary X-rays. Besides focusing the X-rays through a monochromator, we also used an aperture system in order to select only a fraction of the emitted photoelectrons for detection.

The HSA is designed to have a constant and as high as possible energy resolution for the detection of photoelectrons. The best energy resolution in XPS is 0.15 eV, corresponding to the line width of the monochromator. In order to reduce the size of the analyzer, it is standard practice to retard the kinetic energies of the photoelectrons either to user-selected analyzer energy, called pass energy. The first mode is called fixed analyzer transmission mode (FAT)). In this mode of operation, which is applied for the detection of photoelectrons, a constant voltage is applied across the hemispheres allowing electrons of a particular energy to pass between them. The most important characteristic in this case is a constant energy resolution in the spectrum as a function of the energy.

The electrons are emitted from the specimen and transferred to the focal point of the analyzer by the lens system. At this point they are retarded electrostatically before entering the analyzer itself. Those electrons with energies matching the pass energy of the analyzer are transmitted, detected and counted by the electron detector. The retarding field potential is then ramped, and so the electrons are counted as function of energy. To improve the sensitivity of the HSA, the electron detection is done by a multichannel detector system. Depending on the type of system, the number of electron multipliers may go up to 16. This parallel electron detection is especially useful when a monochromator is used due to the loss of intensity of the primary X-rays.

All of our XPS measurements were carried out with a Phoibos 150 MCD Energy Hemispherical Analyzer provided by Specs GmbH using photon energy of 1486.74 eV from a Specs Micro-Focus 500 ellipsoidal crystal Mono-chromator with Al α x-ray source and focusing x-ray spot capabilities, a pass energy of 30 eV. The step energy in the spectra is 0.01ev. The overall energy resolution for the XPS spectra is 0.16 eV. The base pressure of our system during the measurements was better than $2e10^{-9}$ Torr.

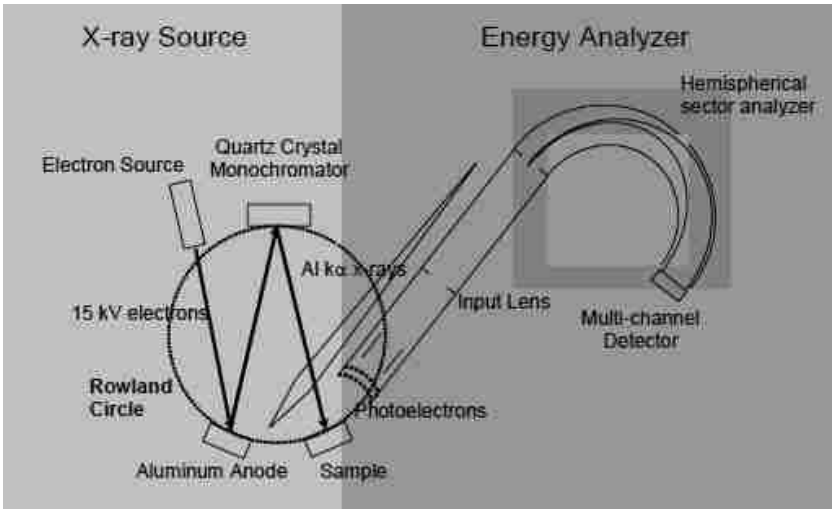

Figure 2.14: Schematic representation of an XPS set-up with a hemispherical analyzer.

2.4.2 Methodology of surface composition determination

2.4.2.1 XPS surface sensitivity of core level spectra.

As we have shown in chapter one, surface properties differ tremendously from the bulk due to the broken symmetry. We should expect that the chemical bonding and electronic energy levels are quite different for the surface. The photoelectrons emitted from solids will exhibit combined bonding information of both surface and bulk; here we use ARXPS to extract the surface information from it.

The surface sensitivity of the photoelectron spectroscopy is defined as the ratio of surface to bulk signal. It does not only depend on the penetrating depth of the incident radiation but upon the probability that photoelectron will be able to escape from the surface. According to the Beer-Lambert law, the probability of an electron travelling a distance d through a solid without undergoing inelastic scattering is given by:

$$P(d) = \exp(-d / \lambda(E)) \tag{2.9}$$

Where λ is the Inelastic Mean Free Path (IMFP). Calculation can be done to show 95% of the detected electrons are within 3λ from the surface. Therefore the shorter of the λ, the better surface sensitivity can be achieved. Also we can increase the probability *P* by tuning the energy of X-ray radiation and detecting the photoelectron emission at higher emission angle with respect to the surface normal. Intuitively it is not difficult to understand hard X-ray radiation will increase the intensity of detected electrons as they carry higher kinetic energy, but this requires synchrotron that allows the variation of beam energy. What we can do with our fixed Aluminum anode source setup is changing the emission angles. In this case, the 95% of the detected electrons will come from within $3\lambda\cos\theta$ of the surface. This method is the basis of the angle resolved X-ray

photoelectron spectroscopy. Fadley and Bergstrom [75] introduced this method and people started to use this to distinguish between surface and bulk compositions. The first method for obtaining concentration depth profiles by ARXPS was proposed by Pijolat and Hollinge [76]. Considering the layered compounds, the quantification of XPS data (the intensity of j peak of i element) can be written as

$$I_{ij} = K \cdot T(E) \cdot L_{ij}(\gamma) \cdot \sigma_{ij} \cdot \int n_i(z) \cdot e^{-z/\lambda(E)\cos\theta} dz \cdot \tag{2.10}$$

θ is the emission angle with respect to the surface normal, λ is the IMFP of the photoelectron with the appropriate kinetic energy, the T (E) is the electron transmission function, the σ_{ij} is the photoionization cross sections. It is not difficult to tell from equation 2.10, the intensity of a specific core level will show exponential decay with emission angle. In reality when we measure the peak intensity to comparison, we need to make sure the background is subtracted to calculate the area under the peak and the method used to substrate should be consistent each time.

Since the XPS spectra peak consists of the elastically scattered electrons, we will need to know the inelastic mean free path (IMFP) $\lambda(E)$, which is dependent on the kinetic energy E, and the specific materials. For Al K_α radiation, most of IMFP falls into range of 1-3.5nm (a few unit cells for most layered compounds). The experimental IMFP curve exhibits a minimum point for electrons with kinetic energies of around 50-100 eV. The reason is that the electron has less possibility to cause plasmon excitation at low energies; and therefore the IMFP increases with kinetic energies. We will introduce some theoretical studies to model the

IMFP with one form [8] generally calculate the IMFP. Once we have the estimated IMFP value, the sampling depth will be 3 λ where 95% of electrons are escaped without losing energy. Of course in reality, we will be able to detect much deeper depth for a solid as we can see the binding energy peak is broadened.

2.4.2.2 Basic setup of ARXPS

The analyzer is permanently mounted on the chamber in a perpendicular direction. To change the photoelectron detection angels, we shall rotate the sample in a polar direction, not azimuthally. Figure 2.15 provides an illustration of the changing detection angles of the photoelectron showing the angle dependence of penetration depth.

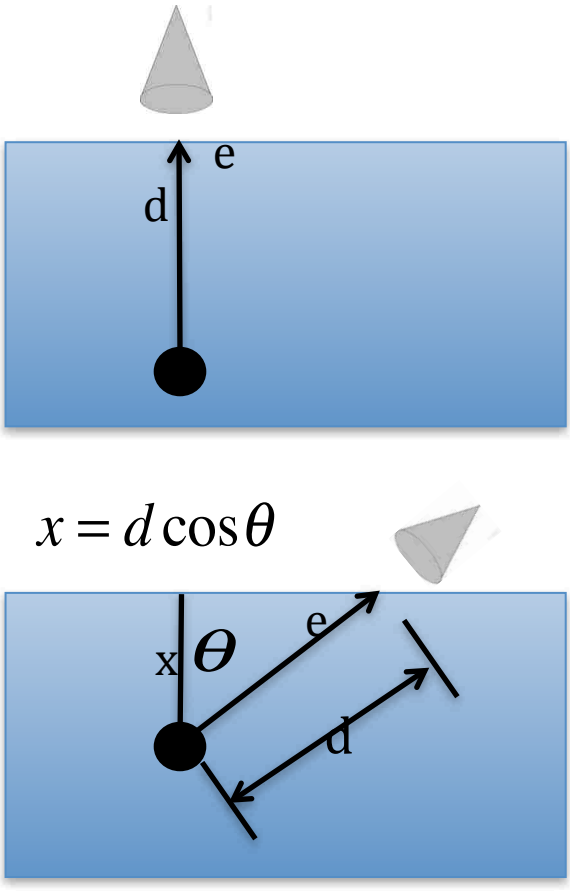

Figure 2.15. Schematic illustration of changing photoelectron detection angles using commercial XPS setup.

By detecting the photoelectrons intensity at higher angles θ, the sampling distance scales to $\cos\theta$. ARXPS method was first proposed by Bergstrom [77], and for instance, more and more scholars contribute to the applications of this methods [77,78]. Figure 2.16(a) is an example of the XPS spectra changes by varying the emission angle [79]. The biding energies of two peaks do not depend on the emission angles. It is clear from the As 3d spectra that the oxide peak (at higher binding energy) is dominant at the surface whereas the peak due to arsenic in the form of GaAs (at lower binding energy) is more dominant at near normal analysis angles. Figure 2.16 (b) shows schematically shows XPS data are collected from the metal at two angles, near normal (the "bulk angle") and neargrazing (the "surface angle"). Near normal emission produces a spectrum in which the metal peak dominates while the oxide peak dominates in the spectrum from the grazing emission.

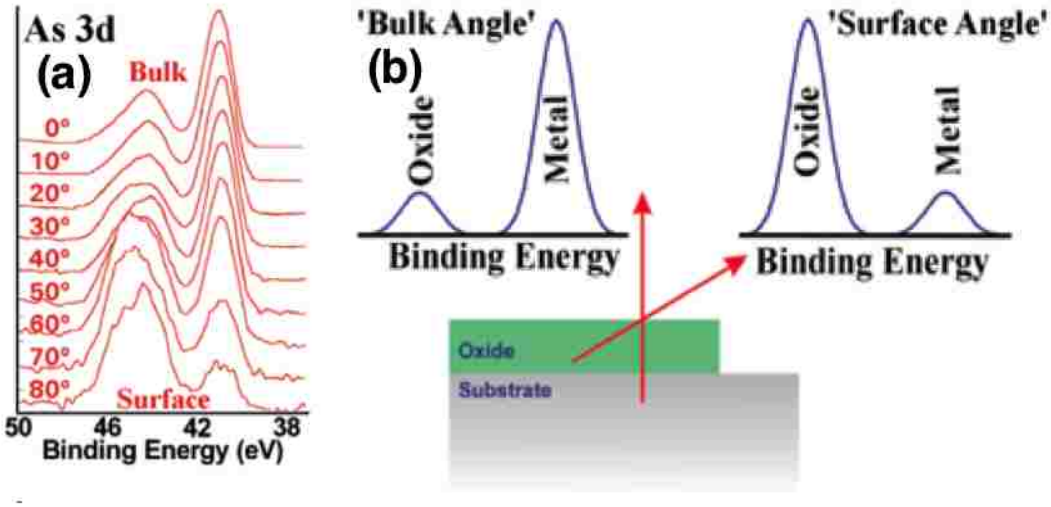

Figure 2.16. a) Effect of variation of emission angle on the As spectrum with a passive oxide layer. b) An illustration of the analysis of a thin metal oxide on a metal substrate. The diagrammatic spectra show the effect of the collection angle on the elemental and oxide peaks of the metal. (Reference 81)

CHAPTER 3. CHEMICAL COMPOSITION CHARACTERIZATION WITH ARXPS

3.1 ARXPS intensity calculation

The contribution to the photoemission intensity of an infinitesimal thick layer at depth z from the surface can be expressed as follows:

$$dI = \phi T(E) n e^{-jd/\lambda(E)Cos(\theta)} \sigma dz \tag{3.1}$$

We define the probability $P(\lambda, z, \theta) = e^{-\frac{z}{\lambda \cos\theta}}$ (3.2)

and ϕ is the photon flux.

T(E) is the analyzer transmission function that depends on the kinetic energy (old electron analyzer could have different sensitivity at different E_k);

σ is the photoelectron cross section that depends on the atomic species, the electronic level (i.e. 1s, 2s, 2p...) and the photon energy;

n is the number of atoms per unit volume per sampling area, that can depend on the X-ray focalization on the sample and/or on the analyzer focus;

$P(\lambda, z, \theta)$ is the probability of an electron at depth z to escape from the specimen and to reach the analyzer placed at an angle θ relative to the sample normal; λ is the IMFP and depends on the sample composition and on the E_k.

When dealing with the ratio of two element spectra only, the photon flux and sampling area can be discarded since they are contributing in the same way to each photoelectron peak. When measuring XPS peaks with close kinetic energy (or with a well calibrated analyzer) also the *T(E)* term can be neglected. Other parameters have to be taken into account to carefully quantify the elements concentration; Assume the transmission T (E) has no relation with Energy, in a simple model, ignoring the L_{ij} term(angular asymmetric factor) and we get

$$\frac{I_A(\theta)}{I_B(\theta)} = \frac{\sum_j n_A e^{-jd/\lambda_A(E)Cos(\theta)}}{\sum_j n_B e^{-jd/\lambda_B(E)Cos(\theta)}} \cdot \frac{\sigma_A}{\sigma_B} \tag{3.3}$$

The reason why we use relative intensity ratios instead of the absolute calculation is to rule out the system instrument errors, such as the X ray flux variation, detector efficiency, different pass energy setting etc. Here A and B represent two elements. The letter *d* is the interlayer spacing. The cross section can be achieved from the Spec library database. There are some calculated values to be referenced as well [Figure 3.1]. The mean free path can be estimated though TPP-2M method in the following equations as discussed in chapter 2. Notice that A, B does not need to be on the same layer.

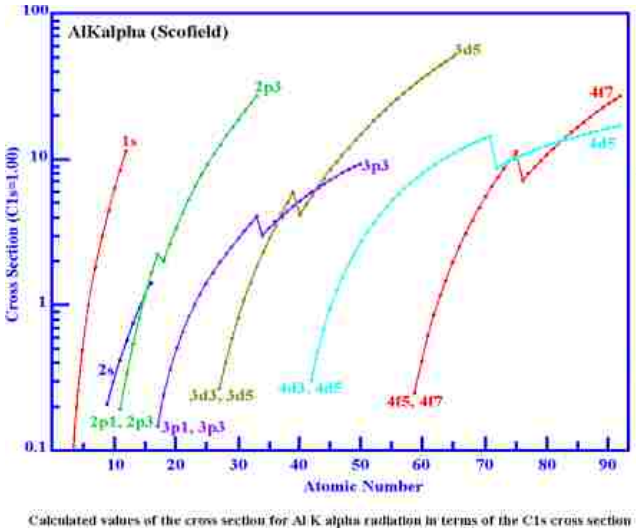

Figure 3.1. Calculated values of the cross section for Al K_α radiation in terms of the C1s cross section.

The TPP-2M predictive equation for the IMFP, λ, as a function of electron energy, *E* (eV) s described as:

$$\lambda = \frac{E}{E_p^2[\beta \ln(\gamma E) - (C/E) + (D/E^2)]} \tag{3.4}$$

The parameters to calculate the IMFP include the following:

$$\begin{aligned}
&\beta = -0.10 + 0.944(E_p^2 + E_g^2)^{-1/2} + 0.069\rho^{0.1} \\
&\gamma = 0.191\rho^{-1/2} \\
&C = 1.97 - 0.91U \\
&D = 53.4 - 20.8U \\
&U = N_v\rho / M = E_p^2 / 829.4
\end{aligned} \tag{3.5}$$

where $E_p = 28.8(N_v\rho / M)^{1/2}$ is the free- electron Plasmon energy (in eV), N_v is the number of valence electrons per atom (for elemental solids) or molecule (for compounds), ρ is the density (in g.cm^{-3}), M is the atomic or molecular weight and E_g is the band gap energy (in eV). For a specific system, we can either measure or refer the data from the synthesized materials.

Being able to calculate the IMFP, we can easily plot the curve of intensity ratio with the change of emission angle. Especially at high emission angle, which reflects mainly the surface layers, the intensity ratio can really tell us the chemical composition compared to the bulk (small emission angle).

Hani Dulli *et. al.* studied the surface chemical composition of thin film $La_{0.65}Sr_{0.35}MnO_3$ by ARXPS [80]. The surfaces have Sr segregation and restructuring happen which can be characterized by the formation of Ruddelsden-Popper phase $(La,Sr)_{n+1}Mn_nO_{3n+1}$ with n=1 occurs. The angular dependence of Sr/La ratio is shown in Figure 3.2. If the relative concentration of Sr with respect to that of La was independent of the depth into the sample the Sr/La ratio would be roughly constant. It is clear from Figure 3.2 that this ratio is not constant but it is increasing with increasing emission angle. Qualitatively this shows that the surface region is Sr rich. It also shows a fairly small decrease in Mn/Sr ratio, which can be also attributed to the increase in surface

concentration of Sr. The Mn/La ratio is increasing with the emission angle. Finally this angular dependence XPS data was used to quantitatively analyze the surface composition altered by Sr segregation. By applying the XPS core level intensity function (equation 3.2) and estimated surface layer, it turned out the best fit for the possible stacking sequences of LSMO is that of $(La_{0.65}Sr_{0.35})_2MnO_4$ with La/SrO termination [Figure 3.3]. My other studies of LEED and ISS indicate there is no surface reconstruction and the surface is mainly SrO. This conflicting conclusion results from the big errors without considering the diffraction.

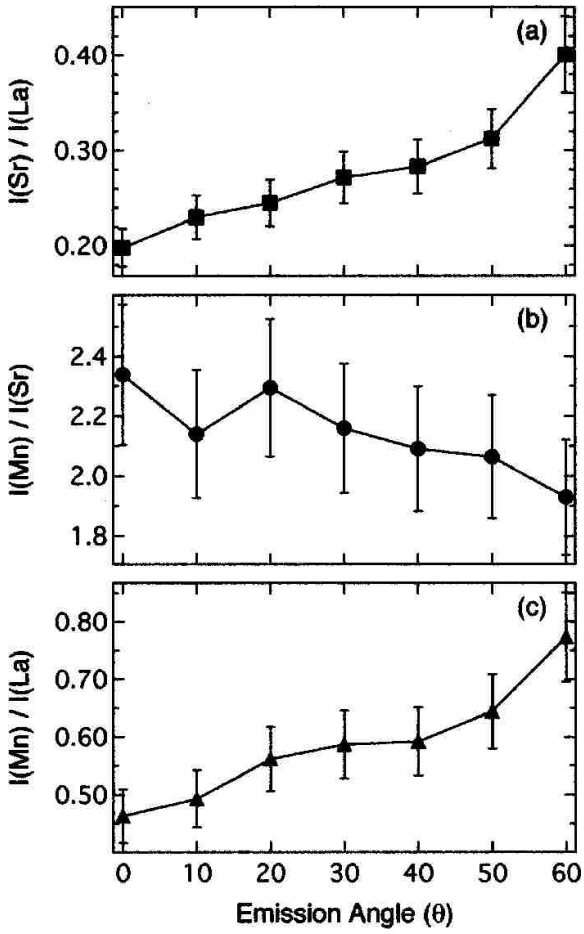

Figure 3.2. Relative intensities of (Sr $3d_{5/2}$ + Sr $3d_{3/2}$) to La $3d_{5/2}$, Mn $2p_{3/2}$ to Sr $3d_{5/2}$+Sr $3d_{3/2}$), and Mn $2p_{3/2}$ to La $3d_{5/2}$ all as functions of the emission angle.

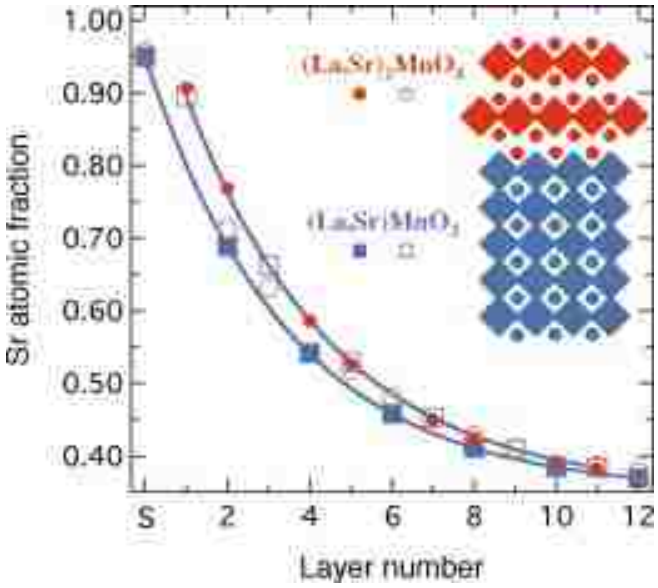

Figure 3.3. The blue solid open squares represent the Sr atomic fraction per layer for the perovskite structure of $La_{0.65}Sr_{0.35}MnO_3$ with La/SrO (MnO_2) termination. The red open solid circles represent the Sr atomic fraction for the K_2NiF_4 structure of $(La_{0.65}Sr_{0.35})_2MnO_4$ with La/SrO (MnO_2) termination.

The study from the above group has certain errors as the intensity modulation due to photoelectron effect was not considered. Without considering the diffraction effect of X-ray photoelectron, the analysis and the theoretical model is not so accurate to point to a conclusion. Nevertheless, the applications of ARXPS prove to be a useful tool to study the surface composition especially for the layered ordered structures. Understanding the surface composition and structure pave the way of probing the electronic properties of the materials.

3.2 X-Ray photoelectron diffraction (XPD)

There is angular effect important in XPS. For a clean single crystal surfaces, oscillations can be observed in the absolute core level peak intensity as electron emission angle is varied. These oscillations are attributed to constructive and destructive interferences between the coherent components of the photoelectron waves. More specifically, forward scattering is observed where the photoemission intensity enhanced

along principal crystal axes. Analysis of the photoelectron diffraction plots can offer insight into the interatomic spacing in the uppermost few atomic layers, thus X-ray photoelectron diffraction is often used to reveal the local atomic geometry (crystal symmetry, interatomic distances, bond lengths and angles) of the system under investigation. Long-range order is not required. High energy-resolution photoemission with synchrotron radiation allows us to combine chemical sensitivity to non-equivalent atomic species and structural information.

Figure 3.2 shows a clear picture of the Sr content enhancement at surface. While the explanation of the modulation at low emission angle was not explained clearly. Without simulation of the modulation in the intensity ratio fitting, it is difficult to get an accurate result of real bulk structure contribution to the intensity ratio. We propose those fluctuation can help to understand the surface structure of components. The first reported example is in a NaCl crystal by varying the photoelectron emission angles [81]. After then, more and more scientists reported the X-ray photoelectron diffraction pattern. Au 4f core level intensity modulation was reported by Fadley [75] in both polar and azimuthal directions. The theoretical framework of photoelectron includes the electron channeling theory [82,83,84], single scattering [85, 86], and multiple scattering theory[87,88,89]. The most important concept introduced is forward scattering both theoretically and experimentally confirmed [90,91,92,93,94,95]. The photoelectron current is intensified in the directions of the crystal axes because the photoelectrons are forward scattered by the negative potentials of the atoms in the lattice. The wave function $\phi_k(r)$ of photoelectron scattered by a single atom can be expressed as [96]:

$$\phi_k(r) \to \exp(ikz) + \frac{f(\theta)}{r}\exp(ikr) \tag{3.6}$$

where $f(\theta)$ is the scattering amplitude. If the electron has velocity v, and atomic number is Z, the $f(\theta)$ can be written by the first born approximation as

$$f^{(1)}(\theta) = \frac{e^2}{2mv^2}[Z - A(\theta)]\frac{1}{\sin^2(\theta/2)} \tag{3.7}$$

where e and m are the charge and electron mass respectively; here

$$A(\theta) = 4\pi\int_0^\infty \frac{\sin Kr}{Kr}\rho(r)r^2 dr \tag{3.8}$$

K is defined as the change of the electron momentum before and after the scattering as $K = \frac{4\pi mv}{h}\sin\frac{\theta}{2}$. As the electron density $\rho(r)$ can be calculated from Hartree Fock Slater wave functions [97], the forward scattering amplitude $f(\theta)$ at small scattering angle (close to zero) can be roughly written as $f(\theta^0) = \frac{1}{3}\int_0^\infty 4\pi\rho(r)r^4\, dr = \frac{1}{3}Z < r^2 >$, here $Z = \int_0^\infty 4\pi\rho(r)r^2\, dr$.

Figure 3.4 is the schematic drawing of first approximation scattering amplitude. From this figure, we can deduct that the full width at half maximum (FWHM) of the profile is smaller for higher kinetic energy. For small θ which is close to forward scattering angle, the scattering magnitude is much stronger than large scattering angle (back scattering). Typically back scattering is only considered for electrons with smaller kinetic energies. The multiple scattering is also not considered because of the defocusing effect. Therefore, the photoelectron diffraction peaks coincide with the crystal axes in real space.

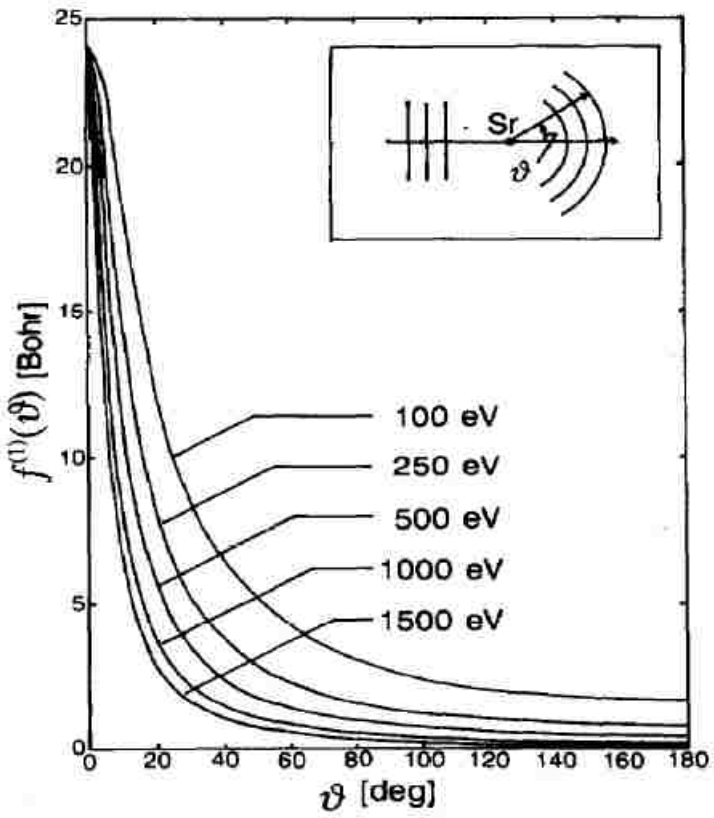

Figure 3.4. Profiles of scattering amplitude $f^{(1)}(\theta)$ at different electron kinetic energies.

The de Broglie wavelength of an electron with kinetic energy E is written as $\lambda = 12.3/\sqrt{E}$, with this in mind, the wave length calculated if kinetic energy is in the 200-1000 eV range will be comparable with the atomic lattice constant. This will make us expect the interaction of photoelectrons with lattice. The forward scattering amplitude is one order of magnitude greater than the back scattering amplitude, therefore, the X-Ray photoelectron patterns represent the surface crystal structure of single crystal in real space. LEED as introduced in the previous chapter basically provide similar information as X-ray photoelectron diffraction because it is also scattered by the atomic potential. However as LEED energy is in the range of 50-300 eV, the backscattering amplitude

cannot be neglected and multiple scattering must be considered. The complexity makes the X-ray photoelectron diffraction study the most promising tool for surface composition analysis. LEED is mainly used for surface structure analysis.

Zero degree forward scattering involves no path length difference between the direct and scattered waves, so interference is construction in the direction. However if we measure the peak intensity at a different scattering angle, the phase shift introduces the destructive interference. Both the interference effect and angle dependent cross section produce modulation of electron flux as a function of emission angle. This can clearly offer a method to determine the interatomic directions for the solid surface and the orientation of the intratomic bond angles within a solid. Though we have kept mentioning the X ray photoelectron diffraction, the qualitative determination of the intratomic bond angles have nothing to do with diffraction at all. Basically this is zero order diffraction or it is like a straight through beam in a grating. In the simplest single scattering picture, the maxima of these holographic fringes should appear when the following equation is satisfied:

$$2\pi m = \left[\frac{2\pi}{\lambda_e}\right] d_{sc}(1-\cos\theta) + \varphi_{sc}, m = 1,2... \tag{3.9}$$

where λ_e is the electron de Broglie wavelength, d_{sc} is the distance between emitter and a given scatterer, and φ_{sc} is the phase shift associated with the scattering process, often small compared to the first term in Equation 3.9.

Due to the ionic size, thermal broadening effect and the detector aperture angle, we can expect the diffraction intensity curve with the emission angle is not a delta function.

For atom size braodenging effect, the typical spectra can be described as a Gaussian function $I=I_0\exp(-2(\theta-\theta_0)^2/\beta^2)$. The thermal broadening parameter is described as follows:

$$B = 0.9\lambda / (t\cos\theta)$$
$$\beta = B / (2sqrt[2\ln(2)] = B / 2.3548$$

Here λ is the electron wavelength (Å), t is the average crystallite size (Å), and θ is the diffraction angle. However the thermal broadening is very small comparing the aperture angle, therefore we simply choose β=2.34 as the curve broadening coefficient.

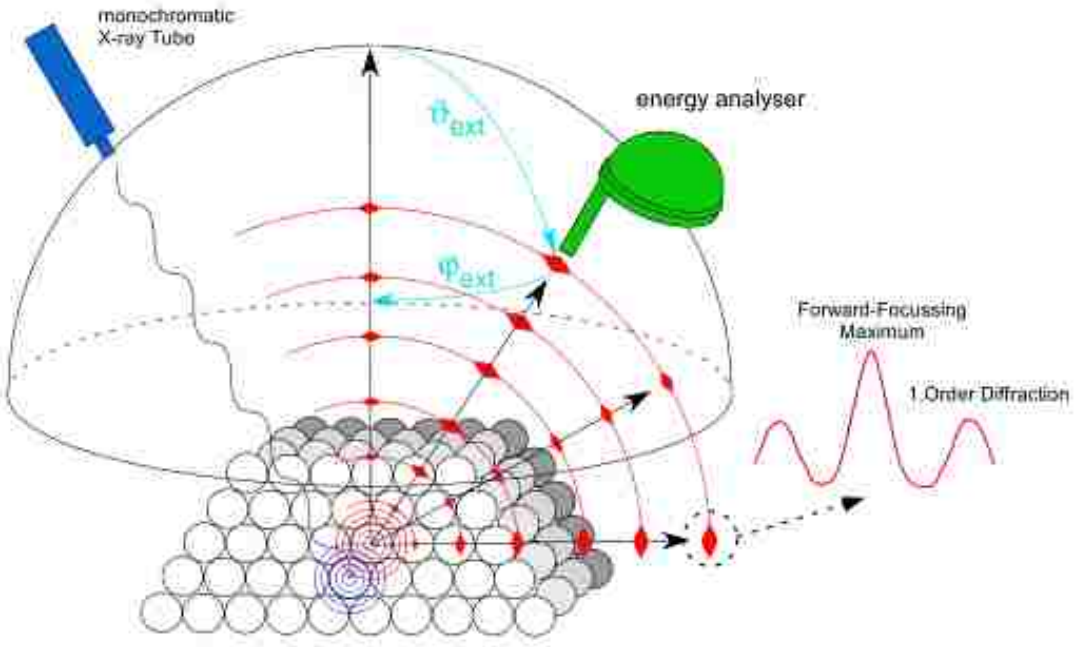

Figure 3.5. Illustration of the X-ray Photoelectron Diffraction (XPD) method. The exited emitter atom (Blue) sends a spherical wave, which interferes with the scattered wave (red), and the interference pattern shows angle dependence intensity. This intensity is recorded by an electron energy analyzer. On the right side, the intensity distribution shows the forward scattering and diffraction 1st order.

By varying the X ray analyzer detection angle both in the polar and zimuthal angles, we are now expecting the core level peak intensity to modulate. In our experiment setup,

the easiest way for us to implement is to change the polar angle, as we are able to rotate the sample in a polar angle, keeping the sample in vacuum. As shown in Figure 3.6 with arrows pointing at different directions, the possible forward scattering peaks are supposed to observe at polar angles 0°, 22°, 25°, 45°, 48°, 60°, and 63° etc.

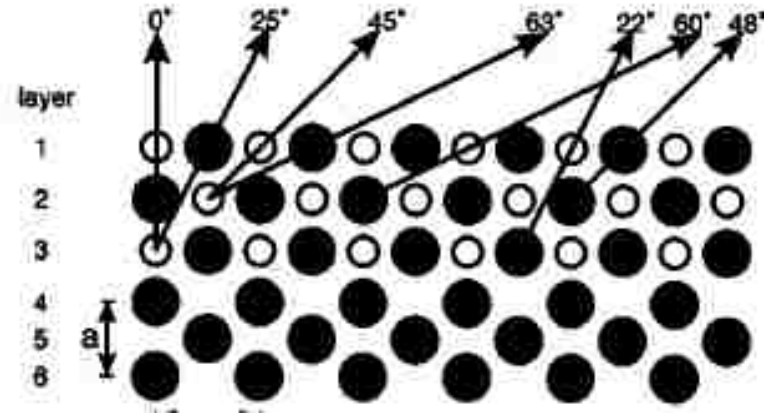

Figure 3.6. A sample structure model for NaCl, showing a vertical cuts through the crystal along the [011] and the [bcc] two inequivalent nearest neighbor planes azimuthal directions. The arrows indicate the dominant forward scattering directions of photoelectrons emitted from either Na or Cl atoms.

The intensity of the forward scattering peak is very difficult to quantify. In deed it is based on the first Born Approximation and proportional to square value of scattering amplitude. The intensity of forward scattering contribution below the surface has an exponential decay $e^{-d/\lambda\cos\theta}$. The higher emission angle, the bigger ratio of electrons from the surface is. Although this is an oversimplification of the physics, there is in general a monotonic decrease in emission depth with decreasing takeoff angle that can be used both qualitatively and quantitatively to study the depth distributions of species near surfaces. As for an angular scan, the total intensity plotted will include the contributions from the first and subsequent layers of the solids. Even though precisely simulating the

angular distribution can only be achieved through sophisticated multiple scattering scenario, but we can qualitatively tell that the angle scan intensity is dominant by the near surface layers because of the defocusing effect of the multiple forward scattering. Indeed, this can still be a qualitative tool for surface structure analysis, though the scattering peak intensity will be underestimated. Shown in Figure 3.6 which is a typical structure NaCl, we can draw a few forward scattering directions by the arrows. The atomic number of Na and Cl are 11 and 17 respectively. We can naturally tell the forward scattering peak intensities for angles 22° and 25°, which have same travelling distance of photoelectrons to the emitter, are not equivalent. They should have a ratio $11^2/17^2$=0.418. Considering the angles 25° and 48°, though the emitter are both Na atoms which means the atomic number is same for emitter scattering, the travelling distance for Cl and Na electrons are different. Therefore, the intensity ratio for the two peaks should be $\frac{e^{-\lambda_{Cl}/a\cos 25}}{e^{-\lambda_{Na}/0.5a\cos 48}}$. Here the λ represent the IMFP for specific core levels. Therefore we can clearly estimate the forward scattering peak position and peak intensity ratio. Again, the capability from the above assumption is to only give us the intensity ratio and the actual intensity values.

Removing the photoelectron forward scattering effect (intensity ratio of diffraction effect) in the ARXPS intensity ratio, we can have the pure information from the structure stacking sequence starting with the first surface layer, which provide a precise determination of the surface chemical composition and structure.

3.3 Chemical composition study of Sr_2RuO_4 (001) surface using ARXPS methodology

Here we present the study for single crystal Sr_2RuO_4 (001) to test the effectiveness of our methodology using ARXPS considering forward scattering effect. In 1994, Maeno,

Hashimoto et al. reported the discovery of superconductivity with T_c= 1K in Sr_2RuO_4 [98]. Since that time, Sr_2RuO_4 has gained considerable attention and numerous papers have been published on Sr_2RuO_4. It is an unconventional spin-triplet superconductor with intriguing superconducting properties [104,99]. These are discussed in two excellent review articles, a very recent and comprehensive paper in April 2003 by Mackenzie and Maeno [100] and a publication in January 2001 by Maeno, Rice and Sigrist [101]. The study of ruthenates is a active subject of research and so far there are still many open questions. For example, the properties of $Sr_{n+1}Ru_nO_{3n+1}$ exhibit strong dependence on the number of RuO_6 octahedral layers in crystal structure, reflecting the effect of dimensionality in the system [102]. Ca doped $Ca_{2-x}Sr_xRuO_4$ [103] has various interesting properties related with the correlation effect among Ru 4d electrons though 4d orbitals are fairly delocalized. And also mall amount of Ca doping can also kill the triplet superconductivity easily. It has also been reported that a lattice distortion takes place at the surface [104] giving FSs different from the bulk.

A controlled way to disturb the coupled system without changing the stoichiometry is to break the symmetry by creating a surface. Sr_2RuO_4 has proven results to show the surface termination layer is SrO. We used Sr_2RuO_4 as a test sample for developing theory of ARXPS with photoelectron diffraction. The experiment results successfully confirm the surface composition and the surface structure. The single crystals of Sr_2RuO_4 were grown by the floating zone technique [105]. The x-ray diffraction on these crystals did not reveal any impurity phase. The samples were cleaved at room temperature in ultrahigh vacuum conditions to form a (001) surface and were immediately transferred

into the μ-metal-shielded analysis chamber equipped with LEED and XPS. The crystals were cleaved between two SrO layers without breaking RuO_6 octahedra. There are two possible cleavage planes.

Figure 3.7 shows a typical LEED pattern taken from the cleaved surface of Sr_2RuO_4 at room temperature, showing excellent diffraction patterns. The surface layer shows a lattice distortion characterized by rigid RuO_6 octahedra rotation, which is not presented in the bulk, thus reflecting the surface reconstruction $\sqrt{2}*\sqrt{2}$ have been observed. The samples do not have obvious degradation during experiments.

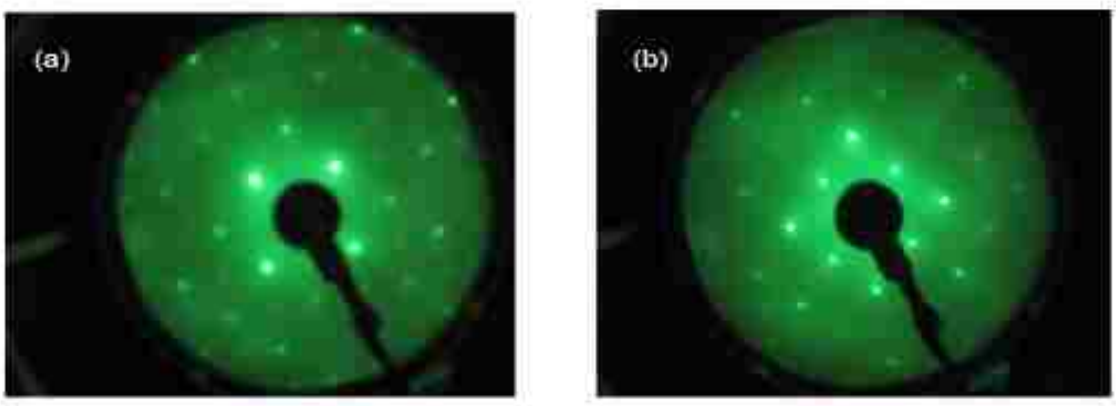

Figure 3.7. A typical LEED pattern from a freshly cleaved Sr_2RuO_4 surface taken at room temperature with electron-beam energy of (a) 200 eV and (b) 250 eV.

We also used Ion scattering spectroscopy (ISS) to inspect the surface. To simply describe ISS, the mechanism is as follows. A beam of positive ions derived from He or Ne is directed at the surface. Some of these ions are reflected with the loss of energy appropriate to the simple binary elastic collision of the ion beam with a particular surface atom. At any fixed scattering angle, defined by the angle between the ion source and the analyzer, the energy loss of the ion is dependent only on the mass of the surface atom

causing the scattering. The technique is uniquely sensitive to the outermost layer of the surface and ISS spectrum can provide the surface content information. Figure 3.8 is the structural model of the bulk Sr_2RuO_4 and large scale STM image (4 x 4 μm) showing the origin of the step height. The cleavage plane for this layer compound is SrO shown in Figure 3.8(c).

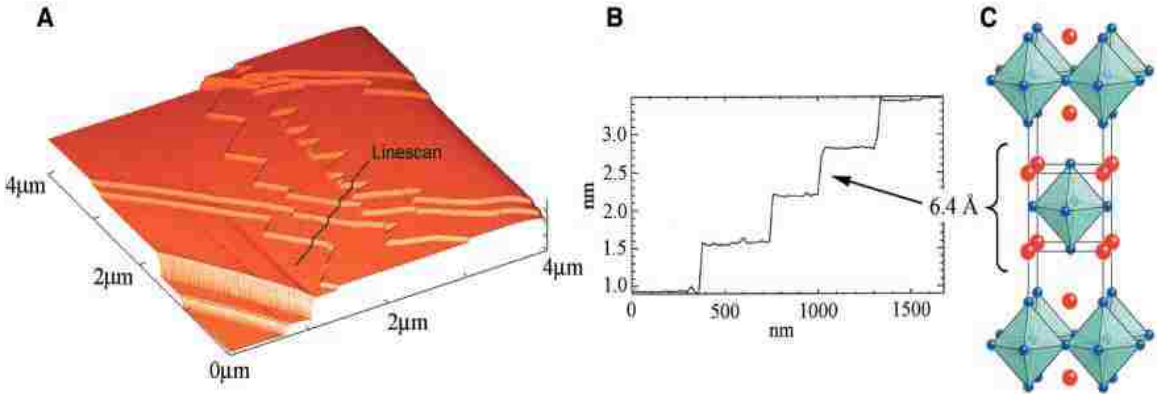

Figure 3.8. (a) Large scale of STM image showing clear terrace (b) Multiple of half unit cells shown as step height (c) Ball model structure of Sr_2RuO_4. (Reference 104)

We have performed the XPS study on Sr_2RuO_4. Figure 3.9 displays the character spectra with change of emission angles. The top to bottom curves are 0 to 81° with step of 3°. With the high intensity and resolution of X ray core level spectra, we can clearly cut the background with the same type as Shirley background. Both Sr 3d and O 1s spectra has signature of multiple components, which vary with the emission angles. It is not difficult to understand that they are actually surface and bulk component. The surface component for O 1s is sitting at around 1.5 eV higher binding energy side. As we can see Sr 3p spectra is entangled with Ru 3d peaks, therefore we use Sr 3d as the characteristic peak for our model analysis as the background subtraction is much simpler.

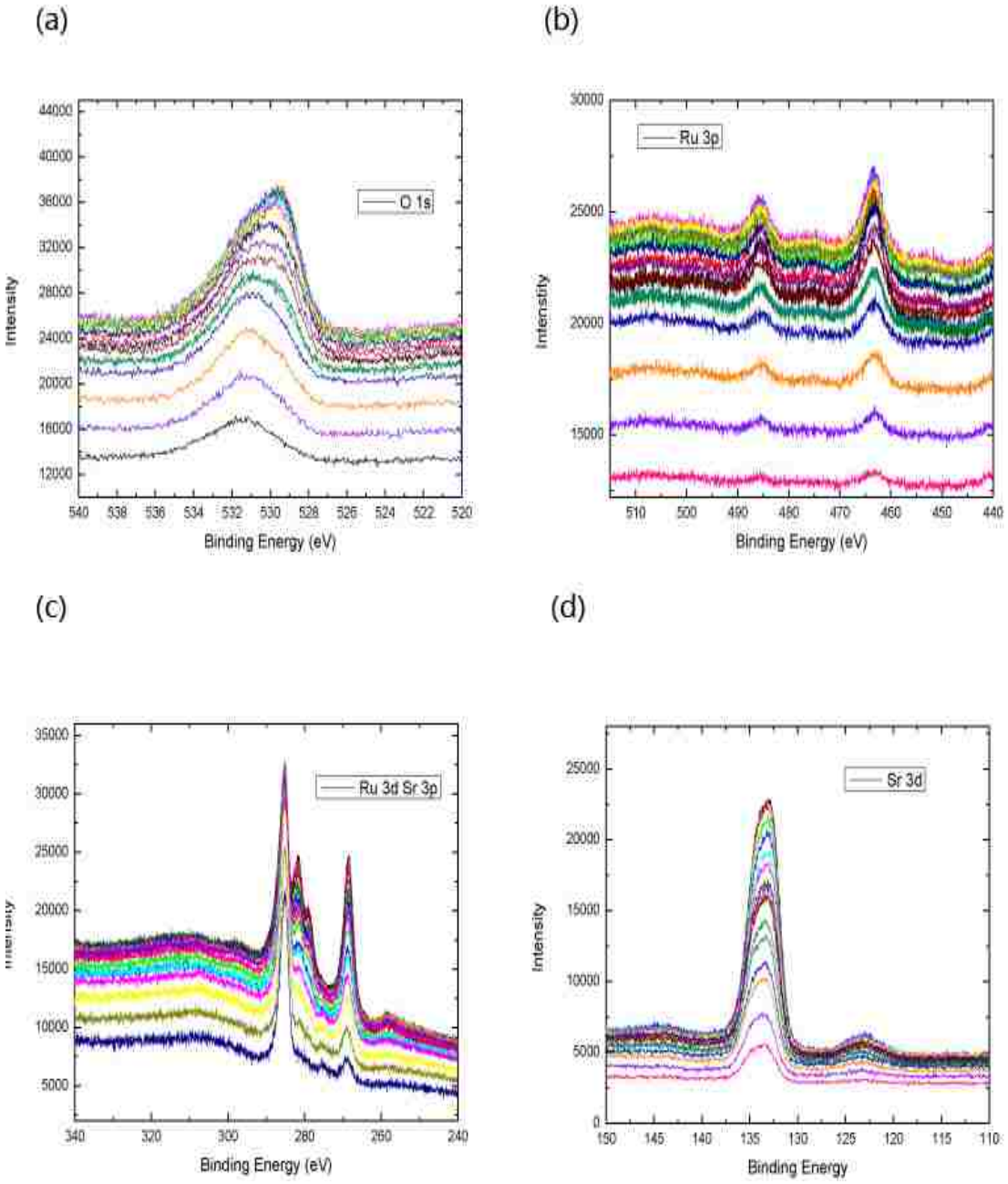

Figure 3.9. Spectra of core levels O 1s, Ru 3p, Sr 3d and Ru 3d/Sr 3p displayed from top panel to the bottom. The intensities of four spectra drop with the increase of emission angles. The curve colors ranging from black to navy blue represents 18 curves with emission angle step 3°.

In Figure 3.10, we display the reverse "branching ratio'' for Sr 3d spectra at the emission angle of 80°. The yellow and violet lines represent the surface components. To

fit the Sr 3d curve, we have set the peak positions difference between Sr $3d_{5/2}$ and Sr $3d_{3/2}$ to be same for both surface and bulk components. Also the line width and intensity ratio for spin orbital splitting curve must be similar as well. It is clear to us that the branching ratio remains the same. The reverse behavior of two peak heights is actually due to the substantial increase of the surface components.

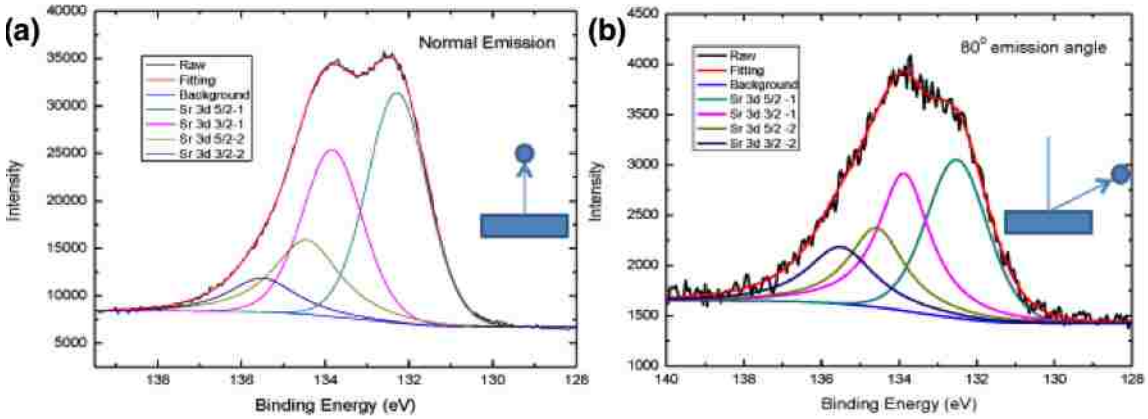

Figure 3.10. (a) Sr 3d core level spectra comparison at normal emission and (b) 80° emission angle. Sr $3d_{3/2}$ and Sr $3d_{5/2}$ surface and bulk components are marked by green, pink, yellow and violet solid curves respectively.

We have also fit in a similar way for the O 1s peaks. Because of the broad line width, we have to fit the O 1s spectra with 4 components that are naturally explained as two different oxygen chemical bonding environments and surface can be seen in the 214 structures. The FWHM of four peaks are fit close to 2.5 eV. As seen in Figure 3.11, both the intensities under violet and blue curves increase with the emission angle, indicating the character of surface sensitivity. Therefore, the pink and violet curves represent the bulk components whose intensities drop with the increase of the emission angle. We assign the four components to be O1 (pink), O2 (green), O1 surface (blue) and O2 surface (violet). The multiple components are coming from the various chemical environments for oxygen atoms. O1 and O2 peaks are coming from SrO and RuO_2 layers.

Interestingly, the peak positions of bulk components of O2 and O2 do not agree with that of surface components. In the bulk, the energy difference is around 1 eV; for the surface, the difference induced by the chemical bonding is 3 eV. From the fact of SrO termination, we believe the oxygen at this layer is affected substantially than the surface oxygen in subsequent RuO_2 layer due to the broken symmetry.

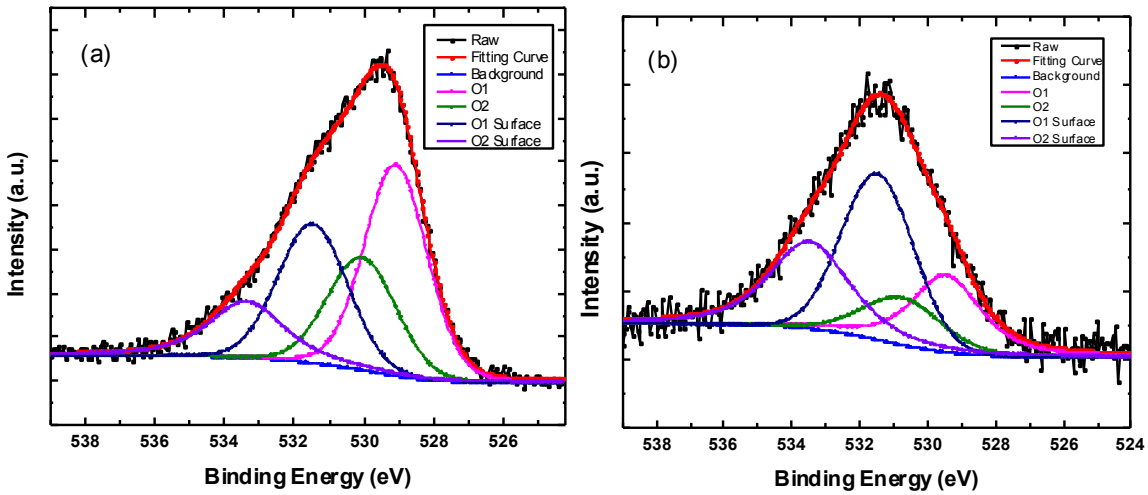

Figure 3.11. a) O 1s spectra comparison at normal emission and (b) 80° emission angle. O 1s spectra are fitted with four components O1, O2 and their corresponding surface components marked by pink, green, blue and violet curves respectively. The raw data and fitting curve are marked as continuous black and red lines.

Since we already know that the surface is mainly SrO layer, it is not difficult to understand why the surface component at higher binding energy positions increase as the emission angle. This is a good example reaffirming the surface composition using ARXPS. To check the stoichiometry carefully, we will need quantitative analysis for the intensity of core level spectra. Let us consider the relative intensities of Sr 3p and Ru 3p. The actual area used for all the peaks are carefully calculated using appropriate background subtraction. Figure 3.12 shows plots of Sr 3d/Ru 3p(Sr/Ru) in black as a function of the emission angle. The XPS spectra for all of the curves are taken at step 5°.

There is a strong angular dependence of Sr/Ru ratio and the increase of Sr/Ru ratio is also consistent with the fact of SrO termination layer. Apparently, the modulation of the intensity ratio comes from the photoelectron forwarding scattering effects.

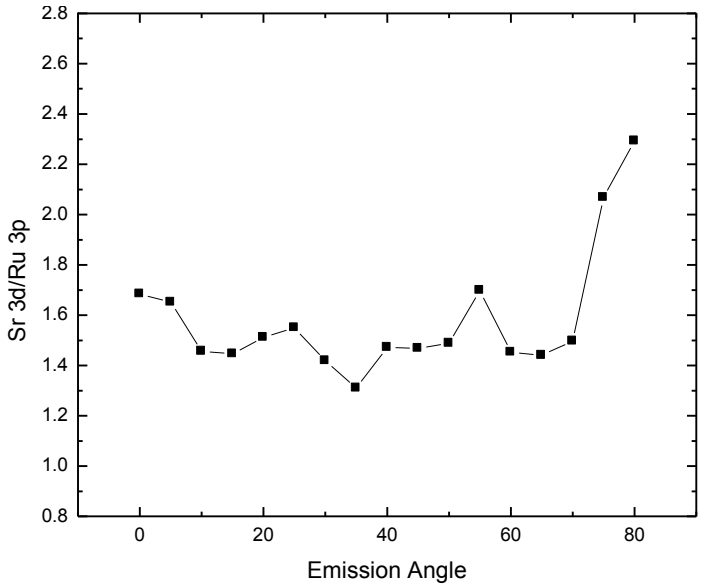

Figure 3.12. Experimental angular dependence of the core-level intensity ratio of Sr 3d/Ru 3p measured at room temperature.

Now we shall use the following equation to calculate the intensity ratio theoretically

$$\frac{I_A(\theta)}{I_B(\theta)} = \frac{\sum_j n_A e^{-jd/\lambda_A(E)Cos(\theta)}}{\sum_j n_B e^{-jd/\lambda_B(E)Cos(\theta)}} \cdot \frac{\sigma_A}{\sigma_B} \tag{3.10}$$

where n is the atomic fraction of the element at j^{th}-layer, d is the interlayer spacing. The cross section were taken from Spec lab. For Sr 3d and Ru 3p, the cross sections for Al source are 5.05027 and 3.439 respectively. As SRO214 system is metallic, thus we put the gap energy as 0 eV. Inelastic mean free path can be calculated according to equation 3.2. The other necessary data to calculate IMFP are listed in Table 3.1.

Table 3.1 Parameters to calculate the IMFP of characteristic curves for Sr_2RuO_4.

E_p	22.79	Eg	0 eV
C	1.4001134	ρ	5.92 g/cm3
D	40.37402	N_v	36
β	0.0238512	M	340.3117 g/mol
γ	0.078302	U	0.626249

Table 3.2 List of cross section and IMFP for Sr 3p, Sr 3d, Ru 3p and O 1s core levels.

Element	Z	Electron Shell	Shell	σ(Al K_a)	E_k(eV)	E_k(eV	λ(E) (Å)
Sr	38	$5s^2$	3p	4.331	1218.1 (3p3/2)	1209.9 (3p1/2)	21.48
			3d	5.05027	1352.9 (3d5/2)	1351.0 (3d3/2)	25.38
Ru	44	$4d^7\ 5s^1$	3p	3.439	1023.6(3 p 3/2)	1001.1 (3p ½)	14.96
O	8	$2s^22p^4$	1s	2.92991	955.7	531.1	18.92

The structure of SRO is well defined. With the SrO-RuO_2 stacking sequence, we simulate the theoretical curve shown in Figure 3.13. Basically there is little change of intensity ratio at wide range of emission angles until 70°. As the emission angle further increases, especially at the angle as high as 80°, the estimated thickness that allow photoelectrons to travel through without going through inelastic collisions with other atoms can be only as thin as 0.1 nm. This clearly illustrates the picture of SrO termination. The Sr_2RuO_4 has lattice constants a=0.387 nm and c=1.274 nm. Shown in Figure 3.14, which is the ball model of the crystal structure (perspective view). A few possible forward scattering peaks for Sr atoms are marked by lines (1), (2) and (3). The three angles with respect to the normal direction can be calculated easily.

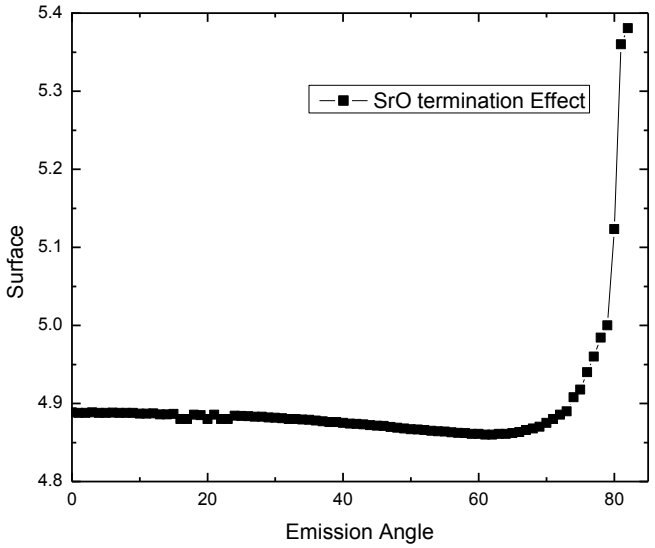

Figure 3.13. Theoretical angular dependence of Sr 3p/Ru 3p intensity considering SrO termination and SrO, RuO_2 stacking sequence.

For peak 1, the scattering angle can be derived from $\arctan(\frac{0.5a}{0.5c-0.5a}) \approx 23.55^{o}$.

Similarly for peak 2 and peak 3, they can be calculated through actan1 and arctan3 respectively; so the corresponding peak angles are 45° (arctan1) and 71° (arctan3). For Ru 3p characteristic photoelectrons with kinetic energy 1001.1 eV can be possibly scattered at angles 41.11° and 63.43°. Of course both Sr 3d and Ru 3p core level spectra will have forward scattering peaks at normal emission scattered by oxygen atoms at different layers. There is multiple scattering effects need to be considered in this case. However we found the multiple scattering only contributes to the magnitude of the peak, not the peak shape and intensity ratio of two spectra. Therefore we have chosen to use single scattering simulation to get the intensity ratio value. To understand the scattering directions, we shall use the ball model to illustrate the scattering process, especially the elastic forward scattering.

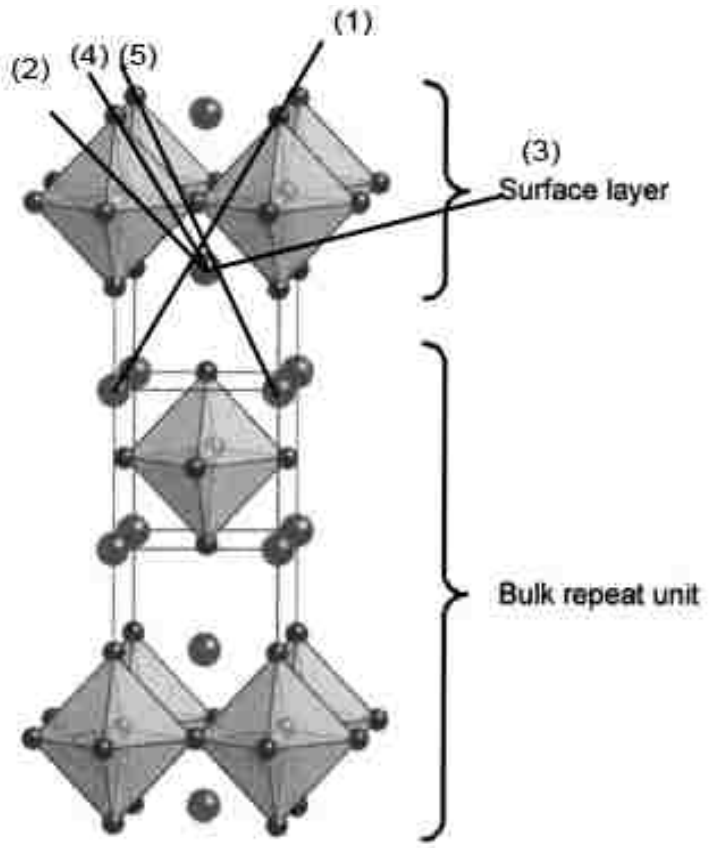

Figure 3.14. Ball model of the crystal structure (perspective view). The big ball represents the Sr atoms and the small ball oxygen. Ruthenium atoms are located in the center of the octahedral. Bulk-repeat unit is and surface layer are indicated. Lines marked by number (1), (2) and (3) indicate the forward scattering directions for Sr atoms.

Take one scattering peak as an example, Sr 3d forward scattered peaks at 45° is scattered by Sr atom too with atomic number 38. The peak at angel 63.43° has the same scatter Sr, so the intensity contributions from these two angles will be only proportional to $\frac{e^{-\lambda_{Sr\,3d}/a\cos 45}}{e^{-\lambda_{Sr\,3d}/a\cos 63.43}}$, here a is the lattice constant 0.387 nm. If we define the forward scattered peak at zero as A, we can get the other few peaks illustrated as $A * F_n(\theta_n)$. The intensity ratio for Sr 3d and Ru 3p as $\frac{I_{Sr\,3d}}{I_{Ru\,3p}} = \frac{A(1+F_{A1}(\theta_1)+.....+F_{An}(\theta_n)}{B(1+F_{B1}(\theta_1)+.....+F_{Bn}(\theta_n)}$, here A, B

ratios can also be calculated knowing the atomic number and the scattering routes. By adding all possible scattering peaks together whose Gaussian profile has different peak heights. Figure 3.15 shows the theoretical curve marked in black dot for the Sr 3d and Ru 3p intensity ratio (Sr/Ru).

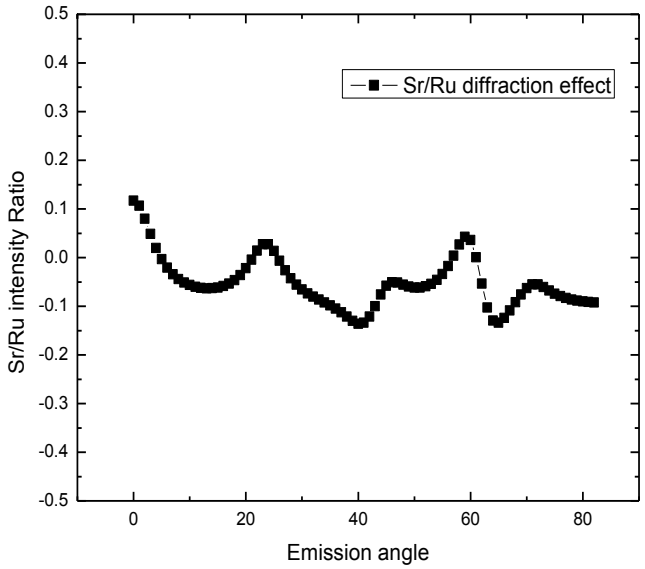

Figure 3.15. Theoretical intensity ratio of Sr 3d to Ru 3p cpre levels as a function of angle due to the zero-order XPD effect.

By adding the simple structure effect with surface termination SrO and the forward scattering effect, we can simulate the intensity ratio and compare with experimental result and see how good our methodology is. See Figure 3.16, with two curves plotted as red scattered curve and black line curve. Except the regions at the low emission angle range 0°-10° and high emission angle range 70°-80°, there are slight difference between theoretical and experimental results. Overall, the theoretical model fits very well with the experimental results. The dips and peaks' positions coincide with the forward scattering peak positions. The errors not only come from the data collection, background

subtraction and other instrument errors, but also the intrinsic differences as the methodology we developed have a lot of assumptions, such as first born approximation, no multiple scattering, peak Gaussian broadening, perfect surface stoichiometry etc.

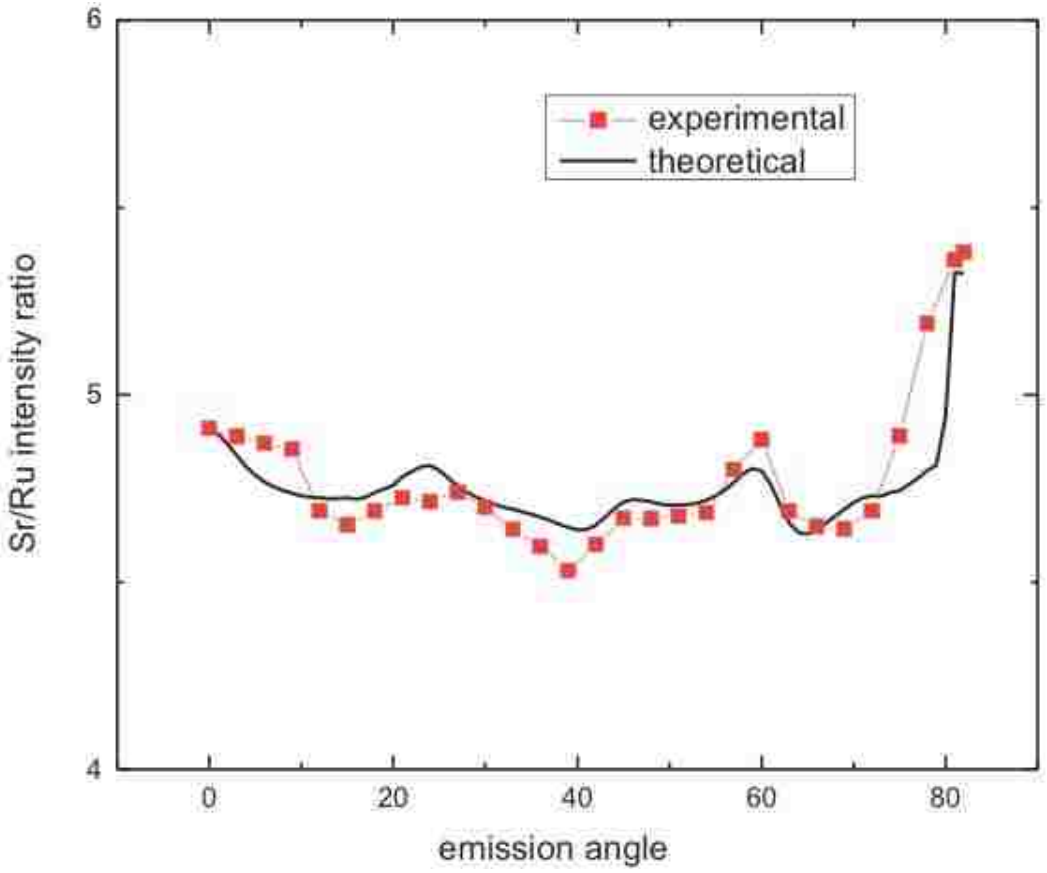

Figure 3.16. Theoretical (solid black curve) and experimental (red dots) angular dependence of Sr 3p /Ru 3p intensity ratio measured at room temperature.

Using the angle-dependence of Sr 3d/ Ru 3p core level intensity ratio, our method clearly confirms that the termination layer of the surface is SrO-layer as the high emission angle trend matches. The diffraction pattern matches very well with the theoretical calculation of forward scattering peaks. We have successfully shown the ARXPS methodology is a very promising tool for the surface and interface chemical composition analysis.

CHAPTER 4. SURFACE ANALYSIS OF SINGLE CRYSTAL $SrTiO_3$ (100)

4.1 Introduction and motivation

$SrTiO_3$ is of cubic perovskite structure and an insulator with a band gap of 3.2 eV. Self-doping with oxygen vacancies or element doping by Nb will result in n-type semiconductor. The major purpose of my study $SrTiO_3$ is not only because it is frequently used as a substrate for thin film growth [106], but also because perovskite type oxide $SrTiO_3$ attracts considerable attention as models of catalysis systems [107,108]. $SrTiO_3$ (001), as an important substrate for our PLD growth for thin films, has controllable termination layer with either TiO_2 or SrO. The atomically flat TiO_2 terminated surface can be obtained by HF buffer solution etching and *in-situ* annealing [109]; while SrO termination surface (SrO (001)) is obtained by high temperature annealing [110] or depositing a SrO layer on TiO_2 (001) surface [111]. Various surface reconstructions (1x2, 2x2, 4x2, C(2x2), C(4x2), c(6x2), c(√5x√5), etc.) have been reported [112,113,114,115,116,117]. The surface reconstruction will affect growth and properties of both interface and epitaxial film [118,119].

The $SrTiO_3$ interfacial layer plays an important role in interface properties. For the $LaAlO_3/SrTiO_3$ interface where both $LaAlO_3$ and $SrTiO_3$ are wide band gap insulators, unexpected formation of a quasi-two dimensional high-mobility electron gas emerges [120]. This interface can be superconductive at low temperature [121]. Superconductivity behavior between was also observed at $LaTiO_3/SrTiO_3$ interface [122]. In the case of $LaAlO_3/SrTiO_3$ interface, if the termination layer is SrO, the interface maintains insulating, but an only TiO_2 termination layer provides possibility of creating free electron gas [15].

A theoretic calculation suggests that the termination layer of $SrTiO_3$ can vary the interface electronic and magnetic properties of $SrTiO_3/La_{2/3}Sr_{1/3}MnO_3$ interface [123]. The surface defects, polarity, reconstruction, termination layer could strongly control the properties of the film grown on STO. Many models have been proposed for surface structure, but there is no firm conclusion yet. The most fundamental question to ask is what is the termination layer. Recent reports seem to be inconsistent. Liang, *et al.* have shown that annealing in UHV above 1000°C will give rise to SrO rich surface, because sublimation rate of Ti is higher than that of Sr [124,125]. However, Szot *et al.* report that UHV annealing results in TiO_x rich surface [126]. Here we present the study of $SiTiO_3$ which was HF treated surface using STM, LEED, XPS and ARXPS to characterize the surface chemistry and structure.

4.2 Surface morphology of specially treated single crystal surface of $SrTiO_3$

The 0.1 wt% (001) Nb doped $SrTiO_3$ single crystal substrates were procured from CrysTec Co. The sample size is 5mm*5mm*0.5mm which is big enough for XPS experiment. One side of the surface is polished. To perform wet-etching, the sample was first sonicated in (1) Acetone for 5 min; (2) Ethanol for 5 min (3) Milli water for 5min; (4) then put in Buffer HF solution (From Alfa Co.) for 30s. After wet-etching, we used ultrapure N_2 gas to blow it to dry, and then mounted it onto a home-made sample holder, which has oxygen compatible resistance heater, and load it into UHV system (base pressure: 10^{-10} Torr).

The surface morphology under different annealing condition was imaged with STM. As shown in Figure 4.1, the surface of the as-etched sample (sample-1 as shown Figure 4.1) has relative narrow terraces of about 40 nm wide and the step edges are not very

straight. With annealing at 500°C for 1 hour (sample-2), the step edge still looks a little rough. The step edge will be straightened out with higher annealing temperature as the samples annealed at 800°C (sample-3) and 900°C (sample-4) as examples. The large-scale STM images of sample-1 and sample-4 are displayed in Figure 4.2. The height profile of sample-1 surface shows that step height is ~ 0.39 nm, suggesting a single termination surface of the as-etched sample. After annealing at 10^{-4} Torr Ozone at 900°C for 1 h, the surface morphology changes, but the step height is still 0.39 nm, indicating that the surface still has a single termination. Generally, an atomically flat substrate will favor 2D growth and is good for the quality of a thin film. With respect to an ultrathin film especially the case that the interface coupling cannot be ignored, a single termination and atomically flat surface is usually necessary. With HF buffer solution etching and high temperature annealing, we can obtain good substrate morphology for epitaxial growth.

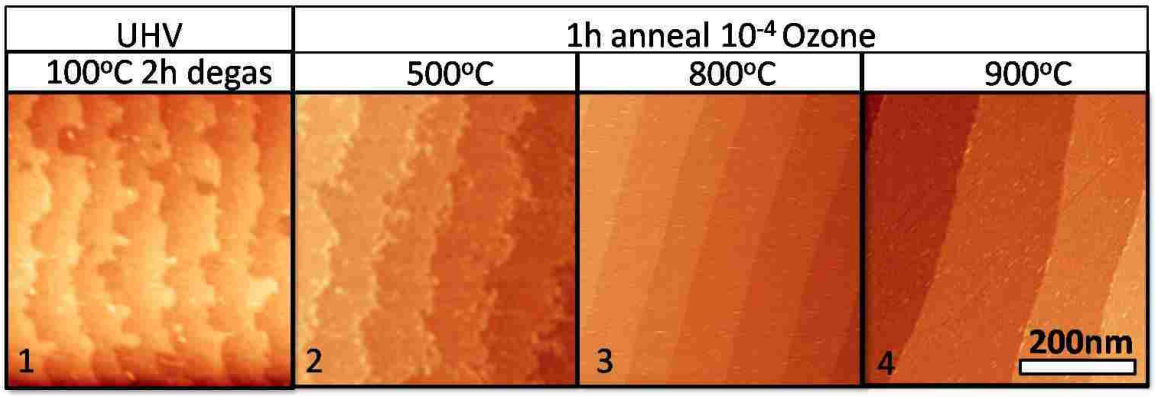

Figure 4.1. Surface morphology of $SrTiO_3$ (001) at different treatment conditions.

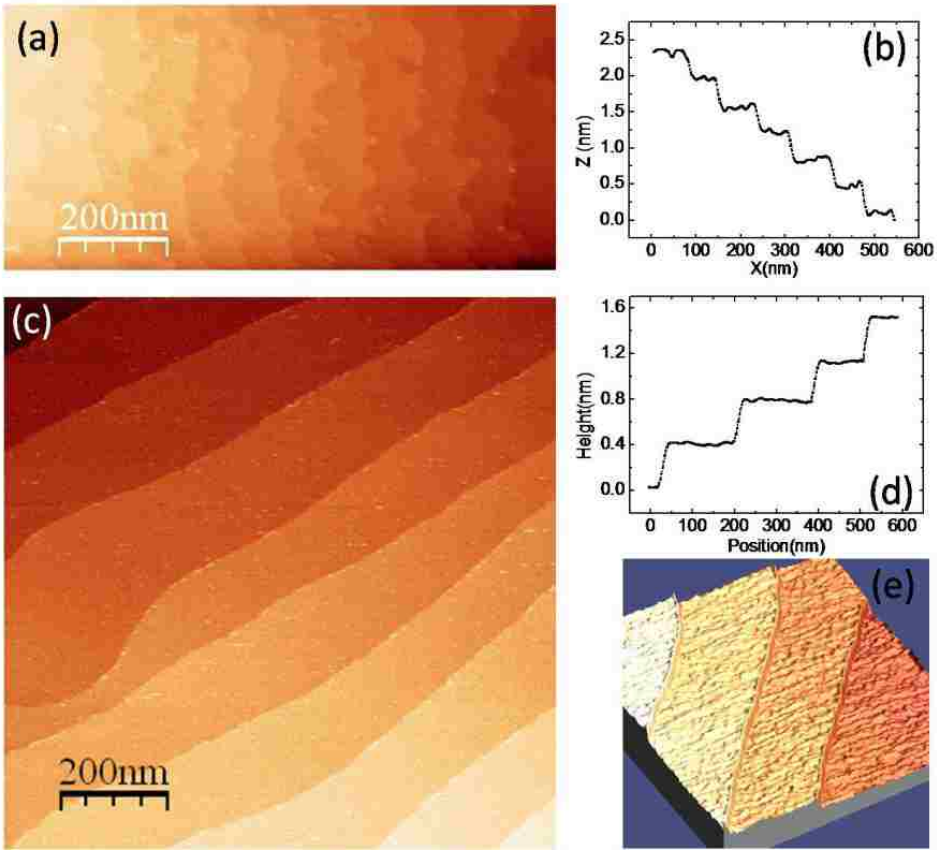

Figure 4.2. (a) STM image and (b) height profile of as-etching $SrTiO_3$ surface after degas at 100°C in UHV. (c) STM image and height profile of sample annealed at 900°C for 1 h at 10^{-4} Torr Ozone and (e) its 3D image.

4.3 ARXPS study of surface termination and composition of STO single crystal

The HF treatment leaves fluorine on the surface. ARXPS result for different treatment conditions is presented in Figure 4.3. A strong F1s peak can be observed in the spectrum of 100°C annealed sample. At higher emission angle, which only detect the first few surface layers of the solid, the F 1s intensity is enhanced. The Fluorine starts to disappear under 500°C and higher annealing temperature. The Carbon component can also removed by annealing at and above 650°C.

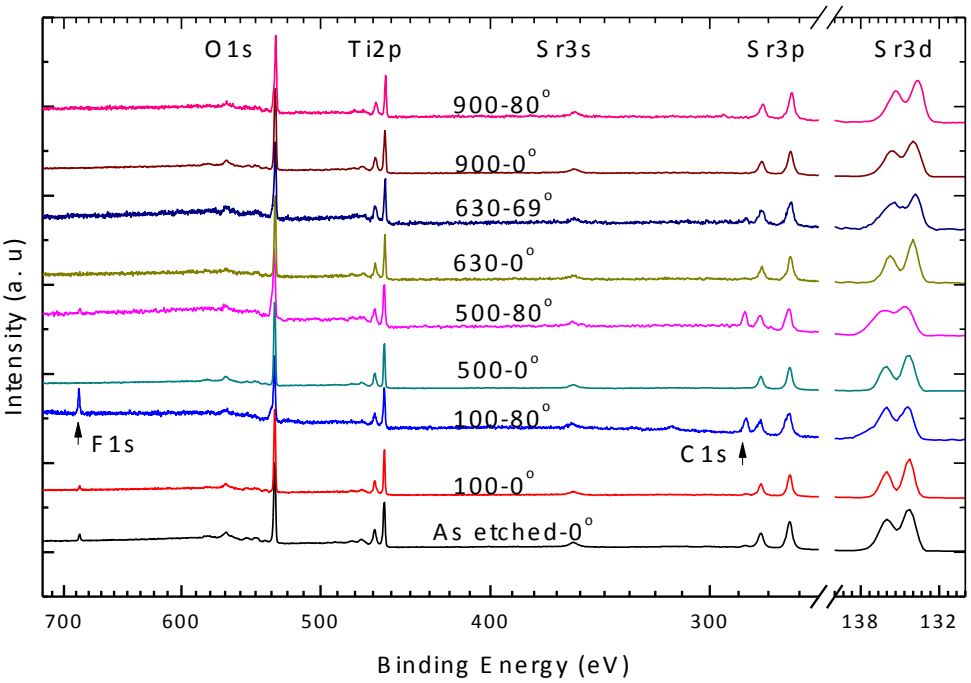

Figure 4.3. ARXPS data showing Fluorine component for degased sample especially at higher emission angle. Both F 1s and C 1s peaks are marked with black arrows.

The four spectra Sr 3d, Sr 3p, Ti 2p and O 1s are plotted in the Figure 4.4. The actual data collection was taken with angle step of 5°. Here we only present the raw data with 0°, 10°, 20°, 30°, 40°, 50°, 60°, 70° and 80°. Even at high emission angle, the resolution of the spectra is still good enough to allow us to do core level fitting and analysis. The change of intensity for different core levels are not monotonically as the forward scattering contributes the intensity substantially at a certain polar angle. One thing to notice is that the signature of Ti 2p spectra. The satellite peak binding energy is around 14 eV higher than the main peak. As we know the satellite is an indication of correlation, further study of the intensity ratio of satellite peak and main peak, the line width and FWHM is needed to investigate the difference between surface and bulk in terms of the correlation.

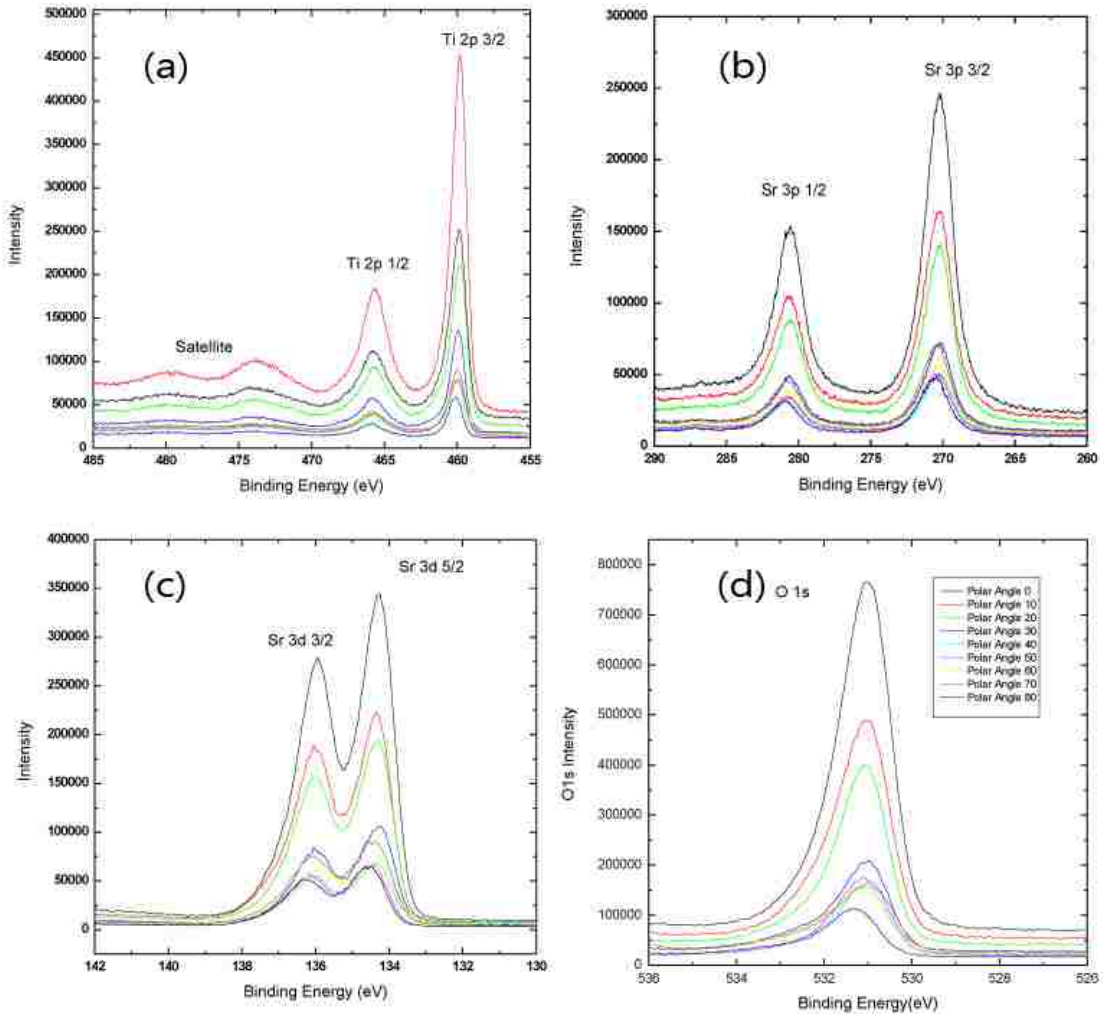

Figure 4.4. (a) Ti 2p (b) Sr 3p (c) Sr 3d (d) O 1s core level spectra.

Under the annealing temperature as high as 650°C, we can maintain the surface without reconstruction and keep the surface free from contamination. The LEED pattern with such annealing temperature proves that the surface is 1x1 with very little sign of reconstruction though we cannot rule out the possibility as many references indicate the reconstruction after annealing (Figure 4.4). This 1x1 surface of $SrTiO_3$ is not stable against high temperature and oxygen partial pressure.

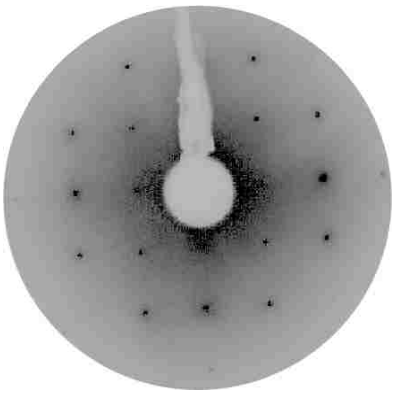

Figure 4.5. LEED pattern of unreconstructed p(1x1) surface with Oxygen vacancies taken at beam energy E=162 eV.

From XPS spectra O 1s, we can clearly see the oxygen surface component dramaticlly increase at high emission angle. We pick up a surface etched and annealled at 500°C. As shown in Figure 4.6, the left panel plots the two curves with normal emission in red and 80° emission angle in black (Figure 4.6a). A bump at higher binding energy for high emission angle curve can be seen. Then we fit the high emission angle spectra with green and pink curves as the surface and bulk part (Figure 4.6b). Due to the surface roughness, the linewidth for the surface component is very broad, indicating the lifetime of the surface electrons is shorter. The surface component is as high as 40% of the total photoelectron intensity at emission angle 80°, increasing from 13% detected at the normal emission. The line width for bulk and surface components remain relatively unchanged. We also noticed the surface components for STO crystals change with the oxygen partial pressure and annealing temperature. Further study of these dependence can reveal the surface composition, thus the possible relationship between the intriguing properties and the compositions change in proximity of surface. Here we choose an optimal annealling temperature 500°C as the surface is not reconstructed.

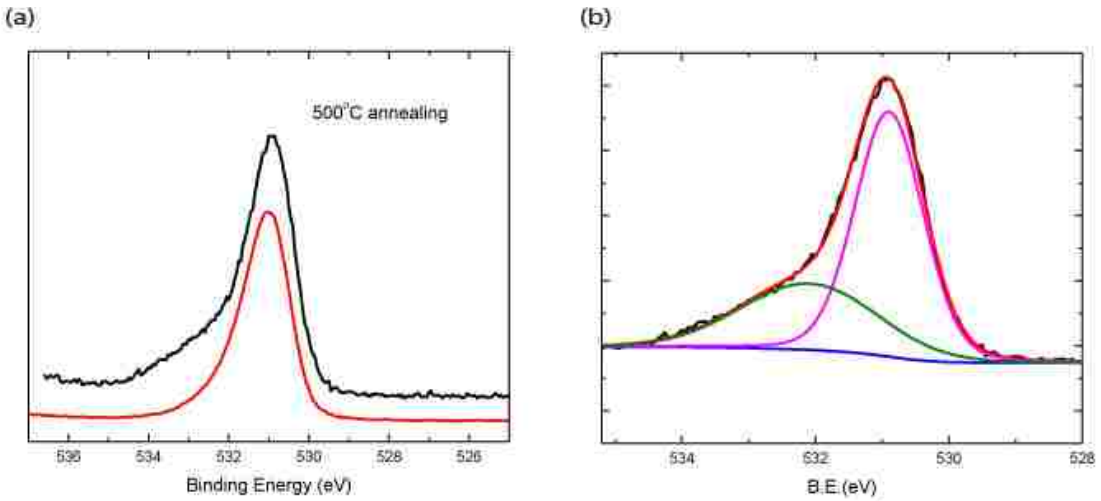

Figure 4.6. (a) the O 1s core level spectra taken at normal emission and 80° polar angles marked as red and black curves. (b) The 80° emission angle O 1s spectra is fit with two components in pink and green as the bulk and surface components.

Now we revisit a list of four spectra to be discussed in detail, Sr 3d, Sr 3p and Ti 2p and O 1s. The clear spin orbital splitting peaks indicate the good resolution of our system. The peak intensity is very high that it is very easy to determine the background. Ti 2p two higher binding bumps are satellite peaks for Ti $2p_{1/2}$ and Ti $2p_{3/2}$ respectively. The binding energies of the characteristic peaks are listed in table 4.1. Both the core level binding energies and peak shapes are similar to the previously reported results. In our experiments, the intensity has been simply calculated as the area after the Shirley background subtraction. The background subtraction has to be used using the consistent method, which is Shirley type, to ensure the intensity ratio is correct. As most peaks have surface components, we all use the main peaks to determine the peak positions. Table 4.1 lists the core levels binding energy, kinetic energy and cross sections references from Specs lab data base.

Table 4.1 Binding Energy and kinetic energy for core levels of $SrTiO_3$.

	E_b (eV)	E_k (eV)	CS
O 1s	531.1	955.6	2.84897
Ti 2p	457.1	1029.6	7.89713
Sr 3p	273.1	1213.6	5.70793
Sr 3d	135.3	1351.4	5.28808
F 1s	685.0	801.7	4.25845
C 1s	284.6	1202.1	0.99964

Take STO(001) etched surface as an example. By using equation 3.2 and the necessary parameters are shown in Table 3.2, we can simulate the Sr 3p/Ti 2p intensity ratio as in shown Figure 4.7. The Black and Red dotted lines represent TiO_2 and SrO termination layer separately. By plotting the actual intensity ratio for the STO treated sample, we will be able to determine the termination layer. In the same time, the detail surface structure can be analyzed through the modulation of intensity.

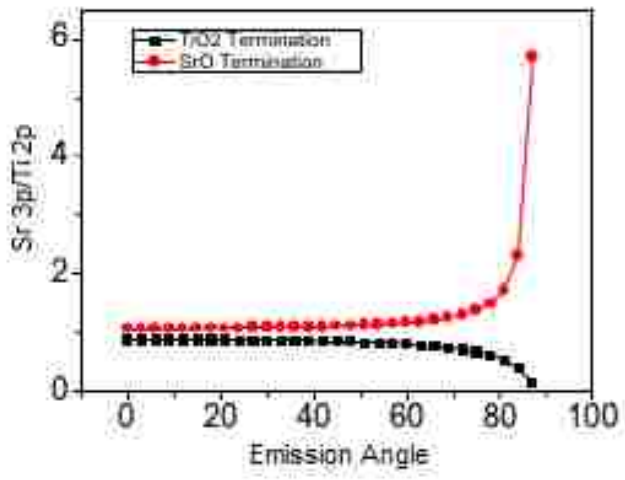

Figure 4.7. Theoretical angular dependence of Sr 3p/Ti 2p peak intensity ratio.

Table 4.2 List of cross sections, IMFP and materials gap energy, density, shell configuration and kinetic energies.

Element	Z	Electron Shell	Shell	σ(Al K_a)	E_k(eV)	λ(E) (Å)
Sr	38	$1s^2 2s^2 2p^6 3s^2 3p^6 3d^{10} 4s^2 4p^6 5s^2$	3p	4.331	1206.2	22.74
			3d	4.886	1351.0	24.68
Ti	22	$1s^2 2s^2 2p^6 3s^2 3p^6 3d^2 4s^2$	2p	5.04	1021.5	19.91
O	8	$1s^2 2s^2 2p^4$	1s	2.8	955.7	18.92

Eg	3.2eV
ρ	5.175g/cm^3
N_v	24
M	183.5
U	0.67684

E_p	23.7
C	1.35408
D	39.3217
β	0.0208214
γ	0.0839611

The next step is simulating the forward scattering peaks contributed to the intensity ratio. Though we are not clear with the termination, but since the structure of STO is same for both SrO and TiO_2 termination. The diffraction effect remains almost same. People have done X ray photoelectron diffraction (XPD) experiment on STO[127]. The XPD Sr 3d spectra taken from polar angles along [010] and [100] axes are shown in Figure 4.8. The normalized XPD pattern after the background subtraction for [010] and [100] are not identical due to the inhomogeneity of sample holder electrostatic potential. But the peak positions 1-7 are consistent along equivalent axes. The strongest two peaks which are marked 1 and 5 are <100> and <110> forward scatterings, respectively. One might expect the peak positions will be changed if the azimuthal angle φ is between 0° and 90°. Especially along the (010) direction, the peaks reflecting the forward scattering <111>, <211> and <311> will show up.

The previous study is allowing the researchers to further support the structure analysis through bulk probe techniques, but not providing us information about the surface concentration or termination. The difference in our XPD setup is that we use hemispherical energy analyzer with small acceptation angle. The flux of electron detected decreased in terms of the emission angles indicated in equation 3.1. In the process of rotating samples to create angles between emission and analyzer, the small position change of the sample make the flux perturb. The way to get rid of these perturbation effect is to calculate the intensity ratio at different polar angles. The ratio at high emission angle provides the good information about the surface. Qualitatively we can search for peak positions to discuss the corresponding bond angles.

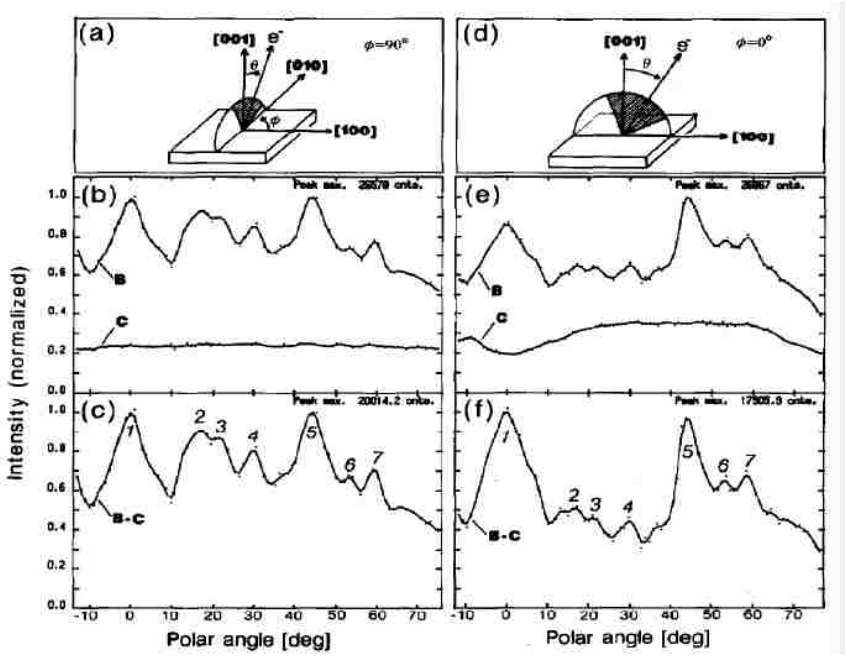

Figure 4.8. Sr 3d polar angle scan along [010] and [100] directions.

Figure 4.9 shows a theoretical simulation for the forward scattering effect of the intensity ratio of Sr 3p/Ti 2p. The diffraction peaks for Sr 3p are 45° and 71.56°; for Ti 2p spectra, the diffraction peaks are for polar angles 26.56°, 45° and 63.43°.

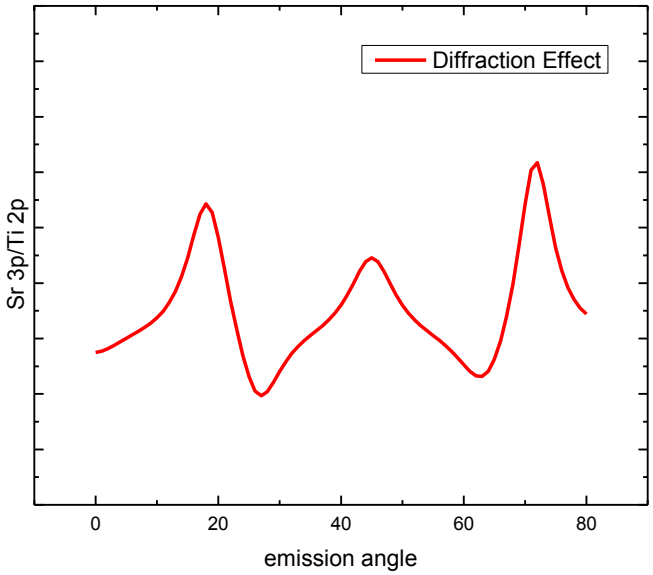

Figure 4.9. Theoretical simulation on the angular dependence of the forward scattering intensity ratio for Sr 3p/Ti 2p core levels for a truncated TiO_2-terminated surface of $SrTiO_3$ (100).

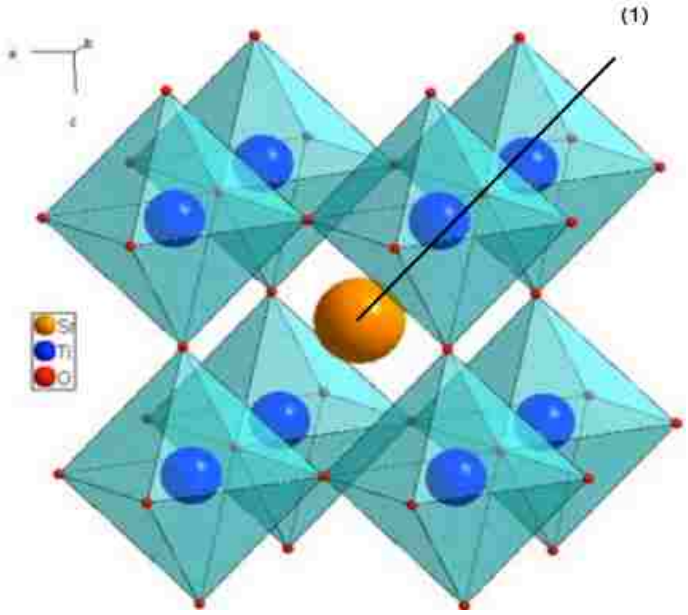

Figure 4.10. Crystal structure of single crystal $SrTiO_3$. Lines 1 points to forward scattering angle 45° of Sr atoms.

The overall theoretical curve for Sr 3p and Ti 2p is sum effect of forward scattering and right layer stacking. As shown in Figure 4.11, the black and red curves represent the

theoretical simulation results considering the SrO and TiO_2 termination respectively. The blue curve is the actual experiment data with proper background subtraction and intensity ratio calculation. We can clearly see the experimental data matches the trend with consideration of TiO_2 termination. The difference at the high emission angles is due to the oxygen vacancies that affect the IMFP for both Ti 2p and Sr 3p photoelectrons. Oxygen deficiency changes the material density and respective the number of electrons. For low all three curves have the same diffraction effects pattern which further show our theoretical models is quite successful and reasonable applying at the single crystals.

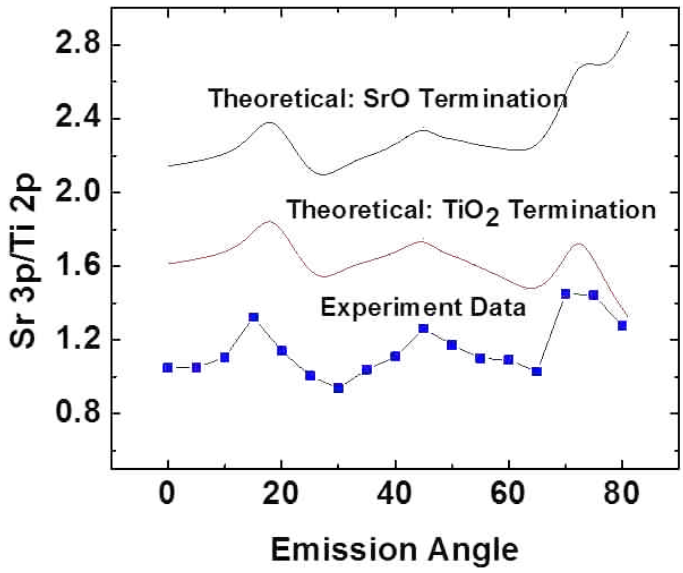

Figure 4.11. Angular dependence of Sr 3p/ Ti 2p intensity ratio (a) Theoretical curve with SrO termination, (b) experimental data by proper background subtraction, (c) theoretical curve with TiO_2 termination. Note all three curves have similar modulation patterns.

The slight inconsistencies at high emission angles between theoretical calculation of TiO_2 termination and experimental data are actually related to the oxygen deficiency. To further support this, we can measure the intensity ratio for O 1s/Ti 2p. Because the oxygen deficiency will decrease the oxygen peak intensity form the surface, we shall expect the angular dependence of O 1s/Ti 2p intensity ratio.

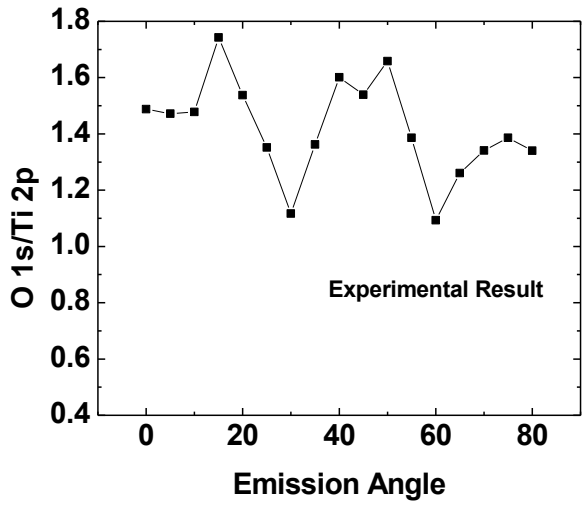

Figure 4.12. Experimental angular dependence of intensity ratio of O 1s and Ti 2p along (100) direction.

Apparently the intensity ratio of O 1s and Ti 2p has strong photoelectron diffraction effect. We firstly remove the diffraction effect which can be theoretically simulated to reveal the pure surface sensitivity effect. The angular dependence of diffraction effect is shown in Figure 4.13. There are strong forward scattering peaks at emission angles 18°, 45° and 71°.

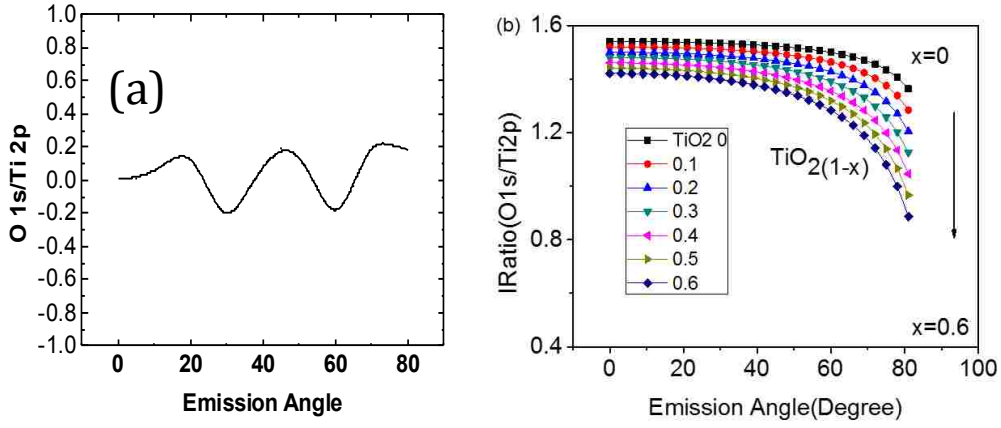

Figure 4.13. (a) Theoretically calculated diffraction effect on the O 1s/Ti 2p intensity ratio (b) Surface effects of angular dependence for different oxygen deficiency levels for O1s/Ti 2p intensity ratio.

As shown in Figure 4.13, the pure surface effect from the experimental data indicating there is oxygen deficiency on the surface the high emission angle result does not match the pure TiO_2 termination surface simulation. Only considering the surface Oxygen has around 30% deficiency, the angular dependence of O 1s/Ti 2p intensity ratio from pure surface effect shown in Figure 4.14 matches the best with the experimental result.

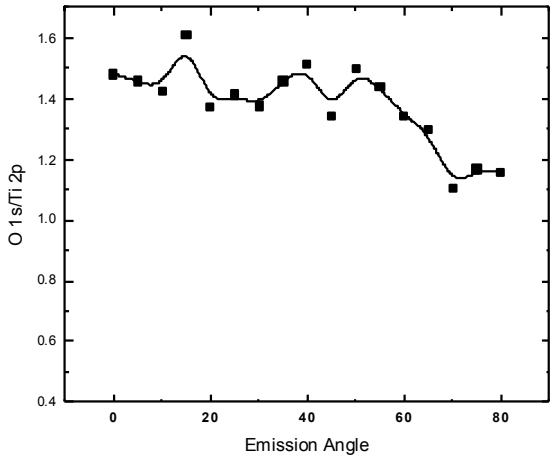

Figure 4.14. Theoretical O 1s/Ti 2p intensity ratio considering 30% oxygen deficiency at surface.

We also plot relative intensities from experimental results for Sr 3d/Sr 3p as a function of emission angle (Figure 4.15). There is little modulation or simply put, no angular dependence. It is not difficult to be understood, as the forward scattering peak and are independent with the core levels of same atoms.

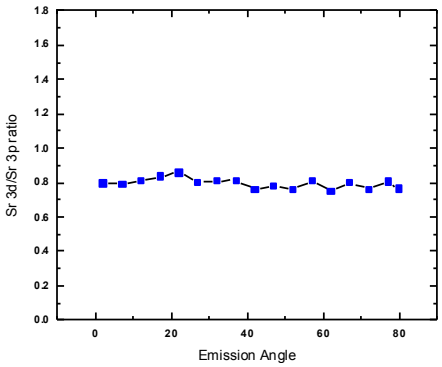

Figure 4.15. Experimental angular dependence of intensity ratio of Sr 3d/Sr 3p.

To conclude, forward scattering effect of the X-ray excited photoelectrons was observed for the $SrTiO_3$ (001) surface. The diffraction patterns reflect the crystal structure very well and no sign of reconstruction can be observed from the pattern. The surface is shown to have around 30% oxygen deficiencies with single termination of TiO_2.

CHAPTER 5. SURFACE STUDY OF $La_{0.65}Sr_{0.35}MnO_3$ THIN FILMS

5.1 Introduction and motivation

We have successfully applied the technique of ARXPS and X-ray photoelectron diffraction to study the surface structure of Sr_2RuO_4 single crystal and $SrTiO_3$ (100) surface. To further support the theory, a crystalline thin film will be another good testing material. The reduced dimensionality for a thin film will drive the metal oxides into a phase far from its counterpart of bulk. For example, a metallic phase switches into insulating phase with reduced dimensionality. It is not an exclusive phenomenon in artificial ultrathin film or quantum dot but initially observed in layer structure materials such as Ruddlesden-Popper series. We studied the surface chemical composition of crystalline films of LSMO by angle-resolved X-ray photoelectron spectroscopy (ARXPS). 33% doping LSMO is most itinerant ferromagnetic metal with curie temperature of ~370 K [128] among manganites. It has nominal 100% spin polarized electrons [129] and so is extensively used for spintronics [130,131,132]. However, electronic and magnetic properties disappear in the ultra thin films regarded as the dead layer [133,134,135,136,137,138]. The reason is still under debate. Difference growth conditions end up different dead layers. Our group has grown a couple of thin films with dead layer as few as 3 unit cells. We found the 6 (UC) LSMO thin film is particular interesting which could be a true critical thickness for the onset of metallic ground state. Under the optimal growth conditions which excludes the possibility of oxygen vacancies, the thin film with thickness below 6 unit cells are always insulating. Shown in Figure 5.1, we have grown several 6 UC LSMO thin films at various oxygen partial pressures. The resistivity exhibits slight trend of Metal Insulator Transition (MIT), but still defined as insulator.

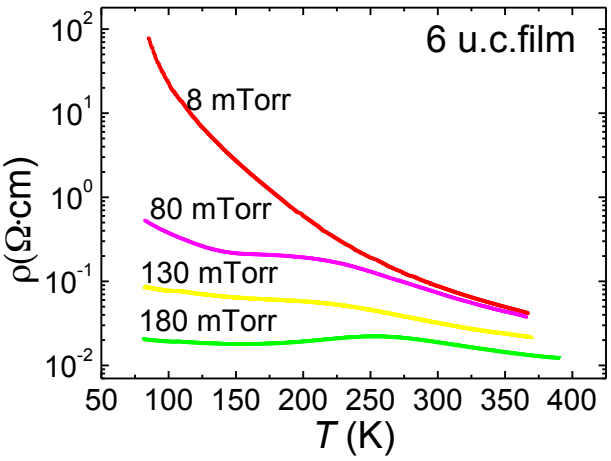

Figure 5.1. Resistivity measurements of LSMO 6 unit cells thin films at various oxygen partial pressures.

This particular surface of 6 UC thickness thin film is worth the study to dig out how the surface plays the role of the system ground states. As for this film, the surface composition was found to be quite different from that of the bulk with clear evidence of Sr segregation. Our photoelectron intensity modulation shows the surface has pure (La,Sr)O termination, which will be discussed later in detail.

5.2 Surface structure and morphology of 6 unit cells thin film

Atomic layer precise LSMO thin film was epitaxially deposited on STO using our Laser-MBE system from a stoichiometric LSMO target. A KrF excimer laser (λ = 248 nm) at a repetition rate of 3 Hz and a laser frequency of ~2.3 J/cm^2 was used. The spot size of the laser beam was ~ 0.021 cm^2. During the growth, an Ozone gas atmosphere was applied. To obtain layer-by-layer growth for all Ozone pressure ranging from 10^{-6} Torr to 180 mTorr, an optimized growth temperature window was explored and it was found to be ~ 680°C-720°C. The RHEED pattern shown in Figure 5.2 (a) indicates 2D

growth. Figure 5.2(b) gives the RHEED intensity oscillation pattern with time. The small decay of the intensity oscillation for the thin film growth shows well-formed surface layer-by-layer growth, thus great structure. By applying the ARXPS method, the first question to be answered is the surface chemical composition and if there is electronic reconstruction.

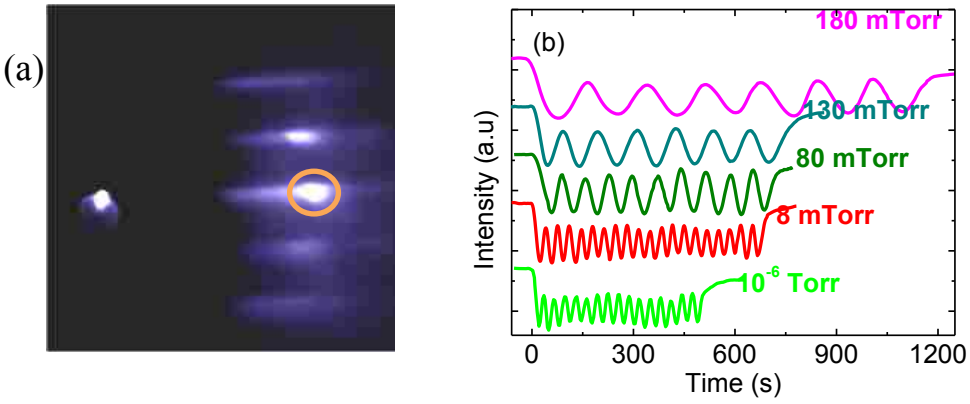

Figure 5.2. (a) RHEED pattern of LSMO thin film during film growth. (b) RHEED intensity oscillation pattern at various oxygen partial pressures.

The LSMO 6uc thin films have been exposed in air and returned to chamber for further XPS study. Before doing XPS, we annealed the sample at temperature 550°C for two hours. Figure 5.3 (a) of LEED pattern shows the surface still remains 1x1 morphology, which is the same pattern as it is before taking out the chamber, indicating the surface structure remains unchanged. Because the exposure time in air is quite long, the surface contamination caused the LEED background to be strong. Figure 5.3 (b) is the STM scan at large scale of 500 nm. To perform the STM scanning, a conductive 0.1wt% Nb doped $SrTiO_3$ substrate was used. Nice terrace with width about 50 nanometers is observed. A single step height of ~0.39 nm can be found in our STM image, indicating a single termination surface.

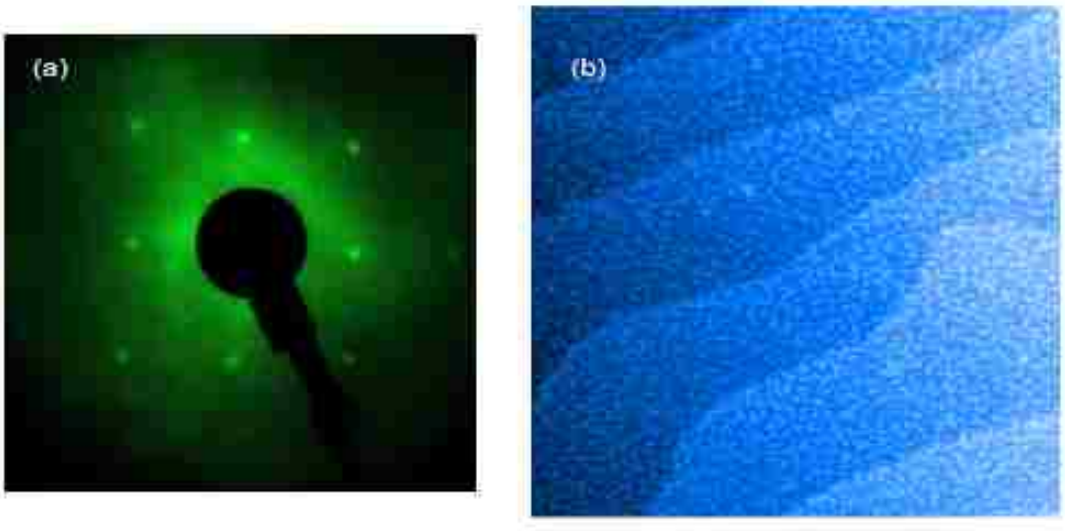

Figure 5.3. (a) LEED pattern taken at room temperature with beam energy 200 eV. (b) STM image with scale 500 nm*500 nm.

5.3 ARXPS study of surface composition for LSMO 6UC thin film

After the STM and LEED data were acquired, we immediately transfer the sample to the XPS in situ to ensure the same surface conditions. Figure 5.4 depicts the four spectra Mn 2p, O1s, La 3d and Sr 3p respectively. Notice Mn 2p and La 3d has clear spin orbiting splitting, and we use Mn $2p_{3/2}$ and La $3d_{5/2}$ intensities in this experiment. Both La $3d_{5/2}$ and La $3d_{3/2}$ have the double peaks feature with the higher binding energy one being the satellite component. Due to complexity of O 1s peak, we are only analyzing the Sr 3p, Mn 2p and La 3d spectra.

From LEED pattern (Figure 5.3), we can clearly see the surface is not reconstructed. The only possibility on the surface termination is either (La, Sr)O or MnO_2. It is naturally to believe the termination of MnO_2 as the substrate surface is TiO_2. However, nature always acts beyond our expectation. ISS data shows the surface is mainly Sr and Oxygen with little sign of Mn and La. We can conclude the surface is (La,Sr)O terminated; but how much concentration of La in deed?

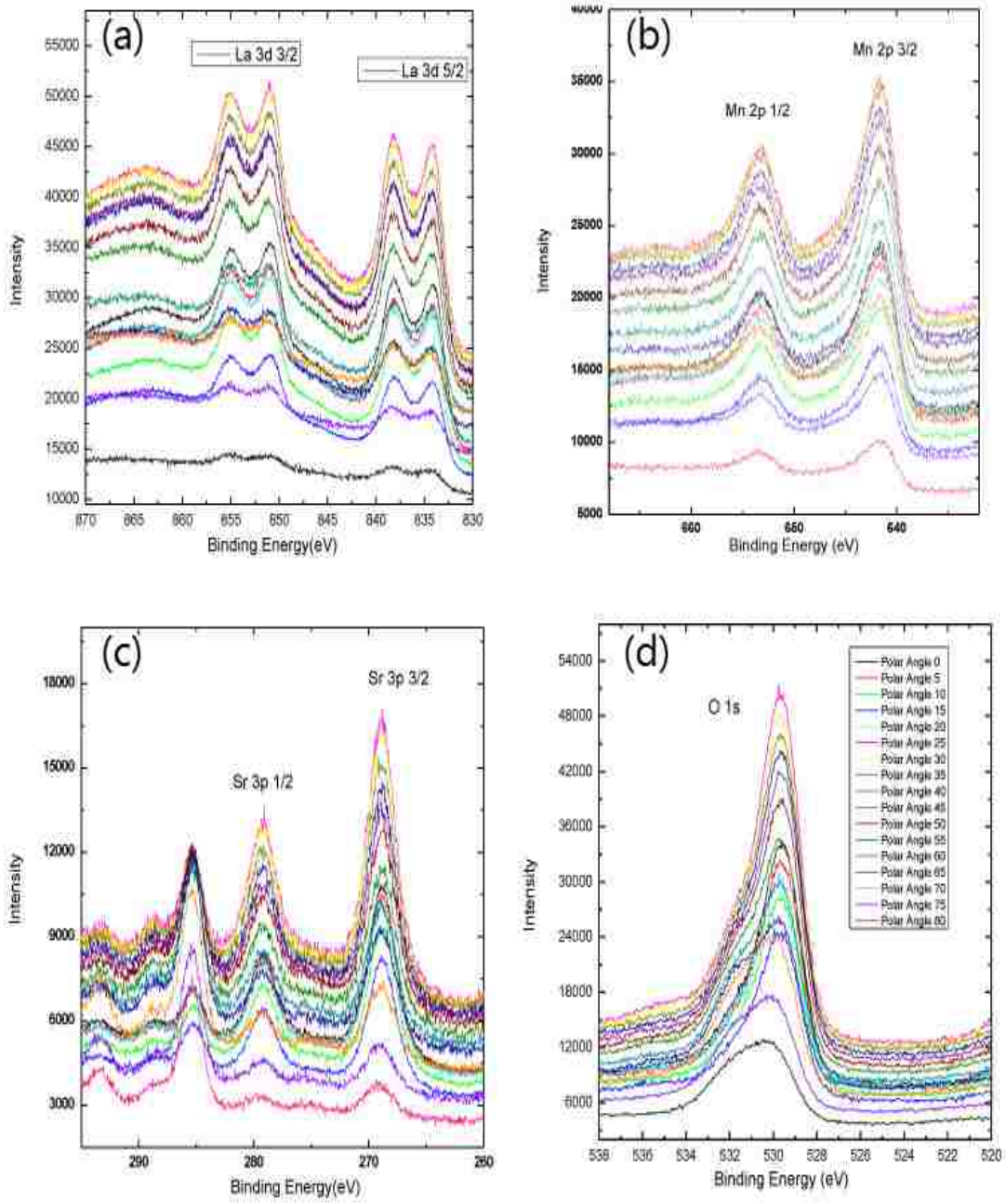

Figure 5.4. Core level spectra of (a) La 3d, (b) Mn 2p, (c) Sr 3p and (d) O 1s taken at normal emission from LSMO(100) surface. All data were taken at room temperature. A clear signature of satellite is observed for La 3d shown in (a). Additional bump at higher binding energy side of Sr 3p spectra is C 1s peak.

To reveal the surface composition, we calculated the intensity ratio of Sr 3p/La $3d_{5/2}$ and Mn $2p_{3/2}$/La $3d_{5/2}$. The purpose of doing the Sr/La ratio is to look for possible change of Sr concentration for the thin film from the target materials. Figure 5.5 (a) plots the angular dependence of intensity ratio of Sr/La. The modulation caused by the photoelectron diffraction is observed. At high emission angle, there is substantial Sr segregation on the surface indicating Sr composition does not remain same for the thin film from the single crystal. Or intuitively, if the difference is only coming from the surface? Mn/La intensity ratio shown in Figure 5.5(b) indicates La composition on the surface is very small.

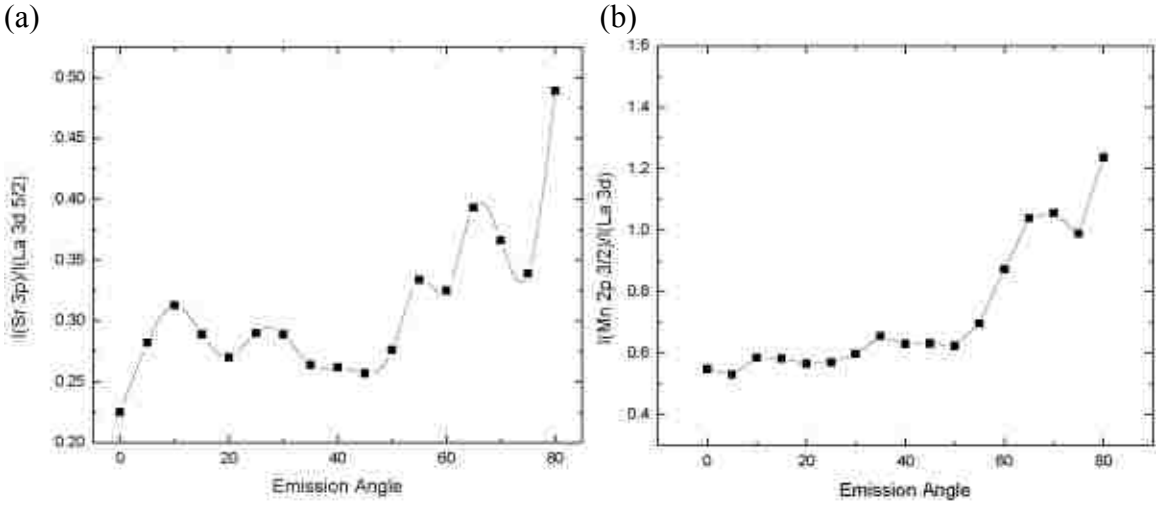

Figure 5.5. (a) Sr 3p/La $3d_{5/2}$ intensity ratio, (b) Mn $2p_{3/2}$/La $3d_{5/2}$ intensity ratio with emission angles.

To qualitatively to calculate the Sr surface segregation or characterize the composition, we need to have full information of the cross section and IMFP for each characteristic spectrum. The table 5.2 listed the necessary information for me to calculate the intensity ratio without considering the diffraction effect.

Table 5.1 Cross sections of Sr 3p, La $3d_{5/2}$ and Mn $2p_{3/2}$ cited from Spec lab data base. The kinetic energy and IMFP are listed in the last two columns.

Element	Z	Electron Shell	Shell	σ(Al K_a)	E_k(eV)	λ(E) (Å)
Sr	38	$1s^2 2s^2 2p^6 3s^2 3p^6 3d^{10} 4s^2 4p^6 5s^2$	3p 3/2	4.33	1206.2	22.74
La	22	$1s^2 2s^2 2p^6 3s^2 3p^6 3d^2 4s^2$	3d 5/2	28.11	654.7	10.2
Mn	8	$1s^2 2s^2 2p^4$	2p 3/2	9.16	844.4	12.9

By applying the same method developed and assuming the Sr/La has a linear decay with the thinness, we simulated the forward scattering amplitude and pure surface effects. Figure 5.6 is the ball model of the structure of the 6uc thin films. The whole theoretical calculation is based on the stacking sequence shown in the Figure 5.6. 7 UC LSMO thin film has already exhibited the metallic properties and we believe within this 6UC thin film, there shall be a layer within has the right composition as the target material. People observed the surface segregated Sr increases as oxygen pressure decreases, and interpreted that Sr replaces La on the AO-terminated surface of the perovskite. There are also proposals that the surface oxygen vacancy concentration controls the degree of segregation. A hypothesis about the origin of A-site segregation is the formation of the A-site containing oxides separated on the surface. We here tentatively propose a Sr/La ratio decay profile to possibly analyze the surface composition.

This profile can be written as:

$$\begin{aligned} f_i^{Sr} &= b - ai, \\ f_i^{La} &= 1 - f_i^{Sr}, \\ f_j^{Mn} &= 1 \end{aligned} \tag{5.1}$$

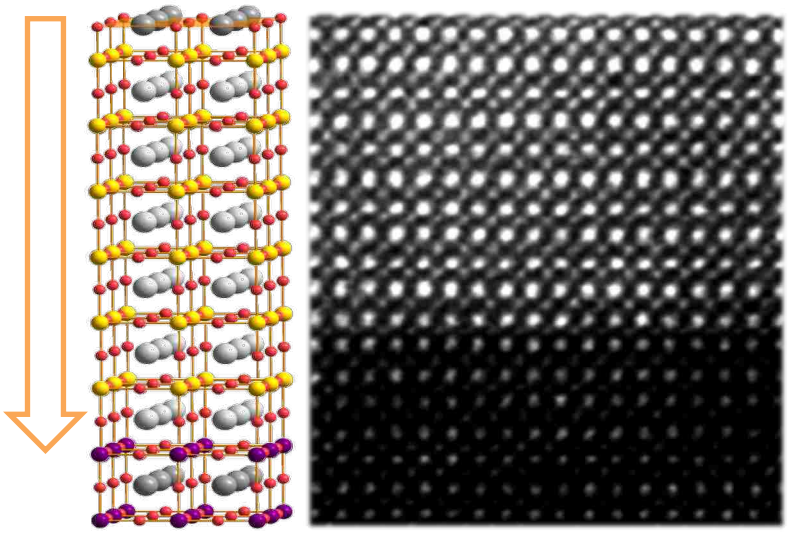

Figure 5.6. Illustration of LSMO 6 UC thin film stacking sequence. The top layer starts with (La,Sr)O.

From the experimental result from Mn/La intensity ratio, we derived the relationship between b and a is $1.27b - 1.65a = 0.856$ utilizing the equation 5.2.

$$\frac{I(Mn)}{I(La)} \frac{\sum_j e^{-jd/\lambda_A(E)Cos(\theta)}}{\sum_i (1-f_i^{Sr}) e^{-jd/\lambda_B(E)Cos(\theta)}} \cdot \frac{\sigma_{Mn}}{\sigma_{La}} \tag{5.2}$$

Then similarly, another equation for parameters b and a is $2.44b - 3.87a = 1.56$ derived from Sr/La intensity ratios. Coefficients b and a can be calculated as 0.83, 0.12 respectively. The detail (La, Sr) composition for each layer is as follows:

$$\begin{aligned}
f_{Sr}^1 &= 0.71 \quad f_{La}^1 = 0.29 \\
f_{Sr}^2 &= 0.59 \quad f_{Sr}^2 = 0.41 \\
f_{Sr}^3 &= 0.47 \quad f_{La}^3 = 0.53 \\
f_{Sr}^4 &= 0.35 \quad f_{La}^4 = 0.65 \\
f_{Sr}^5 &= 0.23 \quad f_{La}^5 = 0.77 \\
f_{Sr}^6 &= 0.11 \quad f_{La}^6 = 0.89
\end{aligned} \tag{5.3}$$

This linear model does not look reasonable as the 2nd, 3rd, 4th, and 5th layers fall into the regions of metallic ground state. Different approach using exponential decay is

proposed for further study. Also the thickness dependence study of angular dependence of intensity ratio is highly needed to summarize a theoretical model. We conclude from my study that the Sr concentration at the surface is appreciably higher than the corresponding bulk value. Such an off-stoichiometric behavior should link to the different physical properties such as nonmetallic/nonmagnetic "dead layer" behavior in the ultrathin films compared with the bulk crystal.

CHAPTER 6. CORE LEVEL STUDY OF IRON ARSENNIDE $BaFe_2As_2$

6.1 Introduction and motivation

The superconductivity in the Fe based systems is widely discussed. The pressure and doping induced superconductivity in the compounds are particularly interesting because these are the tuning parameters of understanding the high T_c superconductivity [139]. A high-pressure neutron scattering study reported the c parameter of $BaFe_2As_2$ (122) systems reduced drastically to a "collapsed tetragonal phase" [140]. If pressure plays the same role as doping of the superconductivity is one of the questions that we generally like to ask. There is a theoretical study suggesting a giant coupling of Fe spin state with the lattice structure [141]. Therefore, the lattice, spin and electron are highly correlated in this system. In the above mentioned reference, the As-As hybridization between both intra and inter plane As ions is also controlled by the Fe magnetic states. In contrast to this result, the low magnetic Fe moment measured is mostly interpreted by Fe 3d and As 4p hybridized states [142,143]. To further understand how the electronic structure evolves with doping, especially the interaction between Fe spin state and lattice structure, we propose to use the X ray photoelectron spectroscopy to examine the valence band and core level spectra to understand the underlying superconducting mechanism and the above-mentioned inconsistent discoveries.

Different studies reviewed the on-site Coulomb repulsion parameter U for Iron based superconductors. The values of U, which would account for the pairing strength in an electronic based mechanism, have been found ranging from 1 eV to 4 eV [144,145,146,147]. While the emergence of iron superconductivity is in close proximity of antiferromagnetic ground state and the phase diagram resembles layered cuprates, revealing whether the iron based superconductor is on the verge of Mott insulator as

cuprates can help to determine the starting point of the theoretical description of iron based superconductors. If Fe superconductors (FeSC) are strong correlated as cuprates, one might expect to see the satellite features for Fe core level spectra as a indication of correlation. As follows, we report a systematic study of electronic structure of the $BaFe^2As^2$ and its electron (Co^{3+}) and hole (K^+) doped compounds using X-ray Spectroscopy techniques.

Single crystals of $BaFe_2As_2$, $Ba_{0.6}K_{0.4}Fe_2As_2$ and $BaFe_{1.86}CO_{0.14}As_2$ (abbreviated forthwith as Ba122, K0.4 and Co0.07 are flux grown. All samples were cleaved at room temperature in our UHV μ metal-shielded analysis chamber equipped with and XPS. XPS measurements were carried out with a Phoibos 150 MCD Energy Hemispherical Analyzer using photon energy of 1486.74 eV from a Specs Micro-Focus 500 ellipsoidal crystal Mono-chromator with Al α x-ray source and focusing x-ray spot capabilities, a passing energy of 30 eV. The step energy in the spectra is 0.01 eV. The overall energy resolution for the XPS spectra is 0.16 eV. The base pressure of our system during the measurements was better than $2e10^{-9}$ Torr. The experiments were carried out at room temperature.

The structure of $BaFe_2As_2$ shown in Figure 6.1 (a) is tetragonal with I4/mmm symmetry. Low energy electron diffraction (LEED) was performed in situ, directly after sample cleaving. For all measured samples (both parent and doping), only the tetragonal unit cell spots were seen in LEED with no sign of extra spots as would occur due to reconstructions or lattice distortion. LEED data on the Ba122 (001) surface indicates an ordered arsenic (As) terminated metallic surface (Figure 6.1b). People have identified the

surface plane of cleaved $BaFe_2As_2$ crystals as the As terminated Fe-As layer-the plane where superconductivity occurs [Figure 1c]. Reconstruction could happen at different cleaving conditions.

Photoemission spectra are usually displayed in binding energies relative to the Fermi edge of the sample. However, what really measured are the kinetic energies of electrons emitted from the sample. The curve can be well described by Fermi dirac distribution curve for Fermion system. The Fermi level is at a position when *F(E)=0.5*. From our data for three samples, we can clearly identify the Fermi edge because of sharp Fermi edge and decent resolution. The accurate calibration is executed using Au 4f 7/2 spectra, which has peak position 84.0 eV, staying constant, even after several days.

Now look at the electronic states near E_f (Figure 6.1c). The 8 eV bandwidth is mainly for the valance band and the sharp peaks near the E_f can be identified as Fe 3d and As 4p. Since we are using the hard X-ray source here, the mean free path for Fe and As atoms are almost identical. In several literatures, both theoretical and experimental studies have indicated that Fe 3d and As 4p are highly hybridized to explain the measured low Fe magnetic moment, our result shows a certain degree of hybridization, but mainly suggest that the electronics states near Fermi level are Fe 3d or other d electrons from dopants. People has introduced LDA+U schedules to relate the As 4p and Fe 3d hybridization to the correlation effect. To investigate the physical consequences of the latter in more detail, we consider studying the satellite peaks in the later content. With doping of K and Co, the whole valence spectra do not show substantial modifications and spectral transfer. The main effect of doping on the crystal structure at room temperature is decreasing As–Fe–As bond angles and Fe–Fe distances [148], thus modifying the electronic structure.

This is responsible for the broadening of the Fe 3d spectra in K doping valence band. In Figure 6.1(c) with Dopant Co, the near Fermi Edge spectra has additional 3d peak near the Fe 3d spectra. In the mean time, there is no sign of Co peaks mixed with As-4p (3-6 eV), and As-4s (11-13 eV) spectra. This is consistent with the DFT calculations which predicts a similar DOS of Co close to the chemical potential, with only a relative energy shift with Fe 3d [149]. Some theoretical DFT studies of the changes in the density of states close to the Fermi energy of the Co substituted materials [150] suggest a shift in the density of states qualitatively consistent with a so called virtual crystal approach in which basically the extra nuclear charge on Co is in effect averaged over the whole crystal.

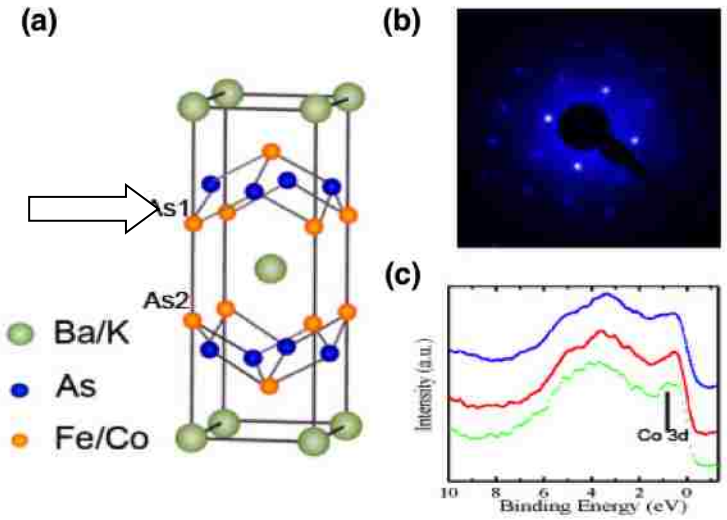

Figure 6.1. (a) The structure of Ba122 compounds with a arrow pointing to the Cleavage plane. The Ba atoms shown in green are sitting between Fe-As layers. (b) LEED pattern took at beam energy 153 eV at room temperature with no reconstruction. (c) Comparison of valence band data for Ba122; The solid bar points to the Co 3d peaks near the Fe 3d spectra. The overall resolution in the XPS experiment is 0.16 eV.

6.2 Doping dependence of core level spectra

As we know, when the band filling is varied, the binding energy shift ΔE satisfies this equation: $\Delta E = -\Delta\mu + K\Delta Q + \Delta V_M - \Delta E_R$. Here $\Delta\mu$ is chemical potential shift, ΔQ is the change in the number of valence electrons on the considered atom and K is a constant, ΔV_M is the change in the Madelung potential, and ΔE_R is the change in the extra-atomic relaxation energy. To understand the binding energy shifts, we need to analyze each terms in the equation. First let us look at the deep core level spectra for the compounds. Figure 6.2 shows the Fe 2p, Ba 3d and As 3p which have binding energies above 100eV. The Fe 2p will be specially discussed in later chapter. The core levels for Ba and Fe of K doped sample have larger shift than Co doped one and also in the opposition direction. The previous study has shown the chemical potential shifts are only around 80meV for 40% K doping and minimal for 7% Co doping. [151] In our core level study by hard X ray source, 80 meV change is difficult to identify due to the resolution limit. Figure 6.2 displays the binding energy shift of core levels Fe 2p, Ba 3d and As 3p respectively. Apparently there is another important factor to which accounts for such opposite larger shift than estimated chemical potential shift. It is known that the screening term ΔE_R is proportional to the mobile carrier concentration, thus it has the same sign on both hole doping and electron doping sides. The screening effect for 7% Co shall have much small effect than 40% K doping which can still not explain the large shifts. The ΔV_M term is not supposed to change much since the Madelung potential relates to the system physics structure only. So the opposite shift of core levels are attributed to the change of the valancy for the doped site, which is the KΔQ including both the change in the electrostatic potential and the change in the intra-atomic relaxation energy. As 3p

spectra has small shift than Ba and Fe atoms due to less effect of doping on the electrostatic potential. The detail binding energy positions are displayed in Table.1. By looking at details of the spectra shape, Ba 3d spectra has additional weight on the high binding energy side which can be understood as the surface components that contains half of the number of Ba atoms compared to the bulk Ba layers in order to create a symmetric cleave [152]. The Fe 2p peaks can be fitted with single Gaussian broadened Donia-Sunjic line shape with asymmetric index around 0.43, in very resemblance of Fe metal ones but no apparent satellite features are observed, indicating the systems are much less correlated than cuprates.

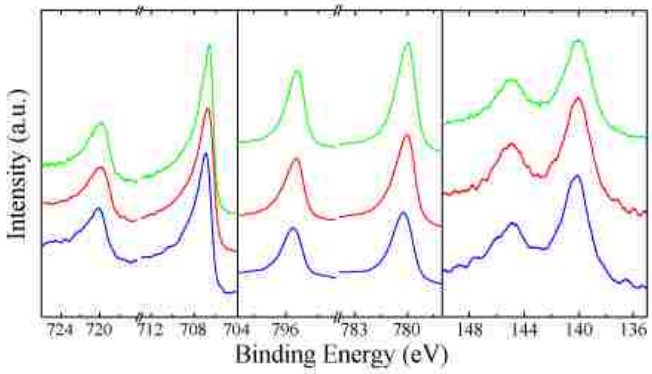

Figure 6.2. Core level spectra (a) Fe 2p (b) Ba 3d (c) As 3p taken at room temperature.

Ba shallow core levels have a similarly higher binding energy shoulder as shallow core level Ba 3d. For As shallow core levels, the surface contribution which cause the asymmetric effect of the line shape is smaller than Ba spectra. The small spectral weight in the As spectra compared to the Ba case can be taken as evidence that the effect of the presence of the surface is screened in a certain degree for the atomic layers below the Ba termination layer. The shallow core level binding energy positions of Ba 4d, As 3d, As 3p

and Fe 3p are also shown in Table 1. Since the doping is at the position of Ba and Fe sites and As is only supposed to be affected by the chemical potential, the As 3p binding energy shifts will reflect the chemical potential shift mainly. We can see the deduced shifts for As 3d and As 3p for both K and Co doping systems (shifting to lower binding energy at 0.02 eV and 0.08 eV respectively) are substantially smaller than other core levels, suggesting the chemical potential shift is very small. The Ba 4d chemical potential shift for K doped sample is relatively bigger than Co doped one, which is simply because the K doping has more influence on Ba electronic structure since K replaces the positions of Ba atoms. One thing remains puzzled is Fe binding energy position in K doped system also presents a qualitatively shift towards higher binding energy as Ba core levels do. This suggests that simple valency energy change cannot be the single cause of core level shifts.

Table 6.1 Core levels of Ba, Fe and As spectra for parent and doped compounds.

Core Levels	$BaFe_2As_2$	ΔE ($Ba_{0.6}K_{0.4}Fe_2As_2$)	ΔE ($BaFe_{1.86}Co_{0.14}As_2$)
Ba $3d_{5/2}$	780.01	0.22	-0.08
Ba $4p_{3/2}$	178.22	0.23	-0.06
Ba $4d_{5/2}$	89.41	0.28	-0.04
Fe $2p_{3/2}$	706.77	0.17	-0.13
Fe $3p_{3/2}$	53.18	0.09	-0.13
As $3p_{3/2}$	140.01	0.03	-0.02
As $3d_{5/2}$	40.58	0.08	-0.08

6.3 Core level study of Fe 3p and As 3d

Now let us focus on Fe spectra. As we expect, Fe satellite can elucidate the role of electron correlations. Figure 6.3 depicts the Fe 2p and Fe 3p spectra for parent and doped systems. The left panel inset is a comparison of Fe 2p spectra between Ba122 systems (colored in red) and simple Fe metal (colored in blue). It is alike to those of Fe metal, obviously differentiating itself from cuprates from the correlation point of view. Missing of Fe 2p satellite peaks associated with Fe 3d electrons set an upper limit on the effective coulomb parameter U~1eV [153]. However there is a report of resonance photoemission for Fe 3p line [154], suggests the systems is quite correlated. The Fe 3p core level is presented in Figure 6.3 right panel, which shows clearly 3 distinct components: the main peak, surface component and Satellite after Shirly background subtraction. These satellites spectra around 10-11 eV above the main peak can be scribed to shake-up or charge, transfer processes. However, there are a few works which suggested the charge transfer process (either ligand to metal or metal to ligand) cannot be the cause of Fe satellites because comparable shake-up satellites do not appear on photoelectron lines associated with the ligand [155]. Another group shows the shake-up processes were attributed to the movement of an electron from a 3d orbital to the empty 4s orbital during ejection of core 2p photoelectron, which implied a hole-hole interaction and in turn the correlations that narrow the 3d bands. This broadened satellite accompanying with Fe 3p cannot provide ample evidence for the electron correlation because the satellite feature of core Fe 2p is hardly seen, proving the correlation is fairly weak. The total intensity for the satellite peak is slightly decreased with doping comparing with parent compounds. Another message from the Fe 3p spectra is that the energy difference between the satellite

and main peaks have shrinked after doping with both electrons and holes. Understanding the satellite feature help us to define this correlation strength of 122 systems is pretty weak. This clearly differs from another class of superconductor: cuprate.

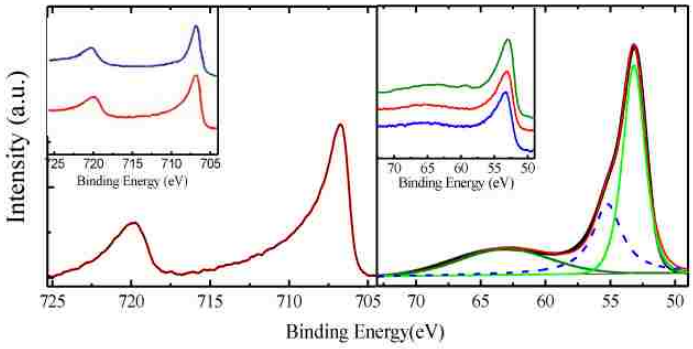

Figure 6.3. (a) Fe 2p spectra. The spectra are similar to Fe metal with similar peak position and line shape. Detail comparison is shown in the left panel inset with blue curve marking the Fe metal spectra. (b) Fe 3p spectra. A broad satellite peak is depicted with 11 eV energy different fro the main peak. The right panel inset shows the comparison of Fe 3p spectra for differing doping.

Figure 6.4 describes the As 3d spectra. As 3d has clear spin orbital splitting $3d_{3/2}$ and $3d_{5/2}$. As we usually know the momentum-integrated intensity of high-spin peak As $3d_{5/2}$ should be larger than that of low-spin peak As $3d_{3/2}$. Thus it is hard to explain the higher binding energy component has higher intensity than lower one without considering two components of As 3d peaks. With surface As atoms has bond dangling, we believe the higher binding component of As 3d core levels come from surface. As discussed in one theoretical study, the As-As hybridization will have interactions of both intra and inter layers as the structure evolves which are tuned well by pressure and doping.

We plotted both the intensity ratio of surface component to bulk and FWHM versus doping level. The surface components for both doped systems are reduced, indicating that collapsed lattice in c direction enhances the As-As interlayer interaction or reduce

the bonding between Fe-As layers. The decrease of line width for doped sample indicates the enhancement of photoelectron lifetime. This tuning capability by doping and structure provide the confidence that the As-Fe and As-As bonding are associated with a mechanism of superconductivity.

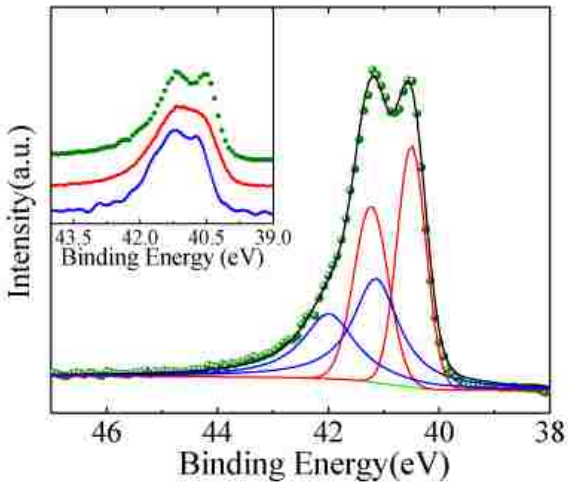

Figure 6.4. Fitted spectra for As 3d core levels. The As $3d_{3/2}$ and As $3d_{5/2}$ peaks are displayed by Red curves. The Blue curves present additional components of As 3d main peaks. The inset shows the comparison of As 3d spectra under differing doping levels.

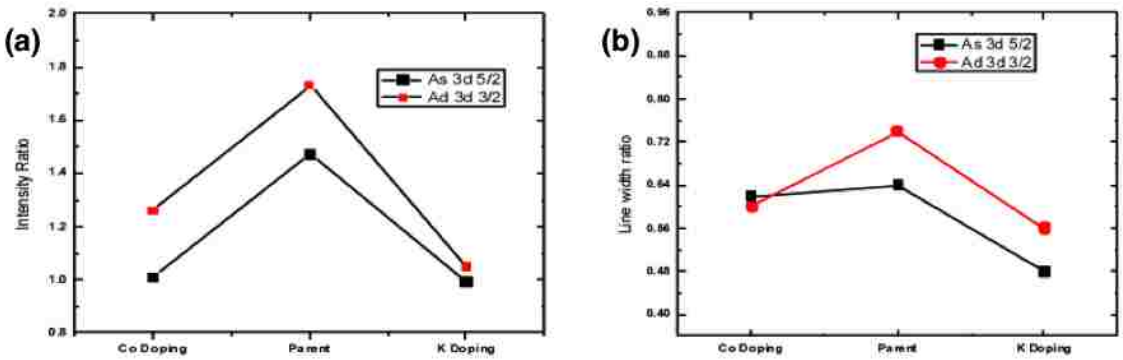

Figure 6.5. (a) As 3d b) FWHM surface components and bulk components ratio for both As $3d_{5/2}$ and As $3d_{3/2}$. Both peaks' bulk/surface ratio is higher than the hole and electron doped systems. (b) FWHM for bulk/surface components are plotted.

We have carried out a systematic photoemission investigation of high quality $BaFe_2As_2$, $Ba_{0.6}K_{0.4}Fe_2As_2$ and $Ba(Fe_{0.93}Co_{0.07})_2As_2$ single crystals. We observed no satellite feature for Fe 2p proving the $BaFe_2As_d$ systems are itinerant or weekly correlated. The Fe 3p broad satellite is complicated to understand because the Fe 3p binding energy is pretty shallow with possibilities to interact with other valence electrons. The doping effect has been reflected mostly on the valency energy instead of chemical potential shift mentioned by other study. Our results demonstrate that the hole doping in the system is largely bonded with the Ba and Fe atoms instead of As. The As-As and As-Fe bonding in the systems are particular important to reveal unconventional mechanism of superconductivity as it is highly correlated with doping, structure evolution and magnetic states suggested by other studies.

CHAPTER 7. DISCUSSION AND SUMMARY

The fundamental issues for the understanding of these emergent phenomena include the structure and chemical composition in the proximity of surface/interface in TMOs. There are not so many tools as for bulk to probe the chemical concentration. In the thesis, I have developed a method using angle resolved X-ray photoelectron spectroscopy (ARXPS) to characterize the surface structure and chemical composition. Only with consideration of the photoelectron diffraction effects on the relative intensities of different core electron levels, the surface chemical composition variation can be accurately calculated. The well-known crystal surface of Sr_2RuO_4 (100) is used to verify the effectiveness of our methodology. The diffraction pattern due to the forward scattering peaks is discussed. The known SrO termination layer gives exponential increase with the emission angles. Both effects considered for a theorectial calculation of intensity ratio matchs with te

Combing the use of low energy electron diffraction (LEED) and scanning tunneling microscopy (STM) with ARXPS, we investigated the surface structure and chemical composition of the most widely used crystal surface: $SrTiO_3$ (100). The surface maintains non reconstructed at annealing temperature 500^{o}c and exhibits out-of-the-plane bulking relaxation. The Ti 2p/Sr 3p intensity ratio at high photoelectron emission angle show that the surface is TiO_2-layer terminated and has significant oxygen-deficiency. These results confirm the conjecture from LEED-I(V) refinement on structure. Finally, the chemical composition of the ultrathin crystalline films of $La_{2/3}Sr_{1/3}MnO_3$ on $SrTiO_3$ (100) has also been discussed. Sr surface segregation was found on the surface. We assume the Sr/La concentration has exponential decreases from the top to the bottom layer. There is at least

one layer in the thin film has similar Sr/La concentration as bulk. The overall Sr richness is possible due to the Sr reservoir of substrate $SrTiO_3$. We believe the off-stoichiometric behavior on the surface is intrinsic and should be associated with the exciting physical properties such as nonmetallic/nonmagnetic "dead layer" behavior in the ultrathin films compared with the bulk crystal.

Complex materials in the proximity of surface and in the form of thin films or interface require the understanding of surface and interface chemical concentration. Our methodology using ARXPS and forward scattering (zero order diffraction) theory provides a useful tool to probe the surface composition. In the future, we shall be able to investigate the thickness dependence of the thin film, such as LSMO, to further study the segregation and dead layer issues. The application of our methodology can be used more precisely if we take the spectra at smaller step of emission angles to reduce the errors.

LIST OF REFERENCES

[1] E. Dagotto. Complexity in strongly correlated electronic systems. *Science* **309**, 257 (2005).

[2] J. G. Bednorz and K. A. Muller. Possible High T_C Superconductivity in the Ba-La-Cu-O System. *Z. Phys. B Cond. Matt.* **64**, 189 (1986).

[3] Patrick A. Lee, N. Nagaosa, and X.G. Wen. Doping a mott insulator: Physics of high-temperature superconductivity. *Rev. Mod. Phys.* **78**, 17 (2006).

[4] J. R. Waldram. Superconductivity of Metals and Cuprates. *Institute of Physics Publishing* (1996).

[5] G. V. M. Williams, J. L. Tallon, E. M. Haines, R. Michalak, and R. Dupree. NMR Evidence for a d-Wave Normal-State Pseudogap. *Phys. Rev. Lett.* **78**, 721 (1997).

[6] D. Vaknin, S. K. Sinha, D. E. Moncton, D. C. Johnston, J. M. Newsam, C. R. Safinya, and H. E. King. Antiferromagnetism in La_2CuO_{4-y}. *Phys. Rev. Lett.***58**, 2802 (1987).

[7] S. H. Pan, J. P. O'Neal, R. L. Badzey, C. Chamon, H. Ding, J. R. Engelbrecht, Z. Wang, H. Eisaki, S. Uchida, A. K. Gupta, K. -W. Ng, E. W. Hudson, K. M. Lang and J. C. Davis. Microscopic Electronic Inhomogeneity in the High Tc Superconductor $Bi_2Sr2CaCu_2O_{8+x}$. *Nature* **413**, 282-285(2001).

[8] S. Nakatsuji and Y. Maeno. Quasi-Two-Dimensional Mott Transition System $Ca_{2-x}Sr_xRuO_4$. *Phys. Rev. Lett.* **84**, 2666 (2000).

[9] Y. Maeno, S. Nakatsuji, S. Ikeda. Metal-Insulator transitions in layered ruthenates. *Materials Science and Engineering B* **63**, 70 (1999).

[10] S. Nakatsuji, D. Hall, L. Balicas, Z. Fisk, K. Sugahara, M. Yoshioka, and Y. Maeno. Heavy-mass fermi liquid near a ferromagnetic instability in layered ruthenates. *Phys. Rev. Lett*. **90**, 137202 (2003).

[11] O. Friedt, M. Braden, G. André, P. Adelmann, S. Nakatsuji, and Y. Maeno. Structural and magnetic sspects of the metal-insulator transition in $Ca_{2-x}Sr_xRuO_4$. *Phys. Rev. B* **63**, 174432 (2001).

[12] A. P. Mackenzie and Y. Maeno. The Superconductivity of Sr_2RuO_4 and the Physics of Spin-Triplet Pairing. *Rev. Mod. Phys.* **75**, 657 (2003).

[13] J. B. Goodenough. Magnetism and the Chemical Bond, *Interscience*, New York (1963).

[14] K. Ebata, M. Hashimoto, K. Tanaka, A. Fujimori, Y. Tomioka, Y. Tokura. Temperature-dependent photoemission spectral weight transfer and chemical potential shift in $Pr_{1-x}Ca_xMnO_3$: Implications for charge density modulation. *Cond-mat* **0707**.0160v1 (2007).

[15] Y. Tokura, Y. Tomioka, H. Kuwahara, A. Asamitsu, Y. Moritomo, and M. Kasai. Origins of Colossal Magnetoresistance in Perovskite-type Manganese Oxides. *Journal of Applied Physics* **79**, 5288 (1996).

[16] Y. Tomioka, A. Asamitsu, Y. Moritomo, H. Kuwahara, and Y. Tokura. Collapse of a Charge-Ordered State under a Magnetic Field in $Pr_{1/2}Sr_{1/2}MnO_3$. *Phys. Rev. Lett*. **74**, 5108 (1995).

[17] H. Kuwahara, Y. Tomioka, A. Asamitsu, Y. Moritomo, and Y. Tokura. A First-Order Phase Transition Induced by a Magnetic Field. *Science* **270**, 961 (1995).

[18] Z. Jirak, S. Vratislav, and J. Zajicek. Magnetic Structure of $Pr_{0.9}Ca_{0.1}MnO_3$. *Physica Status Solidi A-Applied Research* **52**, K39 (1979).

[19] A. P. Mackenzie and Y. Maeno. The superconductivity of Sr_2RuO_4 and the physics of spin-triplet pairing. *Rev. Mod. Phys*. **75**, 657 (2003).

[20] Y. Hashimoto, K. Yoshida, S. Nishizaki, T. Fujita, J. G. Bednorz, and F. Lichtenberg. Superconductivity in a layered perovskite without copper. *Nature London* 372, 532 (1994).

[21] K. D. Nelson, Z. Q. Mao, Y. Liu, and Y. Maeno. Odd-Parity Superconductivity in Sr_2RuO_4. *Science* **306**, 1151 (2004).

[22] S. A. Grigera, R. S. Perry, A. J. Schoteld, M. Chiao, S. R. Julian, G. G. Lonzarich, S. I. Ikeda, Y. Maeno, A. J. Millis, and A. P. Mackenzie. Magnetic Field-Tuned Quantum Criticality in the Metallic Ruthenate $Sr_3Ru_2O_7$. Science **294**, 329(2001).

[23] G. Cao, L. Balicas, W. H. Song, Y. P. Sun, Y. Xin, V. A. Bondarenko, J. W. Brill, S. Parkin, and X. N. Lin. Competing Ground State in Triple-layered $Sr_4Ru_3O_{10}$: Verging on Itinerant Ferromagnestism with Critical Fluctuations. Phys. Rev. B **68**, 174409 (2003).

[24] Z. Q. Mao, M. Zhou, J. Hooper, V. Golub, and C. J. O'Connor. Phase Separation in the Itinerant Metamagnetic Transition of $Sr_4Ru_3O_{10}$. Phys. Rev. Lett. 96, 077205 (2006).

[25] D. Fobes, M. H. Yu, M. Zhou, J. Hooper, C. J. O'Connor, M. Rosario, and Z. Q. Mao. Phase Diagram of the Electronic States of Trilayered Ruthenate $Sr_4Ru_3O_{10}$. *Phys. Rev. B* **75**, 094429 (2007).

[26] L. Klein, J. S. Dodge, C. H. Ahn, G. J. Snyder, T. H. Geballe, M. R. Beasley, and A. Kapitulnik. Anomalous Spin Scattering Effects in the Badly Metallic Itinerant Ferromagnet $SrRuO_3$. *Phys. Rev. Lett.* **77**, 2774 (1996).

[27] G. Cao, S. McCall, M. Shepard, J. E. Crow, and R. P. Guertin. Thermal, magnetic, and transport properties of single-crystal $Sr_{1-x}Ca_xRuO_3$ ($0<\sim x<\sim 1.0$). *Phys. Rev. B* **56**, 321 (1997).

[28] A. Schilling, M. Cantani, J. D. Guo, H. R. Ott. Superconductivity above 130 K in the Hg-Ba-Ca-Cu-O system, *Nature* **363**, 56 (1993).

[29] A. V. Boris, Y. Matiks, E. Benckiser, A. Frano, P. Popovich, V. Hinkov, P. Wochner, M. Castro-Colin, E. Detemple, V. K. Malik, C. Bernhard, T. Prokscha, A. Suter, Z. Salman, E. Morenzoni, G. Cristiani, H. -U. Habermeier, B. Keimer. Dimensionality Control of Electronic Phase Transitions in Nickel-Oxide Superlattices, *Science* **332**, 937 (2011).

[30] K. Yoshimatsu, K. Horiba, H. Kumigashira, T. Yoshida, A. Fujimori, M. Oshima. Metallic Quantum Well States in Artificial Structures of Strongly Correlated Oxide. *Science* **333**, 319 (2011).

[31] R. T. Senger and K. K. Bajaj. Optical properties of confined polaronic excitons in spherical ionic quantum dots. *Phys. Rev. B* **68**, 045313 (2003).

[32] J. Tao, D. Niebieskikwiat, M. Varela, W. Luo, M. A. Schofield, Y. Zhu, M. B. Salamon, J. M. Zuo, S. T. Pantelides, S. J. Pennycook. Direct Imaging of Nanoscale Phase Separation in $La_{0.55}Ca_{0.45}MnO_3$: Relationship to Colossal Magnetoresistance, *Phys. Rev. Lett*. **103**, 097202 (2009).

[33] L. W. Zhang, C. Israel, A. Biswas, R. L. Greene, A. de Lozanne. Direct Observation of Percolation in a Manganite Thin Film, *Science* **298**, 805 (2002).

[34] Nobel Lecture by Herbert Kroemer in G, Ekspong, ed., Noble Lectures, Physics 1996-2000 World Scientific, Singapore (2002).

[35] A. P. Ramirez. Oxide electronics emerge. *Science* **315**, 1377–1378 (2007).

[36] C. Cen, S. Mannhart, S. Thiel, J. Levy. Oxide nanoelectronics on demand. *Science* **323**, 1026–1030 (2009).

[37] A. Ohtomo, H. Y. Hwang. A high-mobility electron gas at the $LaAlO_3/SrTiO_3$ heterointerface. *Nature* **427**, 423–426 (2004).

[38] C. H. Ahn, J. M. Triscone, J. Mannhart. Electric field effect in correlated oxide systems. *Nature* **424**, 1015–1018 (2003).

[39] A. Ohtomo, D. A. Muller, J. L. Grazul, H. Y. Hwang. Artificial charge-modulation in atomic-scale perovskite titanate superlattices. *Nature* **419**, 378–380 (2002).

[40] A. F. Santander-Syro, O. Copie, T. Kondo, F. Fortuna1, S. Pailhès, R. Weht, X. G. Qiu, F. Bertran, A. Nicolaou,A. Taleb-Ibrahimi, P. Le Fèvre, G. Herranz, M. Bibes, N. Reyren, Y. Apertet, P. Lecoeur, A. Barthélémy, M. J. Rozenberg. Two-dimensional electron gas with universal subbands at the surface of $SrTiO_3$, *Nature* **469**, 189 (2011).

[41] W. Meevasana, P. D. C. King, R. H. He, S-K. Mo, M. Hashimoto, A. Tamai, P. Songsiriritthigul, F. Baumberger, Z-X. Shen. Creation and control of a two-dimensional electron liquid at the bare $SrTiO_3$ surface. *Nature Materials* **10**, 114 (2011).

[42] S. Kimura, M. Tsukada. Electronic structure of the (001) surface of reduced $SrTiO_3$, *Applied Surface Science* **121/122**, 195 (1997).

[43] S. Okamoto, A.J. Millis. Electronic reconstruction at an interface between a Mott insulator and a band insulator. *Nature* **428**, 630–633 (2004).

[44] Z. S. Popovic, S. Satpathy, R. M. Martin. Origin of the two-dimensional electron gas carrier density at the $LaAlO_3$ on $SrTiO_3$ interface. *Phys. Rev. Lett.* **101**, 256801(2008).

[45] S. Thiel, G. Hammer, A. Schmehl, C. W. Schneider, J. Mannhart. Tunable quasitwo-dimensional electron gases in oxide heterostructures. *Science* **313**, 1942–1945 (2006).

[46] C. Cen, S. Thiel, G. Hammerl, C.W. Schneider, K.E. Anderson, C.S. Hellberg, J. Mannhart and J. Levy. Nanoscale control of an interfacial metal–insulator transition at room temperature. *Nature Material* **7**, 298–302 (2008).

[47] N. Reyren, S. Thiel, AD. Caviglia. Superconducting interfaces between insulating oxides. *Science* **317**, 1196–1199 (2006).

[48] K. Ueno, S. Nakamura, H. Shimotani, A. Ohtomo, N. Kimura, T. Nojima, H. Aoki, Y. Iwasa and M. Kawasaki. Electric-field-induced superconductivity in an insulator. *Nature Material* **7**, 855–858 (2008).

[49] A. Brinkman, M. Huijben, M. van Zalk, J. Huijben, U. Zeitler, J. C. Maan, W. G. van der Wiel, G. Rijnders, D. H. A. Blank and H. Hilgenkamp. Magnetic effects at the interface between non-magnetic oxides. Nature Material **6**, 493–496 (2007).

[50] R. Pentcheva and W. E. Pickett. Electronic phenomena at complex oxide interfaces: insights from first principles. *J. Phys.: Cond. Mat.* **22**:043001 (2010).

[51] S. Thiel, G. Hammerl, A. Schmehl, C. W. Schneider, and J. Mannhart. Tunable electron gases in oxide heterostructures. *Science*, **313:**1942(2006).

[52] S. Okamoto and A. Millis. Electronic Reconstruction at an Interface between a Mott Insulator and a Band Insulator. *Nature* **428**, 630 (2004).

[53] M. Takizawa, H. Wadati, K. Tanaka, M. Hashimoto, T. Yoshida, A. Fujimori, A. Chikamatsu, H. Kumigashira, M. Oshima, K. Shibuya, T. Mihara, T. Ohnishi, M. Lippmaa, M. Kawasaki, H. Koinuma, S. Okamoto, and A. J. Millis. Photoemission from Buried Interfaces of $LaAlO_3$/SrTiO3 Superlattices. *Phys. Rev. Lett.* **97**, 057601 (2009).

[54] M. Salluzzo, J. C. Cezar, N. B. Brookes, V. Bisogni, G. M. De Luca, C. Richter, S. Thiel, J. Mannhart, M. Huijben, A. Brinkman, G. Rijnders, and G. Ghiringhelli. Orbital Reconstruction and the Two-Dimensional Electron Gas at the $LaAlO_3/SrTiO_3$ Interface. *Phys. Rev. Lett.* **102**, 166804 (2009).

[55] M. Sing, G. Berner, K. Goβ, A. Müller, A. Ruff. A. Wetscherek, T. Thiel, J. Mannhart. S.A. Pauli. C.W. Schneider, P. R. Willmott, M. Gorgoi, F. Schäfers, and R. Claessen. Profiling the Interface Electron Gas of $LaAlO_3/SrTiO_3$ Heterostructures with Hard X-ray Photoelectron Spectroscopy. *Phys. Rev. Lett.* **102**, 176805 (2009).

[56] W. Siemons, G. Koster, H. Yamamoto, W.A. Harrison, G. Lucovsky, T. H. Geballe, D.H.A. Blank, and M.R. Beasley. Origin of Charge Density at $LaAlO_3$ on $SrTiO_3$ Heterointerfaces: Possibility of Intrinsic Doping. *Phys. Rev. Lett*. **98**, 196802 (2007).

[57] G. Herranz, M. Basletić, M. Bibes, C. Carrétéro, E. Tafra, E. Jacquet, K. Bouzehouane, C. Deranlot, A. Hamzić, J.-M. Broto, A. Barthélémy, and A. Fert. High Mobility in $LaAlO_3/SrTiO_3$ Heterostructures: Origin, Dimensionality, and Perspectives. *Phys. Rev. Lett*. **98**, 216803 (2007).

[58] P. R. Willmont, S. A. Pauli, R. Herger, C. M. Schlepütz, D. Martoccia, B.D. Patterson, B. Delley, R. Clarke, D. Kumah, C. Cionca, and Y. Yacoby. Structural Basis for the Conducting Interface between $LaAlO_3$ and $SrTiO_3$. *Phys. Rev. Lett*. **99**, 155502 (2007).

[59] A. S. Kalabukhov, Yu. A. Boikov, I. T. Sakharov, V. N. Popok, R. Gunnarsson, J. Börjesson, N. Ljustina, E. Olsson, D. Winkler and T. Claeson. Cationic Disorder and Phase Segregation in $LaAlO_3/SrTiO_3$ Heterointerfaces Evidenced by Medium-Energy Ion Spectroscopy. *Phys. Rev. Lett*. **103**, 146101 (2009).

[60] R. Pentcheva and W. E. Pickett. Avoiding the Polarization Catastrophe in $LaAlO_3$ Overlayers on $SrTiO_3$ (001) through Polar Distortion. *Phys. Rev. Lett.* **102**, 107602 (2009).

[61] U. Schwingenschlögl and C. Schuster. Exponential Decay of Relaxation Effects at $LaAlO_3/SrTiO_3$ Heterostructures. *Chem. Phys. Lett.* **467**, 354 (2009).

[62] S. Thiel, G. Hammerl, A. Schmehl, C. W. Schneider, and J. Mannhart. Tunable Quasi-Two-Dimensional Electron Gases in Oxide Heterostructures. *Science* **313**, 1942 (2006).

[63] J. Mannhart and D.G. Scholm. Oxide Interfaces — An Opportunity for Electronics. *Science* **327**, 1607-1611 (2010).

[64] H. Koinuma, N. Kanda, J. Nishino, A. Ohtomo, H. Kubota, M. Kawasaki, and M. Yoshimoto. Laser MBE of Ceramic Thin Films for Future Electronics. *Appl. Surf. Sci.* **109/110**, 514 (1997).

[65] M. Kawasaki, M. Izumi, Y. Konishi, T. Manako, and Y. Tokura. Perfect Epitaxy of Perovskite Manganite for Oxide Spin-Electronics. *Mat. Sci. Eng.* B **63**, 49 (1999).

[66] H. M. Christen and G. Eres. Recent Advances in Pulsed-Laser Deposition of Complex Oxides. *J. Phys.: Condens. Matter* **20**, 264005 (2008).

[67] J. Tersoff, D. R. Hamann. Theory of the scanning tunneling microscope. *Phys.Rev. B* **31**, 805 (1985).

[68] S. Doniach and M. Sunjic. Many-electron singularity in X-ray photoemission and X-ray line spectra from metals. *J. Phys. C* **3**, 285-291 (1970).

[69] D. Briggs and J. C. Riviere. Spectral Interpretation. *Chapter 3 in Practical Surface Analysis*, Second edn., **Vol. 1** (Eds. and M. P. Seah), Wiley, Chichester (1990).

[70] G. E. Muilenberg. Handbook of X-ray Photoelectron Spectroscopy. PerkinElmer Corp (1979).

[71] D. Briggs, M. P. Seah. Practical Surface Analysis, 2nd ed., **Vol. 1**, John Wiley & Sons (1990).

[72] S. Tougaard. Background Correction in XPS: Comparison of Validity of Different Methods. *Surf. Sci.* **216**,343 (1989).

[73] D. A. Shirley. High Resolution X-ray Photoemission Spectrum of Valence Bands of Gold. *Phys.Rev.B* **5**, 4707(1972).

[74] S. Hufner. Photoelectron Spectroscopy. *Springer-Verlag*, Berlin (1995).

[75] C. S. Fadley and S. A. L. Bergstrom. Electron Spectroscopy or Chemical Analysis. *Phys. Lett.* **35A**, 375 (1971).

[76] M. Pijolat and G. Hollinger. New depth-profiling method by angular-dependent x-ray photoelectron spectroscopy. *Surf.Sci.* **105**, 114(1981).

[77] D. A. Shirley. Electron Spectroscopy. *North Holland*, Amsterdam (1972).

[78] J. Chastain. *Handbook of X-ray Photoelectron Spectroscopy*, Perkin-Elmer Corp. (1992).

[79] Thermo Fisher Scientific report: Application Note: **31014** (2008).

[80] Hani Dulli, P. A. Dowben, S.-H. Liou,, and E. W. Plummer. Surface segregation and restructuring of colossal-magnetoresistant manganese perovskites, $La_{0.65}Sr_{0.35}MnO_3$. *Phys .Rev. B* **62**, R14629 (2000).

[81] K. Siegbahn, U. Gelius, H. Siegbahn and E. Olson. Angular distribution of electrons in ESCA spectra from a single crystal. *Phys.Lett. A* **32**, 221 (1970).

[82] R. J. Baird, C. S. Fadley and L. F. Wagner. Angular-dependent x-ray-photoelectron peak intensities from single-crystal gold. *Phys.Rev.B* **15**, 666 (1977).

[83] M. Kudo, M. Owari, Y. Nihei, Y. Gohshi and H. Kamada, Proc. Int. Conf. On X-ray and XUV Spectroscopy, Sendai, (1978).

[84] S. M. Goldberg, R. J. Baird, S. Kono, N. F. T. Hall and C. S. Fadley. Two-Beam Kikuchi-Band Theory. *J. Electron Spectrosc. Relat. Phenon*. **21** (1980).

[85] D. Norman, D. P. Woodruff, N. V. Smith, M. M. Traum and H. H. Farrell. Temperature Dependence of Normal Emission Photoelectron Diffraction and Analogies with EXAFS. *Phys. Rev. B*, **18,** 6789 (1978).

[86] P. J. Orders, S. Kono, C. S. Fadley, R. Trehan and J. T. Lloyd. Scattering Theory and Effects of Vibration. *Surf.Sci. **119**,* 371 (1982).

[87] M. Owari, M. Kudo, Y. Nihei and H. Kamada. Experimental and Theoretical Two-Dimensional X-ray Photoelectron Diffraction Patterns from GaAs(001) Surface. *J. Electron Spectrosc. Relat. Phenom*. **34**, 215 (1984).

[88] C. H. Li, A. R. Lubinsky and S. Y. Tong, *Phys. Rev. B*, **17,** 3128 (1978).

[89] P. Rennert. Multiple Scattering Theory in the Small Scattering Centre Approximation. *Phys. Status Solidi B*, **105**, 213 (1981).

[90] T. Fujikawa. Theory of Angle-Resolved X-Ray Photoemission by Multiple-Scattering Cluster Method. *J. Phys. Soc.Jpn.*, **54,** 2747 (1985).

[91] A. Chasse and P. Rennert. Influence Optical Properties on the Spin Polarization of Cu 3p Photoelectrons. *Phys. Status Solidi B*, **138**, 53 (1986).

[92] W. F. Egelhoff, Jr. The XPS Searchlight Effect. *J. Vac. Sci. Technol*. **A3**, 1511(1985).

[93] H. C. Poon and S. Y. Tong. Focusing and diffraction effects in angle-resolved x-ray photoelectron spectroscopy. Phys.Rev.B **31**, 6211 (1984).

[94] E. L. Bullock and C. S. Fadley. Determination of Epitaxial Overlayer Structures from High-Energy Electron Scattering and Diffraction. *Phys.Rev.B*, **31**, 1212 (1985).

[95] S. Y. Tong, H. C. Poon and D. R. Snider. Importance of Multiple Forward Scattering in Medium- and High-energy Electron Emission and/or Diffraction spectroscopies. *Phys. Rev. B* **32**, 2096 (1985).

[96] A. Chasse and P. Rennert. Theoretical Angle-Resolved X-Ray Photoelectron. *Phys.Status Solidi B* **141**, K147 (1987).

[97] W. F. Egelhoff, XPS Forward Scattering Studies of Epitaxial Overlayers and Sandwich Structures of Au and Ag on Ni(100). *Jr. J. Vac. Sci. Technol.* **A6,** 730 (1988).

[98] Y. Maeno, H. Hashimoto, K. Yoshida, S. Nishizaki, T. Fujita, J. G. Bednorz. Superconductivity In a Layered Perovskite without Copper. *Nature* **372**, 532(1994).

[99] K. Ishida, H. Mukuda, Y. Kitaoka, K. Asayama, Z. Q. Mao, Y. Mori, and Y. Maeno. Spin-triplet superconductivity in Sr_2RuO_4identified by ^{17}O Knight shift. *Nature* **396**, 658 (1998).

[100] A. P. Mackenzie, Y. Maeno. The superconductivity of Sr_2RuO_4 and the physics of spin-triplet pairing. *Rev. Mod. Phys.* **75**, 657 (2003).

[101] Y. Maeno, T. M. Rice, M. Sigrist, *Phys Today* **54**, 42 (2001).

[102] H. Z. Guo, Y. Li, D. Urbina, B. Hu, R. Jin, T. Liu, D. Fobes, Z. Q. Mao, E. W. Plummer, and J. D. Zhang. Doping and Dimensionality Effects on the Core-Level Spectra of Layered Ruthenates. *Phys. Rev. B* **81**, 155121(2010).

[103] S. Nakatsuji and Y. Maeno. Quasi-Two-Dimensional Mott Transition System $Ca_{2-x}Sr_xRuO_4$. *Phys. Rev. Lett*. **84**, 2666 (2000).

[104] R. Matzdorf, Z. Fang, Ismail, J. Zhang, T. Kimura, Y. Tokura, K. Terakura, and E. W. Plummer. Ferromagnetism Stabilized by Lattice Distortion at the Surface of the p-Wave Superconductor Sr_2RuO_4. *Science* **289**,746 (2000).

[105] Z. Q. Mao, M. Zhou, J. Hooper, V. Golub, and C. J. O'Connor. Phase Separation in the Itinerant Metamagnetic Transition of $Sr_4Ru_3O_{10}$. *Phys. Rev. Lett*. **96**, 077205 (2006).

[106] S. Watanabe, T. Hikita and M. Kawai. Artifical Layered Oxides by Pulsed Laser Deposition. *J. Vac. Sci. Technol*. **A9**, 2394 (1991).

[107] J. G. Mavroides, J. A. Kafalas, and D. F. Kolesar. Photoelectrolysis of water in cells with $SrTiO_3$ anodes. *Appl. Phys. Lett*. **28**, 241 (1976).

[108] B. Cord and R. Courths. Electronic study of $SrTiO_3$(001) surfaces by photoemission. *Surf. Sci.* **162**, 34 (1985).

[109] T. Ohnishi, K. Shibuya, and M. Lippmaa, D. Kobayashi, H. Kumigashira, and M. Oshima, H. Koinuma. Preparation of thermally stable TiO_2-terminated $SrTiO_3$ (100) substrate Surfaces. *Appl. Phys. Lett*. **85**, 272 (2004).

[110] R. Bachelet, F. Sánchez, F. J. Palomares, C. Ocal, and J. Fontcuberta. Atomically flat SrO-terminated $SrTiO_3$ (001) substrate. *Appl. Phys. Lett.* **95**, 141915 (2009).

[111] M. Radovic, N. Lampis, F. Miletto, P. Perna, Z. Ristic, M. Salluzzo, C.M. Schleputz, U. Scottiddi Uccio. Growth and Characterization of Stable SrO-terminated $SrTiO_3$ Surfaces. *Appl.Phys.Lett.* **94**, 022901(2009).

[112] N. Erdman, L. D. Marks. $SrTiO_3$(001) surface structures under oxidizing conditions. *Surface Science* **526**, 107001(2003).

[113] Martin R. Castell. Scanning tunneling microscopy of reconstructions on the $SrTiO_3$ (001) surface. *Surface Science* **505**, 1 (2002).

[114] Martin R. Castell. Nanostructures on the $SrTiO_3$ (001) surface studied by STM. *Surface Science* **516**, 33 (2002).

[115] N. Erdman, K. R. Poeppelmeier, M. Asta, O. Warschkow, D. E. Ellis, and L. D. Marks. Atomically flat SrO-terminated $SrTiO_3$ (001) substrate. *Nature London* **419**, 55 (2002).

[116] N. Erdman, O. Warschkow, M. Asta, K. R. Poeppelmeier, D. E.Ellis, and L. D. Marks. Effect of Oxygen Deficiency on $SrTiO_3$(001) Surface Reconstructions. J. *Am. Chem. Soc.* **125**, 10050 (2003).

[117] C. H. Lanier, A. van de Walle, N. Erdman, E. Landree, O. Warschkow, A. Kazimirov, K. R. Poeppelmeier, J. Zegenhagen, M. Asta, L. D. Marks. Atomic-scale

structure of the $SrTiO_3$(001)-c(6x2) reconstruction: Experiments and first-principles calculations. *Phys. Rev. B* **76**, 045421 (2007).

[118] S. H. Phark, Y. J. Chang, and T. W. Noh. Selective growth of perovskite oxides on SrTiO3 (001) by control of surface reconstructions. *Appl. Phys. Lett*. **98**, 161908 (2011).

[119] J. Cheng, P. Regreny , L. Largeau, G. Patriarche, O. Mauguin, K. Naji, G. Hollinger, G. Saint-Girons. Influence of the surface reconstruction on the growth of InP on SrTiO3 (001). *Journal of Crystal Growth* **311**, 1042 (2009).

[120] A. Ohtomo, H. Y. Hwang. A High-Mobility Electron Gas at the $LaAlO_3/SrTiO_3$ Heterointerface. *Nature* **427**, 423 (2004).

[121] N. Reyren, S. Thiel, A. D. Caviglia, L. F. Kourkoutis, G. Hammerl, C. Richter, C. W. Schneider, T. Kopp, A. -S. Ruetschi, D. Jaccard, M. Gabay, D. A. Muller, J. -M. Triscone, J. Mannhart. Superconducting Interfaces between insulating oxides. *Science* **317**, 1196(2007).

[122] J. Biscaras, N. Bergeal, A. Kushwaha, T. Wolf, A. Rastogi, R.C. Budhani, J. Lesueur. Two-Dimensional superconductivity at Mott insulator/band insulator interface $LaTiO_3/SrTiO_3$. *Nature Communications* **1**, 89 (2010).

[123] B. Zheng, and N. Binggeli, Influence of the interface atomic structure on the magnetic and electronic properties of $La_{2/3}Sr_{1/3}MnO_3/SrTiO_3$(001) heterojunctions, *Phys. Rev. B* **82**, 245311 (2010).

[124] Y. Liang, D. A. Bonnell. Structures and chemistry of the annealed $SrTiO_3$ (001) surface. *Surf. Sci.* **310**, 12894 (1994)**.**

[125] Y. Liang, D. Bonnell. Effect of variations in stoichiometry on the surface-structure of $SrTiO_3$ (001). *J. Am. Ceram. Soc.* **78**, 2633 (1995).

[126] A. Hirata, A. Ando, K. Saiki, A. Koma. Characterization of surface defects formation in strontium-titanate (100). *Surf. Sci.* **310**, 89 (1994).

[127] J. Kawai, Doctoral Thesis, University of Tokyo (1989).

[128] A. Urushibara, Y. Moritomo, T. Arima, A. Asamitsu, G. Kido, Y. Tokura. Insulator-metal transition and giant magnetoresistance in $La_{1-x}Sr_xMnO_3$. *Phys. Rev. B* **51**, 14103(1995).

[129] J. -H. Park, E. Vescovo, H. -J. Kim, C. Kwon, R. Ramesh, T. Venkatesan. Direct evidence for a half-metallic ferromagnet. *Nature* **392**, 794 (1998).

[130] A. Fert. Review of recent results on spin polarized tunneling and magnetic switching by spin injection. *Materials Science and Engineering B* **84**, 1 (2001).

[131] V. Garcia. Ferroelectric Control of Spin Polarization, *Science* **327**, 1106 (2010).

[132] D. Pantel, S. Goetze, D. Hesse, M. Alexe. Reversible elecrical switching of spin polarization in multiferroic tunnel junctions. *Nature Materials* **11**, 289 (2012).

[133] J. Z. Sun, D. W. Abraham, R. A. Rao, C. B. Eom. Thickness dependent magnetotransport in ultrathin manganite films. *Appl. Phys. Lett*. **74**, 3017 (1999).

[134] R. P. Borges, W. Guichard, J. G. Lunney, J. M. D. Coey and F. Ott. Magnetic and electric "dead layers " in $(La_{0.7}Sr_{0.3})MnO_3$ thin films. *J. Appl. Phys*, **89**,3868 (2001).

[135] M. Huijben, L. W. Martin, Y.-H. Chu, M. B. Holcomb, P. Yu, G. Rijnders, D. H. A. Blank, and R. Ramesh. Critical thickness and orbital ordering in ultrathin $La_{0.7}Sr_{0.3}MnO_3$ films. *Phys. Rev. B* **78**, 094413 (2008).

[136] M. Angeloni, G. Balestrino, N. G. Boggio, P. G. Medaglia, P. Orgiani, A. Tebano. Suppression of the metal-insulator transition temperature in thin $La_{0.7}Sr_{0.3}MnO_3$ films. *J. Appl. Phys.* **96,** 6387(2004).

[137] A.Tebano, C. Aruta, P. G. Medaglia, F. Tozzi, and G. Balestrino, A. A. Sidorenko, G. Allodi, and R. De Renzi, G. Ghiringhelli, C. Dallera, and L. Braicovich, N. B. Brookes. Evidence of orbital reconstruction at interfaces in $La_{0.67}Sr_{0.33}MnO_3$ films. *Phys. Rev. B* **74**, 245116 (2006).

[138] B. Kim, D. Kwon, T.Yajima, C. Bell, Y. Hikita, Bog G. Kim, and H. Y. Hwang. Reentrant insulating state in ultrathin manganite films. *Appl. Phys. Lett*. **99**, 092513 (2011).

[139] P.L. Alireza. Superconductivity up to 29 K in $SrFe_2As_2$ and $BaFe_2As_2$ at high pressures. *J. Phycs. Condens. Matter* **21**, 012208 (2009).

[140] A. Kreyssig, M. A. Green, Y. Lee, G. D. Samolyuk, P. Zajdel, J. W. Lynn, S. L. Budko, M. S. Torikachvili, N. Ni, S. Nandi, J. B. Leao, S. J. Poulton, D. N. Argyriou, B. N. Harmon, R. J. McQlueeney, P. C. Canfield, and A. I. Goldman. Pressure-induced volume-collapsed tetragonal phase of $CaFe_2As_2$ as seen via neutron scattering. *Phys. Rev. B* **78**, 184517 (2008).

[141] T. Yildirim. Strong Coupling of the Fe-Spin State and the As-As Hybridization in Iron-Pnictide Superconductors from First-Principle Calculations. *Phys. Rev. Lett.* **102**, 037003(2010).

[142] J. Wu, Ph. Phillips, and A.H. Castro Neto. Theory of the magnetic moment in iron pnictides. *Phys. Rev. Lett*. **101**, 126401 (2008).

[143] D. R. Garcia, C. Jozwiak, C. G. Hwang, A. Fdorov, S. M. Hanrahan, S. D. Wilson, C. R. Rotundu, B. K. Freelon, R. J. Birgeneau, E. Bourret-Courchesne, and A. Lanzara. Core-level and valence-band study using angle-integrated photoemission on $LaFeAsO_{0.9}F_{0.1}$. *Phys. Rev. B* **78**, 245119 (2008).

[144] K. Haule, J.H. Shim, G. Kotliar. Correlated Electronic Structure of $LaO_{1-x}F_xFeAs$. *Phys. Rev. Lett*. **100**, 226402 (2008).

[145] L. Craco, M. S. Laad, S. Leoni, and H. Rosner. Normal-state correlated electronic structure of iron pnictides from first principles. *Phys. Rev. B* **78**, 134511 (2008).

[146] V. Vildosola, L. Porovskii, R. Arita, S. Biermann, and A. Georges. Bandwidth and Fermi surface of iron oxypnictides: Covalency and sensitivity to structural changes. *Phys. Rev. B* **78**, 064518(2008).

[147] V.I. Anisimov, D. M. Korotin, S. V. Streltsov, A. V. Kozhevnikov, J. Kunes, A. O. Shorikov, and M. A. Korontin. Density-functional calculation of the Coulomb repulsion and correlation strength in superconducting LaFeAsO. *JETP Lett*. **88**, 729 (2008).

[149] M. Rotter, M. Tegel, and D. Johrendt. Superconductivity at 38 K in the Iron Arsenide $(Ba_{1-x}K_x)Fe_2As_2$. *Phys.Rev.Lett*. **101**, 107006(2008).

[149] H. Wadati, I. Elfimov, and G. A. Sawatzky. Where Are the Extra *d* Electrons in Transition-Metal-Substituted Iron Pnictides? *Phys. Rev. Lett.,* **105**, 157004 (2010).

[150] A. S. Sefat, R. Jin, M. A. McGuire, B. C. Sales, D. J.Singh, and D. Mandrus. Superconductivity at 22 K in Co-Doped $BaFe_2As_2$ Crystals. *Phys. Rev. Lett*. **101**, 117004 (2008).

[151] M. Neupane, P. Richard, Y.-M. Xu, K. Nakayama, T. Sato, T. Takahashi, A. V. Federov, G. Xu, X. Dai, Z. Fang, Z. Wang, G. -F. Chen, N. -L. Wang, H.-H. Wen, and H. Ding. Electron-hole asymmetry in the superconductivity of doped $BaFe_2As_2$ seen via the rigid chemical-potential shift in photoemission. *Phys. Rev. B* **83**, 094522 (2011).

[152] V. B. Nascimento, Ang Li, D. R. Jayasundara, Yi Xuan, Jared O'Neal, S. H. Pang, T. Y. Chien, Biao Hu, X. B. He, Guorong Li, A. S. Sefat, M. A. McGuire, B. C. Sales, D. Mandrus. M. H. Pan, Jiandi Zhang, R. Jin, and E. W. Plummer. Surface Geometric and Electronic Structures of $BaFe_2As_2$ (001). *Phys. Rev. Lett*. **103**, 076104(2009).

[154] S. -L. Drechsler, H. Rosner, M. Grobosch, G. Behr, F. Roth, G. Fuchs, K. Koepernik, R. Schuster, J. Malek, S. Elgazzar, M. Rotter, D. Johrendt, H. -H. Klauss, B. Büchner, M. Knupfer. New insight into the physics of iron pnictides from optical and penetration depth data. arXiv:**0904**.0827 (2009).

[154] H. Ding, K. Nakayama, P. Richard, S. Souma, T. Sato, T. Takahashi, M. Neupane, Y.M. Xu, Z.H. Pan, A.V. Fedorov, Z. Wang, X. Dai, Z. Fang, G.F. Chen, J.L. Luo and N. L. Wang. Electronic structure of optimally doped pnictide $Ba_{0.6}K_{0.4}Fe_2As_2$: a comprehensive angle resolved photoemission spectroscopy investigation. *J. Phys. Condens. Matter* **23**, 135701(2011).

[156] A. P. Grosvenor, B. A. Kobe, M. C. Biesinger and N. S. McIntyre. Investigation of multiplet splitting of Fe 2p XPS spectra and bonding in iron compounds. *Surf. Interface Anal.* **36**, 1564–1574(1984).

VITA

Yi Li received her bachelor's degree at Nanjing University of Post and Telecommunications in 2003. Thereafter, she entered graduate school in the Department of Physics and Astronomy at Louisiana State University. She will receive her doctor's degree in May 2013 and plans to run a startup company related to renewable energy.